Università degli Studi di Cagliari

Ph.D. DEGREE
Innovation Sciences and Technologies

Cycle XXXIV

Nanoporous Metals: Fabrication and Structure-Properties Relationship

Scientific Disciplinary Sector

CHIM/07

Ph.D. Student: Andrea Pinna

Supervisor: Prof. Luca Pilia

Co-Supervisor: Prof. Giorgio Pia

Final exam. Academic Year 2020/2021
Thesis defence: April 2022 Session

TABLE OF CONTENTS

Introduction

Nanoporous metals represent a unique class of materials with promising properties for a wide set of applications in advanced technology. Their combined self-supported monolithic form, high surface area, and high electrical conductivity are only the most obvious peculiarities of this kind of material. Since the beginning of an intensive work in 2001, nanoporous metals have shown high potential and tunable properties. However, the effective use in real applications is hampered by some challenging issues, such as the difficult fabrication of low-cost metals in a nanoporous form, the mechanical fragility and the low stability in certain working environments, i.e. electrolytes or high temperatures, and by the lack of a full understanding of the origin of some peculiar properties. The work presented in this thesis has been done with the purpose to address these issues. The fabrication of nanoporous metals and related composites has been studied to enlarge the possible properties of the common nanoporous gold and copper, and at the same time to find new strategies for the fabrication of nanoporous aluminum, a promising material for its low-cost, low-density, high electrical conductivity and corrosion resistance. Moreover, nanoporous gold thermal stability and behavior toward the degradation of organic dyes were further explored.

Chapter 1

Theoretical Framework

Porous materials are commonly defined as materials constituted by solid and void parts, called pores. Pores, that can be in turn occupied by other substances or fluids, can exist in several less or more complex architectures. Depending on their open or closed form, we can find isolated cavities, ordered channels, or percolating networks of passages. Porous materials possess unique properties which are strictly connected to their structure, such as the pores volume fraction, their dispersion and distribution inside the matrix, and chemical composition [1]. Their exceptional versatility makes this kind of materials suitable in a wide range of applications areas, such as insulation, construction, impact protection, sorption, catalysis and membranes [1].

When the characteristic lengths of a material drop to the nanometer scale, a significant part of atoms will be located at the surface, provoking dramatic changes to its properties compared with the bulk counterpart. Since the atomic fraction of atoms located at the surface changes with the characteristic lengths of the nanostructure, properties are commonly related to the characteristic lengths and can be modulated by tuning them. Among nanostructured materials, nanoporous (NP) ones are made of pores whose size can range from fractions of nm to 1 μm. Depending on this, they are grouped by IUPAC into three categories:

- Microporous materials: pore diameter between 0.2 and 2 nm;
- Mesoporous materials: pore diameter between 2 and 50 nm;
- Macroporous materials: pore diameter between 50 nm and 1 μm.

Despite this definition, in literature, these terms are also widely used for indicating different pore sizes – i.e., microporous materials are related to pore sizes in the micrometer order of magnitude.

During last decades, NP materials took a very important place in many technological areas, thanks to their unique surface chemistry, high surface area, large pore volume and high control of the pore structures [2,3]. Among them, NP metals constitute an important group with unique properties [4-6], commonly defined as metallic materials with pore sizes smaller than 200 nm and a porosity of no less than 30% [6]. An NP metal can be thought as randomly interconnected metal nanoparticles that form a continuous structure of metal ligaments and pores [4-6]. They, therefore, possess

typical physical and chemical properties of metal nanoparticles, with the important differences that they can be produced in monolithic form and easily handled; moreover, they are not subjected to agglomeration and don't need a suspension medium [4-6].

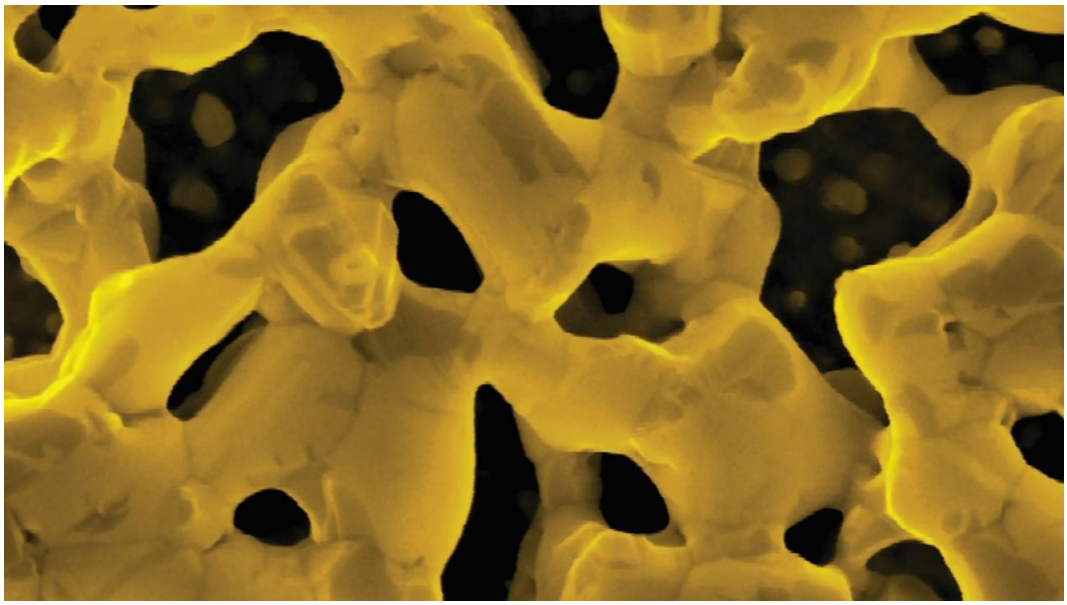

Fig. 1.1 Typical network of interconnected ligaments and pores of an NP metal produced by dealloying [7].

NP metals exhibit partial disentanglement between characteristic lengths, porosity degree and total surface area [4,8,9]. Different combinations of these fundamental features can give rise to different sets of physical and chemical properties, which make NP metal foams show a unique promise in terms of property engineering and tailoring starting from fundamental science.

NP metal foams have been extensively studied for their effective catalytic and electrocatalytic activity and selectivity, or as membrane materials for fuel cell application [5]. In addition, as electrochemical supercapacitors, they can deliver high levels of electrical power and energy storage density coupled with long operational lifetimes [10,11] or enact chemical and electrochemical actuation [12]. Otherwise, they have been proven to be stable substrates for electrochemical and optical sensing [13] and as plasmonic platforms for Surface-Enhanced Raman Spectroscopy (SERS) and Metal-Enhanced Fluorescence (MEF) [14-18]. In addition, NP metals offer great perspectives as structural materials, thanks to their promising mechanical properties matched with a low density [9,19-21].

NP metals can be fabricated in different ways, the most common being dealloying [4]. Dealloying is a process in which, layer by layer, one or more components of an alloy are selectively removed and the other components

diffuse along the interface between the alloy and the surrounding environment, to minimize their surface free energy [9]. In the proper fabrication conditions, this process leads to the formation of a 3D network of interconnected ligaments and pores with tunable characteristic lengths. An example of this typical structure is shown in . Besides, the dealloyed material maintains the microstructure[1] of the parent alloy, apart from NP metals made from metallic glasses. In this case, the dealloying of the amorphous precursor promotes the aggregation of the remaining metal atoms into crystalline structures by surface diffusion [9,22].

NP Au is the most important and studied NP metal, thanks to its chemical stability, to the complete solid solubility in Ag lattice – ideal for an NP metal fabrication by dealloying – and to its unique properties. Several applications have been found for NP Au, from catalysis to sensing to nanomechanics [9,23].

In this chapter, the main fabrication methods, properties and applications of NP metals will be discussed and the work done in the thesis will be introduced.

1.1 Fabrication methods of nanoporous metals

As mentioned above, NP metals are commonly fabricated by dealloying. To obtain unimodal pore size distributions, the ideal dealloying should be performed from a single-phase solid solution composed of two or more elements [9]. The elements should have a different tendency to be removed from the alloy in particular conditions. This tendency is governed by the electrochemical potential difference in the case of chemical/electrochemical dealloying [24], by the difference in solubility in another melt metal in the case of the liquid-metal dealloying [25], or by the vapor pressure difference in the case of vapor-phase dealloying [26].

[1] In this field, the term microstructure can be referred to different aspects of the microscopic structure of a material, i.e. to the morphology of ligaments/pores network or to all the features of the crystalline phases present in a material, such as crystal structure and grains orientation and size. In this thesis the term will be always used in the latter connotation.

For an ideal dealloying, some critical points should be satisfied [9,24,27]:

- the dissolution rate of the dissolving element should be comparable to the diffusion rate of the non-dissolving element. The length scale of pores and ligaments can be controlled by tuning the ratio between the two rates. This can be easily done by modulating characteristic parameters of each dealloying method, such as temperature, concentration of the corrosive solution or pressure;
- the difference in the driving force should be large enough to tune the two described rates;
- the dissolving element content in the precursor alloy should be above a specific content, called the parting limit. Below this concentration, the not-dissolving element would rapidly passivate the surface after dealloying of few atomic layers;
- the non-dissolving element should not be oxidized during the dealloying.

The dealloying mechanism has been particularly studied for the ideal case of NP Au produced by an AuAg alloy.

However, NP metals can also be obtained by performing dealloying outside these strict terms which would restrict the possible nanoporous metals to a few, especially noble and high-cost metals. As a result, not all NP metals present the typical bicontinuous network of ligaments and pores but can still possess interesting properties and be suitable for advanced applications [28-32].

The most common method to prepare nanoporous metals is the selective oxidation of the less-noble elements of a precursor alloy, commonly called **Chemical or Electrochemical Dealloying**, depending on whether or not an external potential is used to allow or control the dissolution process. As anticipated before, this method is remarkably suitable for the fabrication of nanoporous noble metals, like Au, Pt, Pd, Ag, Cu from a precursor binary alloy. Although with more efforts, nanoporous bare metals (such as Ni [33], Ti [34], Al [31], Zn[35]) can also be produced by this method. However, the efficient fabrication of these NP metals has not been achieved yet.

Later, another type of dealloying was conceived, the **Liquid Metal Dealloying** (LMD) [25]. This method is based on the difference of solubility in a melted metal between two or more elements of an alloy. The more soluble elements can be dissolved in the metal, while the atoms of the less

soluble alloy components can reorganize in the classical network of interconnected ligaments and pores, in this case occupied by the melt solution. After the shaping of the NP metal, the solidified solution of the melted metal and the dissolved elements can be removed through a proper chemical etching. This last process narrows the number of NP metals that can be produced without being corroded. Moreover, the high temperatures necessary for the use of metallic melts commonly lead to a large coarsening of the porous structure, with characteristic lengths commonly higher than 200 nm [25,36,37].

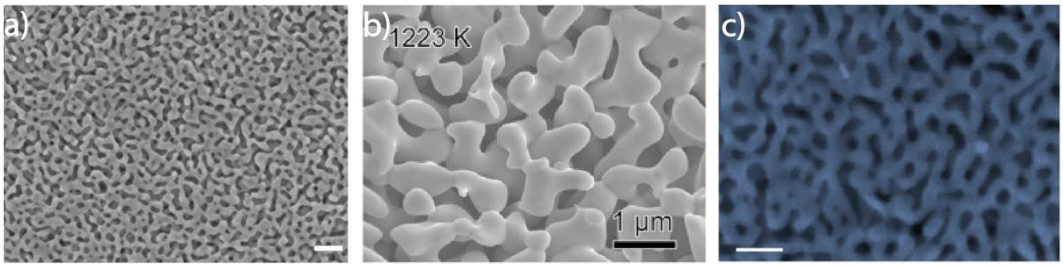

Fig. 1.2 NP metals made by dealloying: a) NP Au made by chemical dealloying, scale bar: 100 nm [38]; b): NP Ti made by Liquid Metal Dealloying, scale bar: 1 µm [25]; c) NP Co made by Vapor Phase Dealloying, scale bar: 200 nm [26].

The described methods present some economic and environmental drawbacks in common, for example, the etching produces chemical waste and the sacrificial metals are difficult to recover.

Recently, a type of dealloying based on the selective sublimation of an alloy component was conceived [26]: indeed, when a difference in vapor pressure between two alloy components exists, it is possible to promote the sublimation of one component during thermal treatment in low-pressure conditions. The introduction of this method, known as **Vapor Phase Dealloying** (VPD), paves the way for the production of new NP metals, with the important benefits that the chemical reactivity plays no role in the process and that there is no need to use other chemicals, apart from the alloy precursors. A limit of this technique is the restricted number of metals that can be sublimated at relatively low temperatures (under 600°C). Therefore, the number of NP metals that can be produced is limited by the number of suitable precursor alloys. shows the typical morphologies of NP metals produced by the three different methods.

Apart from dealloying, other routes are suitable for the fabrication of NP metals, such as through controlled combustion of transition-metal complexes [39] or soft and hard templating [40]. Among all the possible methods, dealloying is surely the most important method [4] thanks to the unique bicontinuous porous structure with tunable characteristic lengths

that can be formed, its relative simplicity and generality and to the possible conversion to large scale production. The vast majority of published papers about NP metals regard materials fabricated through dealloying and the number of published papers and citations per year has increased exponentially since the pioneering work of Erlebacher et al. in 2001 [24]. Therefore, from this point on, the discussion will be referred to those NP metals fabricated by dealloying, unless specified.

1.2 Properties and related applications of NP metals

NP metals show unique and exceptional properties that can find great interest for applications in actuators, electrochemical, electronic and optical sensors, electrochemical energy storage and conversion, green synthesis of organic chemicals, automobile exhaust systems, drug loading and release, photothermal therapy, and diagnostic.

1.2.1 Electronic transport properties and applications

NP metals show good electrical conductivity, which was found to be only 1-2 orders of magnitude lower than that of their bulk counterpart [41]. In addition, they can selectively undergo changes in electrical resistivity when their surface state is perturbed: reversible changes of around 4% and 43 % in double layer and specific surface adsorption charging regimes were observed [42]. The latter effect has been ascribed to the chemisorbed molecules acting as scattering centers for the charge carriers while the first could be also caused by a change in surface charge density [43].

For this reason, NP metals can be used as *electronic sensors*. NP Au nanowires have been used as sensors of octadecanethiol with a sensitivity factor of $1.0 \cdot 10^{-16}$ cm^2 and a change in resistivity of 3% when the molecules adsorb on the sensor surface [44]. NP PdAg alloy with ligament size around 5 nm was instead proven as a fast and reliable sensor for the detection of H_2 [45]. NP Pd, as bulk Pd, is known for its hydrogen storage capacity: when H_2 dissolves in Pd lattice, it changes the electrical resistivity of the material [46].

1.2.2 Mechanical Properties

The mechanical properties of NP metals offer great opportunities: they combine the properties and workability of bulk metals with a much lower density. In addition, the nanostructured size of their ligaments gives NP metals more strength than their bulk counterparts by at least one order of magnitude or more [47], which increases with the decrease of ligament size,

as shown in Fig. 1.3. The following scaling law relating yield stress σ to ligament size s has been proposed by several works [9,20,48,49]:

$$\sigma \approx As^{-m},$$

Eq. 1-1

where A and m are constants.

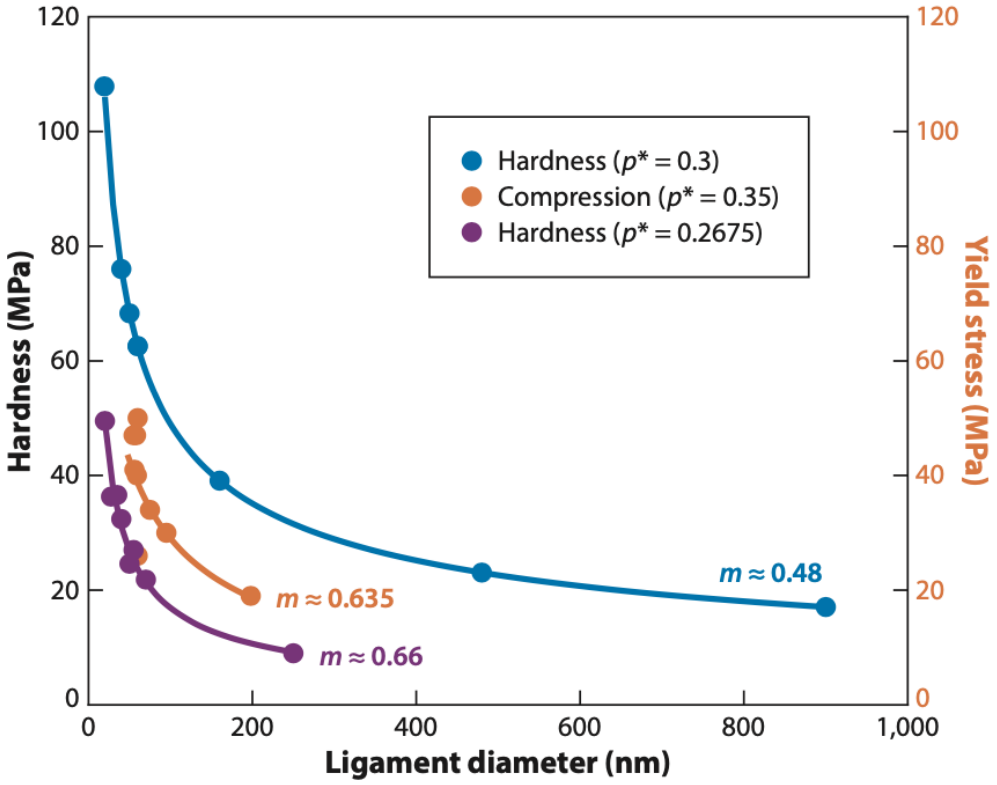

Fig. 1.3 Hardness (blue and purple) and yield stress (orange) values for different ligament diameters. p is referred to the density of the different NP Au samples. Image taken from ref. [9].*

Therefore, NP metals find great interest in the automotive and aerospace sectors, where reliable lightweight high-strength materials are ideal for enhancing the efficiency of the means of transportation while maintaining performances and safety issues, and simultaneously boosting fuel economy [50].

The enhanced strength of NP metals with respect to their bulk counterpart has been ascribed to two mechanisms: firstly, the dispersion of pores and channels across the solid metal brings a strengthening similar to dispersion strengthening typical in solid dispersoids [9]; secondly, the nanostructured size of metal ligaments influences the nucleation and migration of defects under mechanical deformation conditions by suppressing the dislocation activity and resulting in strengthening of the material [51].

Unfortunately, the high theoretical strength expected for nanometric areas of NP metals has never been achieved in macroscopic samples. Fabrication methods invariably result in NP metal structures with a relatively high density of cracks, which make the monolithic sample extremely brittle and unable to bear external mechanical loads [52–56].

This is a point of serious concern for scientists, engineers, and technologists, which hinders the use of monolithic NP metals in the various areas of advanced science and engineering mentioned above.

For this reason, considerable efforts still have to be made to understand the mechanical behavior of NP metals.

1.2.3 Coarsening

As anticipated above, NP metals exhibit coarsening of their pore/ligament network during some processes like dealloying itself, thermal treatments, or during their catalytic activity. This is caused by the diffusion of the metal atoms at the surface. For this reason, dealloying of the same alloy in different acidic or basic solutions brings to different length scales of pores and ligaments by affecting the surface diffusion rate of the metals at the interface. Coarsening can also be affected by the adsorption of different gases at the surface during a thermal treatment, which here too change the surface diffusivity of surface atoms.

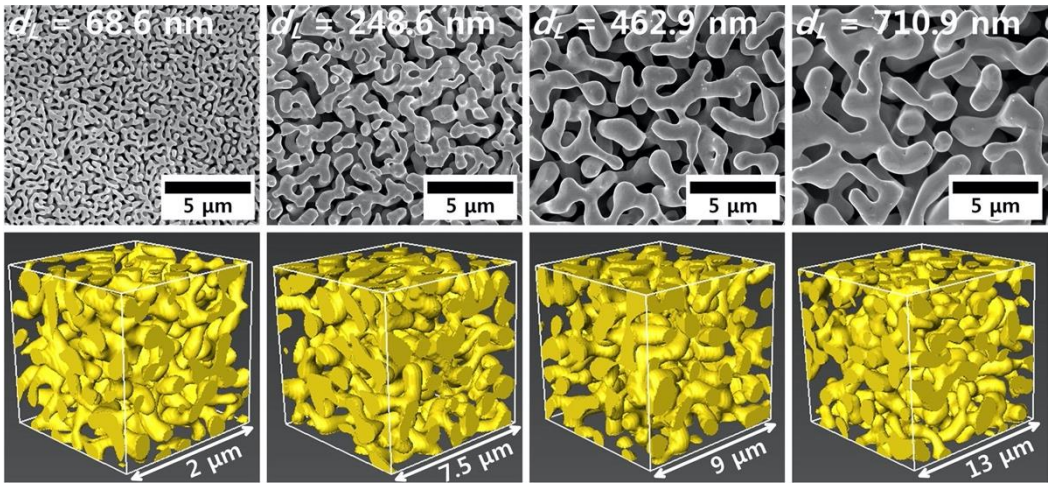

Fig. 1.4 Self-similarity in NP Au coarsening: from left to right, the 2D and 3D morphology of NP Au samples treated at 300, 400, 500, and 600°C for 2h are shown [57].

In coarsening, we find one of those peculiarities that make NP metals so appealing. It enables the fine tuning of the material characteristic lengths from few nm to tens of µm, which become even visible by optical microscopy. This opens up the road to device design with optimized performances for a specific application. However, from the other side, some

applications require NP metals with nanometric characteristic lengths to work at high temperatures or in long-cycles electrochemical processes. This is a critical point because coarsening rapidly causes the increase of the characteristic lengths and with this the drop of its performances, such as its catalytic activity, SERS or MEF efficiency, the mechanical strength, and so on. For this reason, this process has been intensively studied.

NP metal structure is thermodynamically metastable because of its high surface area. For this reason, when the atoms have sufficient mobility, tend to form larger ligaments and pores. The process has been found to proceed in a self-similar structure, as shown in Fig. 1.4, without densification [57]. Nevertheless, other works reported the non-self-similar nature of the process [58]. Kinetic Monte Carlo and Molecular Dynamics simulations explained the coarsening evolution as a result of the complex geometry of the ligaments' network, in which regions of positive, negative, and saddle points curvature can be found. Taking into account these topologies, the simulations indicated that coarsening evolve via pinch-off Rayleigh instabilities to form larger ligaments and that inverse Rayleigh instabilities – a tunnel breaking up into a series of voids – can also occur, explaining the presence of large voids within NP Au ligaments, observed by TEM [59–61].

In several papers, the ligament diameter λ of NP Au is found to grow with a power law respect to the time t [8,62,63]:

$$\lambda = (ktD_s)^n, \qquad \textit{Eq. 1-2}$$

where k is a proportionality constant, n is the coarsening exponent and D_s is surface self-diffusivity. D_s can be written in the Arrhenius form, typical of thermally activated processes:

$$D_S = D_0 e^{-\left(\frac{E_a}{k_B T}\right)}, \qquad \textit{Eq. 1-3}$$

Where D_0 is a constant, E_a is the activation energy. Therefore, becomes:

$$\lambda = At^n e^{-\frac{nE_a}{k_B T}}, \qquad \textit{Eq. 1-4}$$

Where $A = (kD_0)^n$.

However, there are several other reports in which the data don't fit well this relationship, even if there are no important differences in processing conditions and morphology features of the NP metal [52]. This suggests the occurrence of secondary processes during annealing and of hidden parameters that heavily influence those processes.

1.2.4 Catalytic properties and applications

NP metals show very interesting catalytic properties for different types of reactions. For example, NP Au has been shown to be highly active towards the oxidation of the poisonous CO, the selective oxidation of alcohols, or the reduction of CO_2. NP Pt can instead promote the reduction of O_2. Several detailed reviews can be found about NP metals catalysis [9,64–66]. Here, we dwell on some of the most studied reactions, where the relationship between NP metals' structure and catalytic activity has been extensively explored.

NP Au has been found with a very high catalytic activity and selectivity for several oxidation reactions, either in gas phase either in liquid phase. The first oxidation reaction which gained huge interest was that of CO at low temperatures, even down to -30°C [65]. Since then, it is still the most studied reaction catalyzed by NP Au [64,66,67]. Later, other reactions such as the oxidation of alcohols [68] and hydroxylamines [69], or the selective oxidative coupling of alcohols to corresponding formates [70] were observed. In particular, the very high selectivity and catalytic activity higher than that of Au nanoparticles with the same feature sizes has attracted the attention of researchers since 2006 [65]. Moreover, NP Au is not prone to agglomeration, a phenomenon that causes the drop in the catalytic activity of Au nanoparticles. These aspects make NP Au a very promising catalyst: for example, its activity toward CO oxidation can be exploited in automobile exhaust systems [65] and the catalytic activity and excellent selectivity of towards organic reactions, such as methanol oxidation to methyl formate or benzyl alcohol to benzaldehyde [68,70], make it suitable for green catalysts in chemical synthesis. Commonly, any oxidation over the Au surface can happen only with the presence of active oxygen at the surface. This is believed to be the first and key step in any catalytic cycle for NP Au too [64]. How NP Au adsorbs and dissociates molecular oxygen is still under discussion [64,71,72]. The high catalytic activity of NP Au towards oxidation reactions is commonly associated with the high number of low-coordinated Au atoms on the NP Au surface [9,73], attributable to the nanometric size and curvatures of NP Au ligaments. Indeed, it has been calculated that the number of low-coordinated atoms on NP Au ligaments is higher than that of those present on Au nanoparticles with the same sizes (see Fig. 1.5) [74]. Besides, when the structure coarsens to higher ligament sizes, causing a decrease in the fraction of low-coordinated atoms at the surface, the catalytic activity of NP Au falls until vanishing [64].

Usually, NP Au is produced from an Ag-rich precursor alloy and a residual concentration from tens to 0.1 percent is always present in the dealloyed

material [9,64]. Its role in the catalytic activity of NP Au is still unclear. Ag sites could bind to oxygen more strongly than Au ones, promoting its dissociation and so the oxidation of molecules adsorbed on Au sites. However, this cannot explain itself the catalytic behavior of NP Au. Indeed, NP Au produced with other strategies without Ag impurities, still present high catalytic activity [75]. Since the surface state of Ag impurities is not known, its influence on the catalytic properties of NP Au is difficult to understand and more studies are still necessary for this purpose [64].

From the other side, the relevance of low-coordinated Au atoms for both the catalytic activity and the selectivity is not in question. Besides, recent papers reported that the catalytic activity of NP Au can be enhanced by promoting

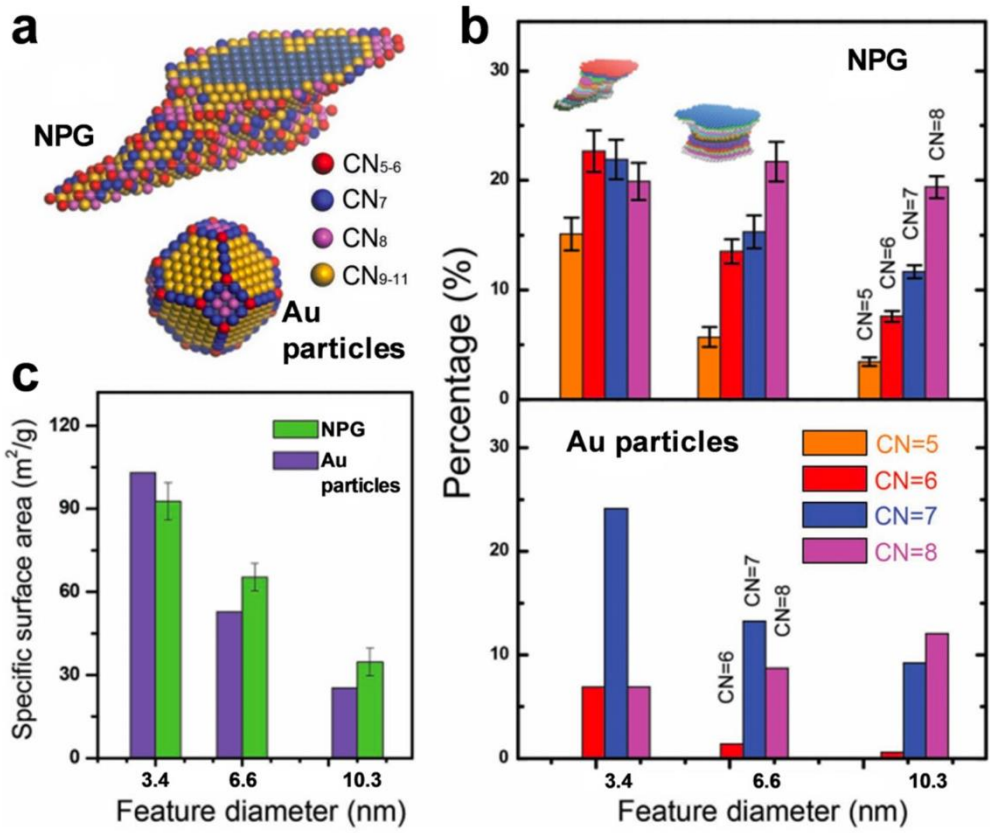

Fig. 1.5 Quantitative calculations for low-coordinated surface atoms on NPG ligaments and Au nanoparticles. a) 3D atomic configurations of an NPG ligament and a truncated octahedral Au nanoparticle. b) Relation between the number fraction of low-coordinated surface atoms and the equivalent radii of Au ligaments and particles. c) Specific surface area as a function of the equivalent radii of NPG ligaments and nanoparticles [74].

the formation of particular Au facets on the surface of NP Au through chemical or electrochemical processes [21,76]. This type of surface engineering can be performed both during dealloying, both after the dealloying. It is therefore possible to renovate the surface structure after its

changes during catalytic cycles, increasing the number of cycles NP Au can be used.

While the origin of the catalytic activity of NP metals surely comes from the nanostructured features of their ligaments, at the same time the nanostructured size of pores hampers the mass transport through the channels, slowing down the reaction rates. For this reason, NP metals with multimodal pore sizes, as that shown in Fig. 1.6, are found to be better catalysts, by combining the enhanced mass transport through larger pores with the high catalytic activity arising from the nanostructured features [77,78].

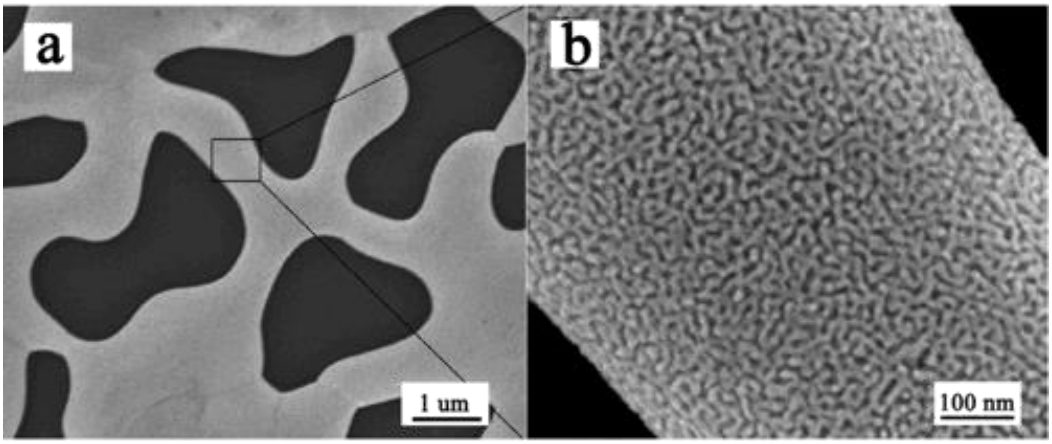

Fig. 1.6 NP Au with multimodal pore size distribution: a) low magnification SEM image with pores of few µm; b) higher magnification image of macro-ligaments of a) displaying nanometric ligaments and pores [78].

Apart from NP Au, other NP metals have shown interesting catalytic activity, such as NP Cu [79], NP Pd [80] and NP Ag [81]. As for NP Au, the low-coordinated atoms are the source of the catalytic activity, and so the characteristic lengths of the porous structure strongly influence the activity. Notably, NP alloys have been studied recently and gathered great interest. NP Au-Pd alloy was found to behave as a better catalyst than NP Au and NP Pd for highly chemoselective 1,4-hydrosilylation of conjugated cyclic enones with hydrosilane [82]. On the other hand, NP NiCu alloy possesses high catalytic activity and selectivity for the non-oxidative dehydrogenation of ethanol to acetaldehyde [83]. Recently, NP NiCuMnO was proposed as a low-cost and stable catalyst for NO reduction and CO oxidation [84].

1.2.5 Electrocatalytic properties and applications for energy conversion and sensing

NP metals' high surface area, good electrical conductivity, and interconnected ligaments and pores that allow chemical species to flow into

the electrode, are ideal features for electrocatalysis. Besides, NP metals have shown great efficiency, sometimes higher than commercial counterparts, as electrocatalysts [4,85].

Fuel cells enable direct and spontaneous conversion of chemical energy contained in fuel and oxidants to electrical energy. The advantages of these devices are: low or zero emissions, high efficiency, flexibility in output power levels that can be generated from the same system of cells, and high stability. Among the various types of possible fuel cells, NP metals are particularly promising as electrodes for polymer electrolyte membrane fuel cells thanks to their outstanding electrocatalytic activity. Hydrogen-Fuel cells, direct methanol fuel cells, and direct formic acid fuel cells have been particularly studied. Pt or Pt-based catalysts are the most used and efficient electrodes in fuel cells. However, Pt devices life is limited by poisoning from carbonaceous species like CO, which adsorb on the metal surface and dramatically decrease its efficiency. This aspect, in addition to the high costs and limited reserve of Pt on earth, makes the search for efficient catalysts with low or no loading of Pt a very active research area [4,86].

NP Au shows a great catalytic activity for methanol electrooxidation, that can be further enhanced through the deposition of tiny amounts of Pt [87] or a Pt layer [88]. From the latter, an electrocatalytic activity greater than that of commercial Pt/C was achieved. NP Au-Pt electrocatalysts were further studied to achieve optimal results with ultralow Pt loading and high stability [5,89]. Moreover, the poisoning of the surface was greatly reduced by suppressing the adsorption of carbonaceous species like CO thanks to the catalytic activity of Au towards their oxidation. Other interesting results were obtained from NP metals made of Pt alloyed with other elements like Cu, Co, and Ni, whose presence is fundamental for the decrease of the poisoning effect [90,91]. Recently NP Pd-based alloys were also proven to be efficient electrocatalysts of electrochemical reduction of CO_2 to formate [92]. Here too, alloying elements like Cu, Co, Ni and Ag were used for making the electrocatalyst tolerant to CO poisoning and reducing the Pt

loading. The electrocatalytic activity for hydrogen evolution reaction (HER) of NP Ni films has been intensively studied for water splitting [93].

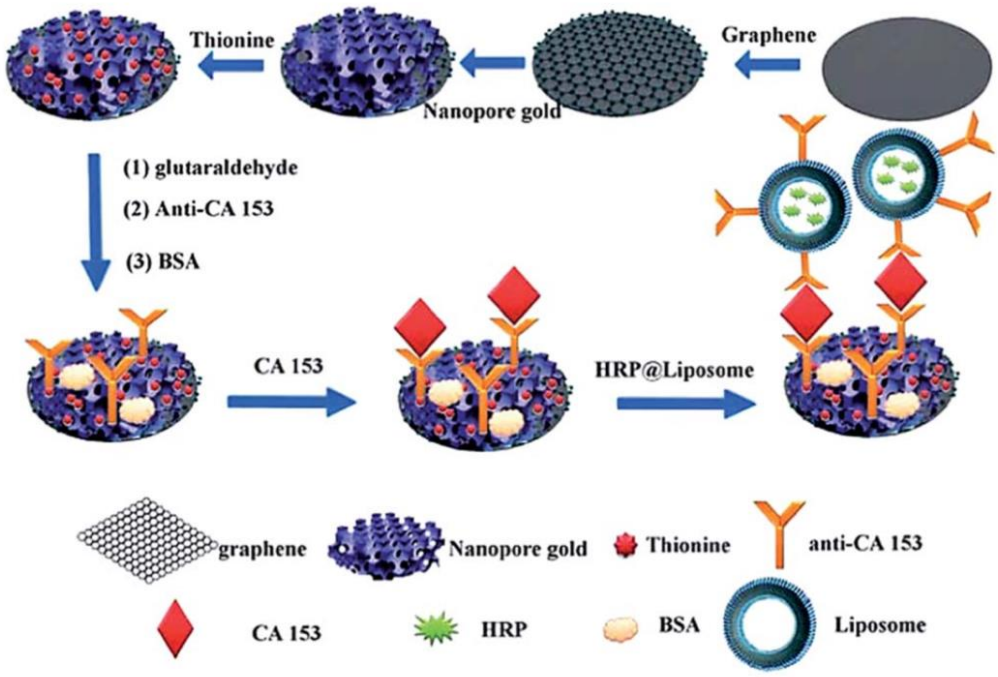

Fig. 1.7 Schematic illustration of immunosensor assembling based on NP Au/graphene hybrid platform and horseradish peroxidase-encapsulated liposomes as labels for the sensitive detection of cancer antigen 15-3 [94].

The high surface area and electrocatalytic activity of NP metals are also suitable for *electrochemical sensing* with high sensitivity and selectivity. Nonenzymatic sensors for small molecules, such as glucose, hydrazine, nicotinamide adenine dinucleotide (NADH), H_2O_2, and dopamine have been designed with NP Au as an integral part of the device [13]. NP Au has been used for the electrochemical detection of the organic pollutant p-nitrophenol (p-NP) with high sensitivity and good selectivity [95]. Since the electrocatalytic activity of NP Au comes from the surface atoms, a more cost-effective NP metal made of Cu core and an Au shell was proposed for the nonenzymatic sensing of glucose [96]. Moreover, other NP metals and alloys, such as NP Ag, NP Pd, and NP PtAg, have been studied for this purpose [97–99]. NP metals can also be used as supports for enzyme immobilization to extend the sensing applications [100–103], or for antibodies immobilization in immunosensors (See Fig. 1.7) [94,104–107]. NP PtCo alloy was used as substrate of an immunosensor for the enzyme-free detection of zeranol, with a very high detection limit up to 13 pg/mL [104].

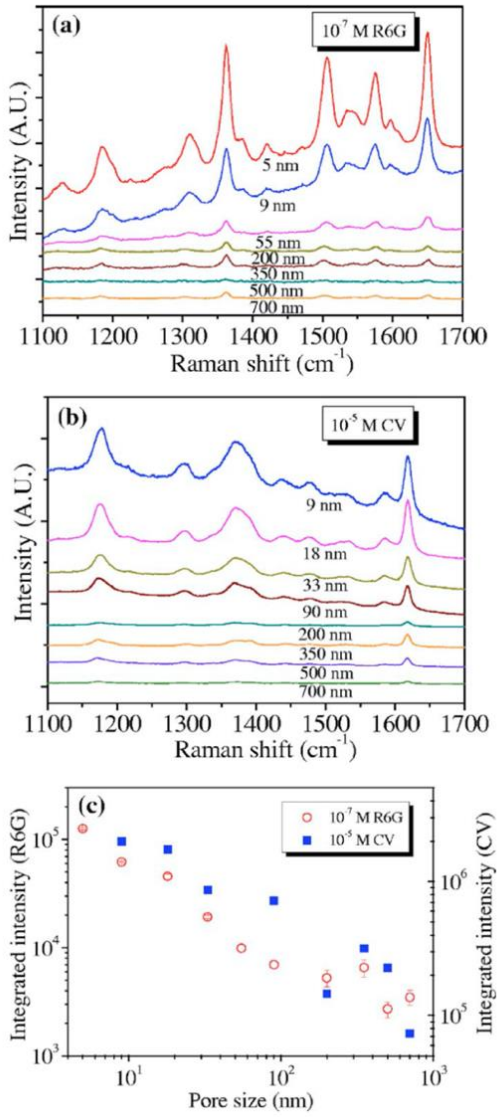

Fig. 1.8 SERS spectra of Rhodamine 6G (R6G) (a) and Crystal Violet (CV) (b) on NP Au with different pore sizes: the enhancement factor increases as pore size decreases (c) [108].

1.2.6 Optical properties and applications

Thanks to their characteristic lengths, NP metals show interesting optical properties that make them suitable for a wide set of applications in various technological areas.

As for metal nanostructures, NP metals' optical properties differ significantly from those of their bulk counterparts. Their uniqueness can be exploited for detection of analytes through Surface Enhanced Raman Spectroscopy (SERS), Metal Enhanced Fluorescence (MEF), and Infrared (IR) absorption spectroscopy and for biomedical applications.

Due to the nanometric size of the ligaments, surface plasmons' energetic levels change with the size and shape of the ligaments and with the surrounding environment, modifying the metal color. When excited at frequencies near plasmon resonance absorption peak, Localized Surface Plasmon Resonance (LSPR) occurs, resulting in a great enhancement of the electromagnetic (EM) field at the metal/dielectric interface, which rapidly decreases with the distance from the surface [109].

For this reason, molecules adsorbed on the metal surface perceive enhanced EM field and can generate enhanced Raman signals of up to 10^{12} times. This effect is harnessed in SERS, where detection limits up to the single-molecule can be achieved. NP noble metals, such as Au, Ag, and Cu have been proven to be efficient SERS substrates. Since the SERS enhancement factor (EF) is remarkably higher in the “hot spots” between metal nanostructures, the pore size plays a predominant role in the EF. Several studies indicate that smaller pore sizes lead to stronger enhancements (see Fig. 1.8) [13,108], although sometimes better results are obtained by dealloying NP metals for more time, resulting in larger pore sizes but with less, SERS-inactive impurities [13,16]. Apart from noble metals, NP Al and NP AlMg alloy were proposed as SERS substrates in the UV spectral range [110], where common NP noble metals are not suitable. This can be particularly interesting in the field of sensing and catalysis, since the major part of organic molecules shows major absorption in the UV range [110]. SERS-based sensors made with NP Au have been explored for the optical sensing of Hg^{2+} traces with an ultralow detection limit of 1 pM, comparable with the most sensitive optical detectors of Hg^{2+}, with excellent selectivity [111]. Another work reported that patterned NP Au nano-disks can be used for in-situ monitoring of DNA hybridization through SERS [112].

Similarly to SERS, NP metals can manifest MEF, i.e. the fluorescence enhancement of a molecule or nanomaterial deposited on a metal surface [17,110,113]. As for SERS, the enhancement of the fluorescence is due to the enhancement of the electromagnetic field near the plasmonic surface. However, while for SERS the efficiency increases as the analyte-metal distance decreases, in this case, the direct contact between the two materials can bring to non-radiative charge transfer, and so to fluorescence quenching. Therefore, a spacer between metal and analyte could be necessary, according to the system [114]. NP Au with silica thin films was produced and showed that an optimal distance between the metal surface and Rhodamine 6G molecules should lie around 20 nm [114]. Instead, MEF of quantum dots deposited on NP Au was exploited for the development of a sensitive and quantitative H1N1 virus sensor, as shown in Fig. 1.9 [115].

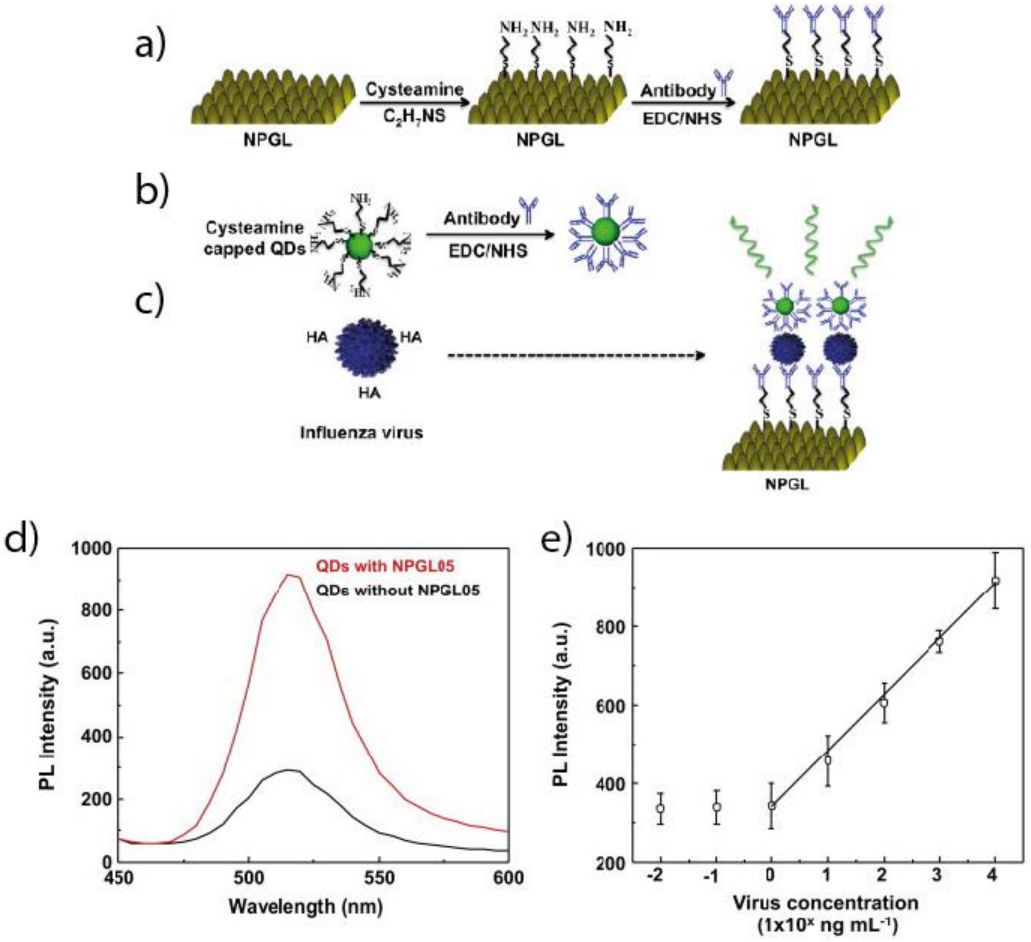

Fig. 1.9 Schematic illustration of virus detection using NP Au leaf (NPGL). The NPGL (a) and quantum dots (QDs) (b) were firstly conjugated with anti-hemagglutinin (HA) antibodies (anti-HA Ab, Y shape). Then anti-HA Ab-conjugated with NPGL and QDs form complex (c) in presence of HA on the surface of influenza virus, finally enhancing photoluminescence (PL) intensity (d). Calibration curve for quantitative determination of virus concentration (e). Image adapted from [115].

By tuning the plasmonic absorption of NP Au, it was observed that it can also be used as a substrate for IR chemical and refractive index sensing [116,117].

SPR is also responsible for NP metals photocatalysis. Localized surface plasmons can also decay into charge carriers, called hot carriers, which can be transferred to molecules or other species near the metal surface and promote chemical reactions [118–120].

In some cases, NP metals exhibit other very interesting optical properties, such as extraordinary light transmittance of thin films [121] and photothermal effect [122]. The latter is widely studied in biomedical research, such as for drug delivery and cancer therapy. Recently, some studies reporting also the use of NP metals for applications based on this effect were released. NP Au nanowires motors were used for drug loading,

transport, and delivery. NP Au disk arrays induce the inactivation of heat-resistant bacteria through photothermal effect with NIR irradiation [123]. In addition, drug-loaded NP Au nanoshells produced by a template method showed a synergistic chemo-photothermal effect in in-vivo tumor therapy [124].

1.2.7 Actuation

Materials that respond to a stimulus, such as an electrical potential, with a reversible volume change can be used as actuators. There is a wide variety of materials with different sets of properties of interest for actuation, such as the common piezoelectric ceramics. Among them, materials with a very high surface area, such as NP metals and carbon materials, are suitable for actuation thanks to their high response to surface state changes. When the interatomic bond strength at the surface change, the surface stresses of the metal carry a mechanical strain. Typically, the surface stress is induced in an electrochemical cell where the NP metal is an electrode, by a transfer of charges to or from the space-charge region at the surface of the metal, which constitutes a layer of the electrochemical double-layer. The change in the local charge density results in a change of surface stress of the metal. Strain amplitudes of up to 2 % can be achieved and even observed to the naked eye. These values are outstanding, comparable to those of commercial actuator materials [125]. Also in this case, smaller ligament sizes lead to major effects, as shown in Fig. 1.10 [126].

Actuators made of NP Au [125], Pt [127], Au-Pt [128], Pd [129], Ag [130] and Au-polymer composite [131] were fabricated. However, recently NP Ni-based devices showed outstanding performances; that, in addition to costs of fabrication very lower in comparison with those of noble metals, makes this material very promising for future applications [150]. In this paper, for the first time, a high level of long-term stability was achieved, with a 70 % of strain retention after 10,000 cycles for the NP Ni actuator. Moreover, the actuator manifested a very high reversible strain of about 2 % and one of the higher work densities for actuators materials. Apart from electrochemical actuation, some studies reported that other mechanisms can promote actuation. Biener et al. found that the surface stresses of the NP metal can be modulated in a chemical way, by alternating adsorption of different gases at the surface [132]. With this method, they obtained a strain amplitude of 0.5 %. Moreover, Yang et al. recently demonstrated that NP Au photothermal effect can generate heat-mediated actuation in the material [133].

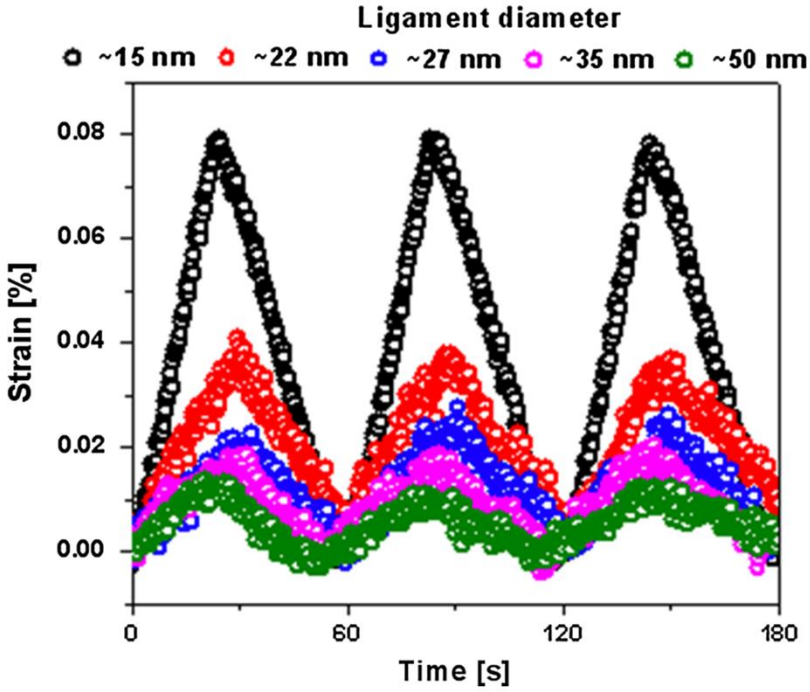

Fig. 1.10 Ligament size dependence of the charge-induced strain in nanoporous metals. The strain amplitude recorded on five NPG samples with different ligament sizes decreases with the increasing ligament size [126].

1.2.8 Electrochemical energy storage

The development of more efficient Li-ion batteries and supercapacitors represent an integral part of the transition process to renewable energy supply. NP metals, thanks to their good electric conductivity, high surface area, and the particular convex/concave curvature of ligaments represent promising materials for these applications as electrodes or supports for electrode deposition.

Supercapacitors have attracted attention for their capability of energy storage and extremely rapid charging and discharging. NP metals have been widely investigated as electrodes for supercapacitors [4,10,134,135]. Supercapacitors with NP Au as electrodes were studied by Lang et al. [135] with good performances both in KOH aqueous solution, both in ionic liquid electrolyte, in which the system displayed improved operating voltage range, from about 1 V to 2V. Supercapacitors based also on the much more economic NP Ni were produced both in organic solvents [136] and in ionic liquids [137]. Although NP metals have shown good perspectives as supercapacitor electrodes, their performances can be still improved by oxidation/oxyhydroxidation of the surface [28,138,139] or by the production of hybrid systems with active materials in the surface of NP metals, such as

metal oxides [11,140,141] and polymers [142]. Among all, NP Au/MnO_2 hybrid system represents the most promising and studied system, for its extraordinary high levels of power delivery with high-energy storage densities [11,140]. An illustration of NP Au/MnO_2-based supercapacitor is shown in Fig. 1.11.

Nanoporous electrodes for *Li-ion batteries* are convenient for several reasons: apart from their already mentioned advantages for any electrochemical system, the nanoscale porosity comports the reduced Li-ion diffusion length between electrolyte and electrode; moreover, the free space occupied by pores supports large volume expansions during discharging-charging processes. Thanks to their properties, NP metals have been studied as electrodes, such as NP Sn/SnSb [143], or as 3D scaffolds for the deposition of other electrode materials, such as metals [144], metal oxides [145], metal sulfides [146] and insertion materials [147].

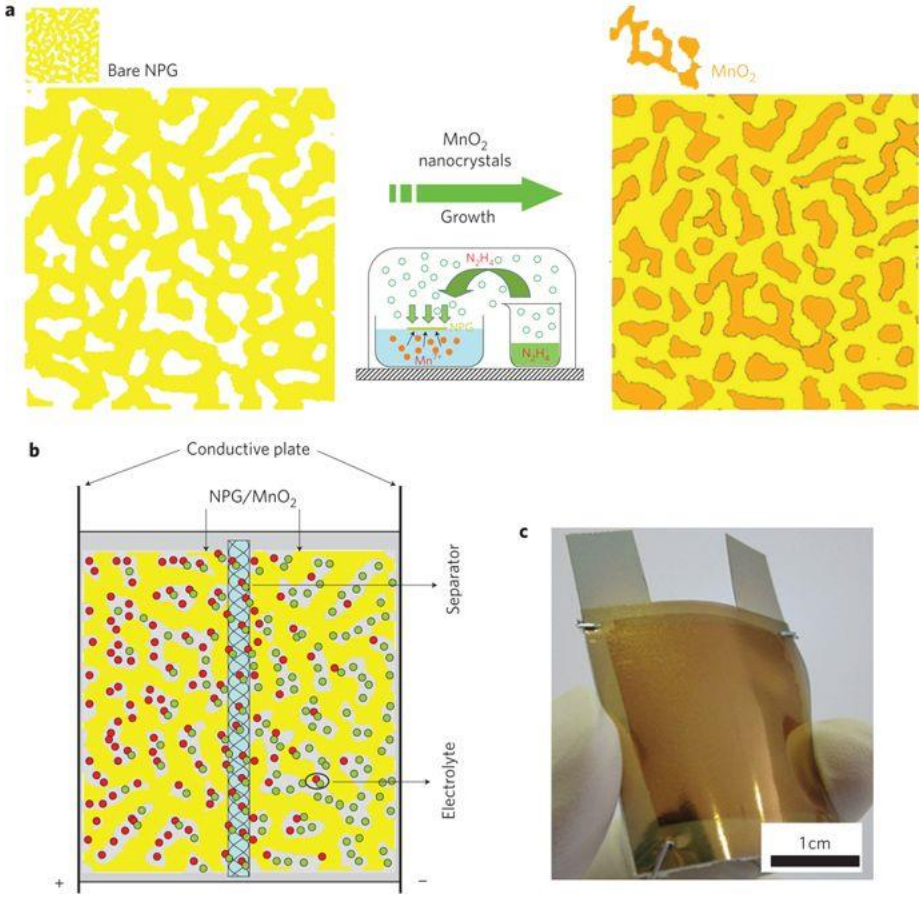

Fig. 1.11 Fabrication of NP Au/MnO_2 composite by MnO_2 growth inside NP Au pores (a). Supercapacitor device constructed with NP Au/MnO_2 films as electrodes, aqueous Li_2SO_4 as electrolyte, and tissue paper as separator (b). Photograph of NP Au/MnO_2-based supercapacitor (c) [11].

1.2.9 Properties of Nanoporous Metals in Composite Structures

As already mentioned, NP metals as self-supported high surface area materials with optimal electrical conductivity, represent ideal supports to realize functional composite structures. These structures can be highly interesting as they can be used for improving properties both of the NP metal or the deposited material, or to trigger unique phenomena that can't happen with just one of the two elements of the system. NP metals can be combined with other substances, such as metal nanostructures, with metal oxide nanostructures and organic compounds.

Metal nanostructures deposited on NP metals can result in stronger SERS enhancements and broadened exploitable wavelength spectrum [148]. Moreover, as anticipated before, Pt nanostructures in form of clusters or ultrathin layers can greatly enhance the catalytic or electrocatalytic activity of NP Au [89].

Metal oxide nanostructures on NP metals can heavily influence their properties. In addition to the already mentioned NP Au/MnO_2 system for supercapacitors electrodes, metal oxide nanoparticles such as Al_2O_3 and TiO_2 can stabilize the NP metal, increasing the temperature ranges and times in which the metal can be used without losing its properties. Besides, catalytically active metal oxide nanostructures, such as TiO_2 and CuO/CuO_2, can enhance the activity of the NP metal, by adsorbing chemical species which will selectively react thanks to the catalytic activity of the NP metal [75,149,150]. This system, commonly called "inverse catalyst", resembles the more common opposite system where metal nanoparticles are deposited on metal oxide supports that are commonly necessary for enabling the catalytic activity of the metal.

NP metals can be coupled also with organic compounds. They can be used to functionalize the surface for specific catalytic and sensing applications [151]. Polymers can also greatly enhance the macroscopic ductility of the NP metals, as in the case of NP Au, which exhibited tensile ductility when different polymers, such as epoxy resin and polyurethane were impregnated in the metallic network [152]. These composites match the high strength of NP Au with the macroscopic tensile ductility arising from the polymer coating. NP Au coated with polyaniline has been shown to perform actuation without the use of any electrolyte, thanks to the presence of sulfate anions as dopants in the polymer matrix, which can tune the surface stress of the NP metal [131]. This mechanism of actuation allows to 3-fold enhance the strain rate of actuation, commonly limited by the low ionic conductivity in

metal/electrolyte actuators. Moreover, it prevents coarsening during electrochemical redox reactions.

Despite the fascinating outlook, the exit of NP metal-based devices in the global market is hampered by some problems:

- At present, a substantial number of studies about NP metals and their properties is restricted to a limited set of elements, such as Ag, Pt, Pd, Cu, Ni, and mostly Au [5].
- Looking at the array of papers on NP metals, we can find wide variability in the values of important properties and, more importantly, in the relationship with other properties and the material structure. This implies the existence of some hidden parameters which are not taken into account while they probably greatly influence the properties of the materials [8]. To solve some critical points, such as the mechanical brittleness and thermal and electrochemical stability, a deep understanding of the structure-properties relationship is of paramount importance.
- NP metal foams exhibit unique properties when combined with other materials, thanks to their interaction. More suitable composite systems can be designed and the set-off interactions between NP metal and the other component(s) should be pointed out and understood to design proper devices for suitable applications.

The following chapters present the work done in this thesis, intending to address these important issues.

In **Chapter 2,** the preparative of different NP metals is presented. In AuAg alloys, Au content higher than 45 at. % is commonly considered the parting limit above which dealloying can't proceed. Here we report that, even if the process is heavily slowed down, long dealloying times can bring to the formation of a nanoporous layer in an alloy with Au content of 50 at. %. Moreover, we performed the fabrication of an NP Au/graphene composite for future possible applications in advanced fields, such as catalysis, electrochemical energy storage and conversion, sensing, and SERS. Finally, the fabrication of NP Cu from a mechanically alloyed CuZn precursor is shown, with the aim of finding new procedures for improving the fabrication of this material from low-cost Zn-based alloys.

In **Chapter 3**, we discuss the coarsening behavior of NP Au by literature data analysis and by experimental work. We found that densification during thermal annealing is more common in low-dimensional systems. In addition, we studied the coarsening of nanocrystalline NP Au dealloyed from a

mechanically alloyed AuAg precursor. We found that nanocrystalline NP Au possesses lower thermal stability compared to literature data and to the same material prepared by annealing the precursor alloy before dealloying, for increasing its grain sizes. We concluded that the microstructure of the precursor alloy heavily influences the thermal stability of the NP metal formed.

Chapter 4 is devoted to the comprehension of the phenomenon that causes discoloration of methyl orange aqueous solutions placed in contact with nanoporous gold. Methyl orange is an azo dye, commonly used in the degradation studies of this class of compounds, to which several toxic ones belong. It was previously observed that when an NP Au sample is immersed in a dilute methyl orange solution, the concentration of the dye in the solution decreases. This process could be caused by a catalytic degradation of the dye or by simple adsorption inside nanoporous gold pores. Through several experiments, we show that, even if traces of degradation products were found, an important part of disappeared methyl orange was adsorbed in the NP Au monolith and could be desorbed again.

In **Chapter 5**, we prepared two systems combining NP Au and perovskite nanocrystals to create a suitable metal-semiconductor heterojunction for photocatalysis, photodetection, and photovoltaic devices. The perovskite degradation phenomenon is observed when the NP Au powder is mixed to the hexane suspension of nanocrystals, while the charge separation efficiency is increased by synthesizing the nanocrystals directly on the Au porous surface. The analysis of the structural and optical properties evidences an energy transfer efficiency of 47%, with high structural stability of the hybrid system.

In **Chapter 6**, we present the effectiveness of Vapor Phase Dealloying to fabricate a hierarchical nanoporous aluminum (NP Al) made of different pore size classes from a few to thousands of nm, with a high surface area of 73 m^2/g. Moreover, a fractal model was designed for the understanding and prediction of some important properties of nanoporous aluminum. As a first validation, we compared the predicted Young's modulus with the value measured by nanoindentation tests, obtaining an optimal correspondence.

In **Chapter 7**, a still in-progress work is presented: we have used SEM images of NP Au to prepare macroscopic 2D reconstructions of its porous morphology to study the effects of ligament/pore geometry on the mechanical response of the specimens. For this purpose, we performed Digital Image Correlation and Extensometer measurements during tensile tests, and Finite Element Method simulations. Preliminary results show that

the mechanical behavior of the material is locally heterogeneous and further studies will be devoted to revealing the topology features correlated to such different responses.

References

[1] K. Ishizaki, S. Komarneni, M. Nanko, Introduction, in: Porous Mater., Materials, Springer, 1998: pp. 1–11. https://doi.org/10.1007/978-1-4615-5811-8_1.

[2] G.Q. Lu, X.S.S. Zhao, Nanoporous Materials: Science and Engineering, PUBLISHED BY IMPERIAL COLLEGE PRESS AND DISTRIBUTED BY WORLD SCIENTIFIC PUBLISHING CO., 2004. https://doi.org/10.1142/P181.

[3] R. Vajtai, Springer handbook of nanomaterials, 2013. https://doi.org/10.1007/978-3-642-20595-8.

[4] Y. Ding, Z. Zhang, Introduction to Nanoporous Metals, in: Nanoporous Met. Adv. Energy Technol., Springer International Publishing, 2016: pp. 1–35. https://doi.org/10.1007/978-3-319-29749-1_1.

[5] J. Zhang, C.M. Li, Nanoporous metals: Fabrication strategies and advanced electrochemical applications in catalysis, sensing and energy systems, Chem. Soc. Rev. 41 (2012) 7016–7031. https://doi.org/10.1039/c2cs35210a.

[6] Y. Ding, Z. Zhang, Nanoporous metals for advanced energy technologies, 2016. https://doi.org/10.1007/978-3-319-29749-1.

[7] Front cover, Nanoscale. 8 (2016) 19405–19405. https://doi.org/10.1039/C6NR90252A.

[8] H.J. Jin, J. Weissmüller, Bulk nanoporous metal for actuation, Adv. Eng. Mater. 12 (2010) 714–723. https://doi.org/10.1002/adem.200900329.

[9] I. McCue, E. Benn, B. Gaskey, J. Erlebacher, Dealloying and Dealloyed Materials, Annu. Rev. Mater. Res. 46 (2016) 263–286. https://doi.org/https://doi.org/10.1146/annurev-matsci-070115-031739.

[10] M. Liu, J. Zhao, Z. Luo, Z. Sun, N. Pan, H. Ding, X. Wang, Unveiling Solvent-Related Effect on Phase Transformations in CsBr-PbBr2 System: Coordination and Ratio of Precursors, Chem. Mater. 30 (2018) 5846–5852. https://doi.org/10.1021/acs.chemmater.8b00537.

[11] H.J. Jin, J. Weissmüller, Bulk nanoporous metal for actuation, Adv. Eng. Mater. 12 (2010) 714–723. https://doi.org/10.1002/adem.200900329.

[12] H.J. Jin, J. Weissmüller, Bulk nanoporous metal for actuation, Adv. Eng. Mater. 12 (2010) 714–723. https://doi.org/10.1002/adem.200900329.

[13] F. Ruffino, M.G. Grimaldi, Nanoporous Gold-Based Sensing, Coatings 2020, Vol. 10, Page 899. 10 (2020) 899. https://doi.org/10.3390/COATINGS10090899.

[14] S.O. Kucheyev, J.R. Hayes, J. Biener, T. Huser, C.E. Talley, A. V. Hamza, Surface-enhanced Raman scattering on nanoporous Au, Appl. Phys. Lett. 89 (2006) 053102. https://doi.org/10.1063/1.2260828.

[15] C. Ma, M.J. Trujillo, J.P. Camden, Nanoporous Silver Film Fabricated by Oxygen Plasma: A Facile Approach for SERS Substrates, ACS Appl. Mater. Interfaces. 8 (2016) 23978–23984. https://doi.org/10.1021/acsami.6b08191.

[16] L.Y. Chen, J.S. Yu, T. Fujita, M.W. Chen, Nanoporous copper with tunable nanoporosity for SERS applications, Adv. Funct. Mater. 19 (2009) 1221–1226. https://doi.org/10.1002/adfm.200801239.

[17] L. Zhang, Y. Song, T. Fujita, Y. Zhang, M. Chen, T. Wang, Large Enhancement of Quantum Dot Fluorescence by Highly Scalable Nanoporous Gold, Adv. Mater. 26 (2014) 1289–1294. https://doi.org/10.1002/adma.201304503.

[18] X.Y. Lang, P.F. Guan, T. Fujita, M.W. Chen, Tailored nanoporous gold for ultrahigh fluorescence enhancement, Phys. Chem. Chem. Phys. 13 (2011) 3795–3799. https://doi.org/10.1039/c0cp01571g.

[19] B.A.M. Hodge, J.R. Hayes, J.A. Caro, J. Biener, A. V. Hamza, Characterization and Mechanical Behavior of Nanoporous Gold **, Adv. Eng. Mater. 8 (2006) 853–857. https://doi.org/10.1002/adem.200600079.

[20] G. Pia, F. Delogu, Mechanical Properties of Nanoporous Au: From Empirical Evidence to Phenomenological Modeling, Metals (Basel). 5 (2015) 1665–1694. https://doi.org/10.3390/met5031665.

[21] Z. Wang, S. Ning, P. Liu, Y. Ding, A. Hirata, T. Fujita, M. Chen, Tuning Surface Structure of 3D Nanoporous Gold by Surfactant-Free Electrochemical Potential Cycling, Adv. Mater. 29 (2017) 1–7. https://doi.org/10.1002/adma.201703601.

[22] F. Scaglione, F. Celegato, P. Rizzi, L. Battezzati, A comparison of de-alloying crystalline and amorphous multicomponent Au alloys, Intermetallics. 66 (2015) 82–87. https://doi.org/10.1016/j.intermet.2015.06.022.

[23] A. Wittstock, J. Biener, J. Erlebacher, M. Baumer, Nanoporous Gold: From an Ancient Technology to a High-Tech Material, 2012.

[24] J. Erlebacher, M.J. Aziz, A. Karma, N. Dimitrov, K. Sieradzki, Evolution of nanoporosity in dealloying, Nature. 410 (2001) 450–453. https://doi.org/10.1038/35068529.

[25] T. Wada, K. Yubuta, A. Inoue, H. Kato, Dealloying by metallic melt, Mater. Lett. 65 (2011) 1076–1078. https://doi.org/10.1016/j.matlet.2011.01.054.

[26] Z. Lu, C. Li, J. Han, F. Zhang, P. Liu, H. Wang, Z. Wang, C. Cheng, L. Chen, A. Hirata, T. Fujita, J. Erlebacher, M. Chen, Three-dimensional bicontinuous nanoporous materials by vapor phase dealloying, Nat. Commun. 9 (2018) 1–7. https://doi.org/10.1038/s41467-017-02167-y.

[27] J. Erlebacher, K. Sieradzki, Pattern formation during dealloying, Scr. Mater. 49 (2003) 991–996. https://doi.org/10.1016/S1359-6462(03)00471-8.

[28] J. Kang, A. Hirata, L. Chen, S. Zhu, T. Fujita, M. Chen, Extraordinary Supercapacitor Performance of a Multicomponent and Mixed-Valence Oxyhydroxide, Angew. Chemie. 127 (2015) 8218–8222. https://doi.org/10.1002/ange.201500133.

[29] Q. Bai, Y. Wang, J. Zhang, Y. Ding, Z. Peng, Z. Zhang, Hierarchically nanoporous nickel-based actuators with giant reversible strain and ultrahigh work density, J. Mater. Chem. C. 4 (2015) 45–52. https://doi.org/10.1039/c5tc03048j.

[30] P. Ponzellini, G. Giovannini, S. Cattarin, R.P. Zaccaria, S. Marras, M. Prato, A. Schirato, F. D'Amico, E. Calandrini, F. De Angelis, W. Yang, H.J. Jin, A. Alabastri, D. Garoli, Metallic Nanoporous Aluminum-Magnesium Alloy for UV-Enhanced Spectroscopy, J. Phys. Chem. C. 123 (2019) 20287–20296. https://doi.org/10.1021/acs.jpcc.9b04230.

[31] J.S. Corsi, J. Fu, Z. Wang, T. Lee, A.K. Ng, E. Detsi, Hierarchical Bulk Nanoporous Aluminum for On-Site Generation of Hydrogen by Hydrolysis in Pure Water and Combustion of Solid Fuels, ACS Sustain.

Chem. Eng. 7 (2019) 11194–11204. https://doi.org/10.1021/acssuschemeng.9b00481.

[32] H. Liu, C. Xi, J. Xin, G. Zhang, S. Zhang, Z. Zhang, Q. Huang, J. Li, H. Liu, J. Kang, Free-standing nanoporous NiMnFeMo alloy: An efficient non-precious metal electrocatalyst for water splitting, Chem. Eng. J. 404 (2021) 126530. https://doi.org/10.1016/j.cej.2020.126530.

[33] L. Sun, C.L. Chien, P.C. Searson, Fabrication of nanoporous nickel by electrochemical dealloying, Chem. Mater. 16 (2004) 3125–3129. https://doi.org/10.1021/cm0497881.

[34] M. Tsuda, T. Wada, H. Kato, Kinetics of formation and coarsening of nanoporous α-titanium dealloyed with Mg melt, J. Appl. Phys. 114 (2013). https://doi.org/10.1063/1.4821066.

[35] J. Fu, Z. Deng, T. Lee, J.S. Corsi, Z. Wang, D. Zhang, E. Detsi, PH-Controlled Dealloying Route to Hierarchical Bulk Nanoporous Zn Derived from Metastable Alloy for Hydrogen Generation by Hydrolysis of Zn in Neutral Water, ACS Appl. Energy Mater. 1 (2018) 3198–3205. https://doi.org/10.1021/acsaem.8b00419.

[36] T. Wada, H. Kato, Three-dimensional open-cell macroporous iron , chromium and ferritic stainless steel, Scr. Mater. 68 (2013) 723–726. https://doi.org/10.1016/j.scriptamat.2013.01.011.

[37] X. Guo, C. Zhang, Q. Tian, D. Yu, Liquid metals dealloying as a general approach for the selective extraction of metals and the fabrication of nanoporous metals: A review, Mater. Today Commun. 26 (2021) 102007. https://doi.org/10.1016/j.mtcomm.2020.102007.

[38] R. Zeis, T. Lei, K. Sieradzki, J. Snyder, J. Erlebacher, Catalytic reduction of oxygen and hydrogen peroxide by nanoporous gold, J. Catal. 253 (2008) 132–138. https://doi.org/10.1016/j.jcat.2007.10.017.

[39] B.C. Tappan, M.H. Huynh, M.A. Hiskey, D.E. Chavez, E.P. Luther, J.T. Mang, S.F. Son, Ultralow-Density Nanostructured Metal Foams : Combustion Synthesis , Morphology , and Composition, J. Am. Chem. Soc. 128 (2006) 6589–6594. https://doi.org/10.1021/JA056550K/SUPPL_FILE/JA056550KSI20050928_123402.AVI.

[40] T.A.R. Jr, Y. Chen, Template-based fabrication of nanoporous metals, J. Mater. Res. 33 (2017). https://doi.org/10.1557/jmr.2017.383.

[41] Z. Zhang, Y. Wang, Z. Qi, W. Zhang, J. Qin, J. Frenzel, Generalized fabrication of nanoporous metals (Au, Pd, Pt, Ag, and Cu) through chemical dealloying, J. Phys. Chem. C. 113 (2009) 12629–12636. https://doi.org/10.1021/jp811445a.

[42] P. Wahl, T. Traußnig, S. Landgraf, H.J. Jin, J. Weissmüller, R. Würschum, Adsorption-driven tuning of the electrical resistance of nanoporous gold, J. Appl. Phys. 108 (2010) 073706. https://doi.org/10.1063/1.3490789.

[43] A.K. Mishra, C. Bansal, H. Hahn, Surface charge induced variation in the electrical conductivity of nanoporous gold, J. Appl. Phys. 103 (2008) 094308. https://doi.org/10.1063/1.2912982.

[44] Z. Liu, P.C. Searson, Single nanoporous gold nanowire sensors, J. Phys. Chem. B. 110 (2006) 4318–4322. https://doi.org/10.1021/jp056940t.

[45] H. Ji, X. Wang, C. Zhao, C. Zhang, J. Xu, Z. Zhang, Formation, control and functionalization of nanoporous silver through changing dealloying media and elemental doping, CrystEngComm. 13 (2011) 2617–2628. https://doi.org/10.1039/c0ce00900h.

[46] M. Hakamada, H. Nakano, T. Furukawa, M. Takahashi, M. Mabuchi, Hydrogen Storage Properties of Nanoporous Palladium Fabricated by Dealloying, J. Phys. Chem. C. 114 (2010) 868–873. https://doi.org/10.1021/jp909479m.

[47] T. Bryce C, S. Stephen A, E.P. Luther, Nanoporous metal foams, Angew. Chemie - Int. Ed. 49 (2010) 4544–4565. https://doi.org/10.1002/anie.200902994.

[48] H.J. Jin, L. Kurmanaeva, J. Schmauch, H. Rösner, Y. Ivanisenko, J. Weissmüller, Deforming nanoporous metal: Role of lattice coherency, Acta Mater. 57 (2009) 2665–2672. https://doi.org/10.1016/j.actamat.2009.02.017.

[49] A.M. Hodge, J. Biener, J.R. Hayes, P.M. Bythrow, C.A. Volkert, A. V. Hamza, Scaling equation for yield strength of nanoporous open-cell foams, Acta Mater. 55 (2007) 1343–1349. https://doi.org/10.1016/j.actamat.2006.09.038.

[50] ASM International, Lightweight Materials: Understanding the Basics, (2012) 2012.

[51] J. Biener, A.M. Hodge, A. V. Hamza, Microscopic failure behavior of nanoporous gold, Appl. Phys. Lett. 87 (2005) 1–3. https://doi.org/10.1063/1.2051791.

[52] E. Seker, J.T. Gaskins, H. Bart-Smith, J. Zhu, M.L. Reed, G. Zangari, R. Kelly, M.R. Begley, The effects of post-fabrication annealing on the mechanical properties of freestanding nanoporous gold structures, Acta Mater. 55 (2007) 4593–4602. https://doi.org/10.1016/j.actamat.2007.03.018.

[53] Y. Sun, T.J. Balk, A multi-step dealloying method to produce nanoporous gold with no volume change and minimal cracking, Scr. Mater. 58 (2008) 727–730. https://doi.org/10.1016/j.scriptamat.2007.12.008.

[54] E. Seker, J.T. Gaskins, H. Bart-Smith, J. Zhu, M.L. Reed, G. Zangari, R. Kelly, M.R. Begley, The effects of annealing prior to dealloying on the mechanical properties of nanoporous gold microbeams, Acta Mater. 56 (2008) 324–332. https://doi.org/10.1016/j.actamat.2007.08.048.

[55] J. Weissmüller, R.C. Newman, H.J. Jin, A.M. Hodge, J.W. Kysar, Nanoporous metals by alloy corrosion: Formation and mechanical properties, MRS Bull. 34 (2009) 577–586. https://doi.org/10.1557/mrs2009.157.

[56] F. Kertis, J. Snyder, L. Govada, S. Khurshid, N. Chayen, J. Erlebacher, Structure/processing relationships in the fabrication of nanoporous gold, JOM. 62 (2010) 50–56. https://doi.org/10.1007/s11837-010-0087-6.

[57] H. Jeon, N.R. Kang, E.J. Gwak, J. il Jang, H.N. Han, J.Y. Hwang, S. Lee, J.Y. Kim, Self-similarity in the structure of coarsened nanoporous gold, Scr. Mater. 137 (2017) 46–49. https://doi.org/10.1016/j.scriptamat.2017.05.009.

[58] Y.K.C.K. Chen-Wiegart, S. Wang, Y.S. Chu, W. Liu, I. McNulty, P.W. Voorhees, D.C. Dunand, Structural evolution of nanoporous gold during thermal coarsening, Acta Mater. 60 (2012) 4972–4981. https://doi.org/10.1016/j.actamat.2012.05.012.

[59] J. Erlebacher, Mechanism of coarsening and bubble formation in high-genus nanoporous metals, Phys. Rev. Lett. 106 (2011) 1–4. https://doi.org/10.1103/PhysRevLett.106.225504.

[60] K. Kolluri, M.J. Demkowicz, Coarsening by network restructuring in model nanoporous gold, Acta Mater. 59 (2011) 7645–7653. https://doi.org/10.1016/j.actamat.2011.08.037.

[61] H. Rösner, S. Parida, D. Kramer, C.A. Volkert, J. Weissmüller, Reconstructing a nanoporous metal in three dimensions: An electron tomography study of dealloyed gold leaf, Adv. Eng. Mater. 9 (2007) 535–541. https://doi.org/10.1002/adem.200700063.

[62] L.H. Qian, M.W. Chen, Ultrafine nanoporous gold by low-temperature dealloying and kinetics of nanopore formation, Appl. Phys. Lett. 91 (2007) 083105. https://doi.org/10.1063/1.2773757.

[63] G. Pia, F. Delogu, Coarsening of nanoporous Au : Relationship between structure and mechanical properties, Acta Mater. 99 (2015) 29–38. https://doi.org/10.1016/j.actamat.2015.07.074.

[64] A. Wittstock, J. Bienera, M. Bäumerb, Surface chemistry and catalysis, RSC Nanosci. Nanotechnol. (2012) 167–198. https://doi.org/10.1039/9781849735285-00167.

[65] V. Zielasek, B. Jürgens, C. Schulz, J. Biener, M.M. Biener, A. V. Hamza, M. Bäumer, Gold Catalysts: Nanoporous Gold Foams, Angew. Chemie Int. Ed. 45 (2006) 8241–8244. https://doi.org/10.1002/ANIE.200602484.

[66] Y. Gao, Y. Ding, Nanoporous Metals for Heterogeneous Catalysis: Following the Success of Raney Nickel, Chem. - A Eur. J. 26 (2020) 8845–8856. https://doi.org/10.1002/chem.202000471.

[67] S.H. Kim, Nanoporous gold: Preparation and applications to catalysis and sensors, Curr. Appl. Phys. 18 (2018) 810–818. https://doi.org/10.1016/j.cap.2018.03.021.

[68] D. Han, T. Xu, J. Su, X. Xu, Y. Ding, Gas-Phase Selective Oxidation of Benzyl Alcohol to Benzaldehyde with Molecular Oxygen over Unsupported Nanoporous Gold, ChemCatChem. 2 (2010) 383–386. https://doi.org/10.1002/CCTC.201000001.

[69] S. Yudha S, I. Kusuma, N. Asao, Aerobic oxidation of hydroxylamines with nanoporous gold catalyst as an efficient synthetic method of nitrones, Tetrahedron. 71 (2015) 6459–6462. https://doi.org/10.1016/j.tet.2015.05.094.

[70] A. Wittstock, V. Zielasek, J. Biener, C.M. Friend, M. Bäumer, Nanoporous gold catalysts for selective gas-phase oxidative coupling of

methanol at low temperature, Science (80-.). 327 (2010) 319–322. https://doi.org/10.1126/science.1183591.

[71] A. Wittstock, B. Neumann, A. Schaefer, K. Dumbuya, C. Kübel, M.M. Biener, V. Zielasek, H.P. Steinrüek, J.M. Gottfried, J. Biener, A. Hamza, M. Bäumer, Nanoporous Au: An unsupported pure gold catalyst?, J. Phys. Chem. C. 113 (2009) 5593–5600. https://doi.org/10.1021/jp808185v.

[72] M.M. Montemore, R.J. Madix, E. Kaxiras, How Does Nanoporous Gold Dissociate Molecular Oxygen?, J. Phys. Chem. C. 120 (2016) 16636–16640. https://doi.org/10.1021/acs.jpcc.6b03371.

[73] T. Fujita, P. Guan, K. McKenna, X. Lang, A. Hirata, L. Zhang, T. Tokunaga, S. Arai, Y. Yamamoto, N. Tanaka, Y. Ishikawa, N. Asao, Y. Yamamoto, J. Erlebacher, M. Chen, Atomic origins of the high catalytic activity of nanoporous gold, Nat. Mater. 11 (2012) 775–780. https://doi.org/10.1038/nmat3391.

[74] P. Liu, P. Guan, A. Hirata, L. Zhang, L. Chen, Y. Wen, Y. Ding, T. Fujita, J. Erlebacher, M. Chen, Visualizing Under-Coordinated Surface Atoms on 3D Nanoporous Gold Catalysts, Adv. Mater. 28 (2016) 1753–1759. https://doi.org/10.1002/adma.201504032.

[75] Y. Li, S. Li, M. Bäumer, E.A. Ivanova-Shor, L. V. Moskaleva, What Changes on the Inverse Catalyst? Insights from CO Oxidation on Au-Supported Ceria Nanoparticles Using Ab Initio Molecular Dynamics, ACS Catal. 10 (2020) 3164–3174. https://doi.org/10.1021/acscatal.9b05175.

[76] Z. Wang, P. Liu, J. Han, C. Cheng, S. Ning, A. Hirata, T. Fujita, M. Chen, Engineering the internal surfaces of three-dimensional nanoporous catalysts by surfactant-modified dealloying, Nat. Commun. 8 (2017) 1–8. https://doi.org/10.1038/s41467-017-01085-3.

[77] G. Hyun, J.T. Song, C. Ahn, Y. Ham, D. Cho, J. Oh, S. Jeon, Hierarchically porous Au nanostructures with interconnected channels for efficient mass transport in electrocatalytic CO2 reduction, Proc. Natl. Acad. Sci. U. S. A. 117 (2020) 5680–5685. https://doi.org/10.1073/pnas.1918837117.

[78] Y. Ding, J. Erlebacher, Nanoporous metals with controlled multimodal pore size distribution, J. Am. Chem. Soc. 125 (2003) 7772–7773. https://doi.org/10.1021/ja035318g.

[79] T. Jin, M. Yan, Menggenbateer, T. Minato, M. Bao, Y. Yamamoto, Nanoporous Copper Metal Catalyst in Click Chemistry: Nanoporosity-

Dependent Activity without Supports and Bases, Adv. Synth. Catal. 353 (2011) 3095–3100. https://doi.org/10.1002/ADSC.201100760.

[80] S. Tanaka, T. Kaneko, N. Asao, Y. Yamamoto, M. Chen, W. Zhang, A. Inoue, A nanostructured skeleton catalyst: Suzuki-coupling with a reusable and sustainable nanoporous metallic glass Pd-catalyst, Chem. Commun. 47 (2011) 5985–5987. https://doi.org/10.1039/c1cc10710k.

[81] C. Xu, Y. Li, F. Tian, Y. Ding, Dealloying to Nanoporous Silver and Its Implementation as a Template Material for Construction of Nanotubular Mesoporous Bimetallic Nanostructures, 11 (2010) 3320–3328. https://doi.org/10.1002/cphc.201000313.

[82] Q. Chen, S. Tanaka, T. Fujita, L. Chen, T. Minato, Y. Ishikawa, M. Chen, N. Asao, Y. Yamamoto, T. Jin, The synergistic effect of nanoporous aupd alloy catalysts on highly chemoselective 1,4-hydrosilylation of conjugated cyclic enones, Chem. Commun. 50 (2014) 3344–3346. https://doi.org/10.1039/c3cc49524h.

[83] T. Fujita, H. Abe, T. Tanabe, Y. Ito, T. Tokunaga, S. Arai, Y. Yamamoto, A. Hirata, M. Chen, Earth-Abundant and Durable Nanoporous Catalyst for Exhaust-Gas Conversion, Adv. Funct. Mater. 26 (2016) 1609–1616. https://doi.org/10.1002/adfm.201504811.

[84] T. Fujita, H. Abe, T. Tanabe, Y. Ito, T. Tokunaga, S. Arai, Y. Yamamoto, A. Hirata, M. Chen, T. Fujita, Y. Ito, A. Hirata, M.W. Chen, H. Abe, T. Tanabe, T. Tokunaga, S. Arai, Y. Yamamoto, Earth-Abundant and Durable Nanoporous Catalyst for Exhaust-Gas Conversion, Adv. Funct. Mater. 26 (2016) 1609–1616. https://doi.org/10.1002/ADFM.201504811.

[85] W. Luc, F. Jiao, Nanoporous Metals as Electrocatalysts: State-of-the-Art, Opportunities, and Challenges, ACS Catal. 7 (2017) 5856–5861. https://doi.org/10.1021/acscatal.7b01803.

[86] C. Sealy, The problem with platinum, Mater. Today. 11 (2008) 65–68. https://doi.org/10.1016/S1369-7021(08)70254-2.

[87] J. Zhang, P. Liu, H. Ma, Y. Ding, Nanostructured Porous Gold for Methanol Electro-Oxidation, J. Phys. Chem. C. 111 (2007) 10382–10388. https://doi.org/10.1021/JP072333P.

[88] X. Ge, R. Wang, P. Liu, Y. Ding, Platinum-decorated nanoporous gold leaf for methanol electrooxidation, Chem. Mater. 19 (2007) 5827–5829. https://doi.org/10.1021/cm702335f.

[89] R. Wang, C. Wang, W. Bin Cai, Y. Ding, Ultralow-platinum-loading high-performance nanoporous electrocatalysts with nanoengineered surface structures, Adv. Mater. 22 (2010) 1845–1848. https://doi.org/10.1002/adma.200903548.

[90] M. Shao, K. Shoemaker, A. Peles, K. Kaneko, L. Protsailo, Pt monolayer on porous Pd-Cu alloys as oxygen reduction electrocatalysts, J. Am. Chem. Soc. 132 (2010) 9253–9255. https://doi.org/10.1021/ja101966a.

[91] L. Liu, R. Scholz, E. Pippel, U. Gösele, Microstructure, electrocatalytic and sensing properties of nanoporous Pt46Ni54 alloy nanowires fabricated by mild dealloying, J. Mater. Chem. 20 (2010) 5621–5627. https://doi.org/10.1039/c0jm00113a.

[92] S. Chatterjee, C. Griego, J.L. Hart, Y. Li, M.L. Taheri, J. Keith, J.D. Snyder, Free Standing Nanoporous Palladium Alloys as CO Poisoning Tolerant Electrocatalysts for the Electrochemical Reduction of CO2 to Formate, ACS Catal. 9 (2019) 5290–5301. https://doi.org/10.1021/acscatal.9b00330.

[93] T. Fujita, H. Abe, T. Tanabe, Y. Ito, T. Tokunaga, S. Arai, Y. Yamamoto, A. Hirata, M. Chen, Earth-Abundant and Durable Nanoporous Catalyst for Exhaust-Gas Conversion, Adv. Funct. Mater. 26 (2016) 1609–1616. https://doi.org/10.1002/adfm.201504811.

[94] S. Ge, X. Jiao, D. Chen, Ultrasensitive electrochemical immunosensor for CA 15-3 using thionine-nanoporous gold-graphene as a platform and horseradish peroxidase-encapsulated liposomes as signal amplification, Analyst. 137 (2012) 4440–4447. https://doi.org/10.1039/c2an35751h.

[95] Z. Liu, J. Du, C. Qiu, L. Huang, H. Ma, D. Shen, Y. Ding, Electrochemical sensor for detection of p-nitrophenol based on nanoporous gold, Electrochem. Commun. 11 (2009) 1365–1368. https://doi.org/10.1016/j.elecom.2009.05.004.

[96] L.Y. Chen, T. Fujita, Y. Ding, M.W. Chen, A Three-Dimensional Gold-Decorated Nanoporous Copper Core–Shell Composite for Electrocatalysis and Nonenzymatic Biosensing, Adv. Funct. Mater. 20 (2010) 2279–2285. https://doi.org/10.1002/ADFM.201000326.

[97] T. Chen, Z. Liu, W. Lu, X. Zhou, H. Ma, Fabrication of free-standing nanoporous silver by selectively dissolving gold from gold–silver alloys via a novel converse dealloying method, Electrochem. Commun. 13 (2011) 1086–1089. https://doi.org/10.1016/J.ELECOM.2011.07.001.

[98] A. Liu, H. Geng, C. Xu, H. Qiu, A three-dimensional hierarchical nanoporous PdCu alloy for enhanced electrocatalysis and biosensing, Anal. Chim. Acta. 703 (2011) 172–178. https://doi.org/10.1016/J.ACA.2011.07.039.

[99] C. Xu, Y. Liu, F. Su, A. Liu, H. Qiu, Nanoporous PtAg and PtCu alloys with hollow ligaments for enhanced electrocatalysis and glucose biosensing, Biosens. Bioelectron. 27 (2011) 160–166. https://doi.org/10.1016/J.BIOS.2011.06.036.

[100] H. Qiu, L. Xue, G. Ji, G. Zhou, X. Huang, Y. Qu, P. Gao, Enzyme-modified nanoporous gold-based electrochemical biosensors, Biosens. Bioelectron. 24 (2009) 3014–3018. https://doi.org/10.1016/j.bios.2009.03.011.

[101] L.Y. Chen, T. Fujita, M.W. Chen, Biofunctionalized nanoporous gold for electrochemical biosensors, Electrochim. Acta. 67 (2012) 1–5. https://doi.org/10.1016/j.electacta.2011.12.132.

[102] H. Qiu, L. Lu, X. Huang, Z. Zhang, Y. Qu, Immobilization of horseradish peroxidase on nanoporous copper and its potential applications, Bioresour. Technol. 101 (2010) 9415–9420. https://doi.org/10.1016/j.biortech.2010.07.097.

[103] C. Wu, X. Liu, Y. Li, X. Du, X. Wang, P. Xu, Lipase-nanoporous gold biocomposite modified electrode for reliable detection of triglycerides, Biosens. Bioelectron. 53 (2014) 26–30. https://doi.org/10.1016/j.bios.2013.09.040.

[104] R. Feng, Y. Zhang, H. Yu, D. Wu, H. Ma, B. Zhu, C. Xu, H. Li, B. Du, Q. Wei, Nanoporous PtCo-based ultrasensitive enzyme-free immunosensor for zeranol detection, Biosens. Bioelectron. 42 (2013) 367–372. https://doi.org/10.1016/j.bios.2012.10.031.

[105] Q. Wei, Y. Zhao, C. Xu, D. Wu, Y. Cai, J. He, H. Li, B. Du, M. Yang, Nanoporous gold film based immunosensor for label-free detection of cancer biomarker, Biosens. Bioelectron. 26 (2011) 3714–3718. https://doi.org/10.1016/j.bios.2011.02.024.

[106] D. Wu, R. Li, H. Wang, S. Liu, H. Wang, Q. Wei, B. Du, Hollow mesoporous silica microspheres as sensitive labels for immunoassay of prostate-specific antigen, Analyst. 137 (2012) 608–613. https://doi.org/10.1039/c2an16033a.

[107] O. V. Shulga, D. Zhou, A. V. Demchenko, K.J. Stine, Detection of free prostate specific antigen (fPSA) on a nanoporous gold platform, Analyst. 133 (2008) 319–322. https://doi.org/10.1039/B712760J.

[108] L.H. Qian, X.Q. Yan, T. Fujita, A. Inoue, M.W. Chen, Surface enhanced Raman scattering of nanoporous gold: Smaller pore sizes stronger enhancements, Appl. Phys. Lett. 90 (2007) 153120. https://doi.org/10.1063/1.2722199.

[109] E. Detsi, M. Salverda, P.R. Onck, J.T.M. De Hosson, On the localized surface plasmon resonance modes in nanoporous gold films, J. Appl. Phys. 115 (2014). https://doi.org/10.1063/1.4862440.

[110] D. Garoli, A. Schirato, G. Giovannini, S. Cattarin, P. Ponzellini, E. Calandrini, R.P. Zaccaria, F. D'amico, M. Pachetti, W. Yang, H.J. Jin, R. Krahne, A. Alabastri, Galvanic replacement reaction as a route to prepare nanoporous aluminum for UV plasmonics, Nanomaterials. 10 (2020) 1–12. https://doi.org/10.3390/nano10010102.

[111] L. Zhang, X. Lang, A. Hirata, M. Chen, Wrinkled nanoporous gold films with ultrahigh surface-enhanced raman scattering enhancement, ACS Nano. 5 (2011) 4407–4413. https://doi.org/10.1021/nn201443p.

[112] J. Qi, J. Zeng, F. Zhao, S.H. Lin, B. Raja, U. Strych, R.C. Willson, W.C. Shih, Label-free, in situ SERS monitoring of individual DNA hybridization in microfluidics, Nanoscale. 6 (2014) 8521–8526. https://doi.org/10.1039/c4nr01951b.

[113] M.J. Lee, W.G. Yang, J.H. Kim, K. Hwang, W.S. Chae, Silver-coated nanoporous gold skeletons for fluorescence amplification, Microporous Mesoporous Mater. 237 (2017) 60–64. https://doi.org/10.1016/j.micromeso.2016.09.016.

[114] C. Chen, L. Zhang, M. Yang, C. Tao, Z. Han, B. Chen, H. Zeng, Size and distance dependent fluorescence enhancement of nanoporous gold, Opt. Express. 25 (2017) 9901. https://doi.org/10.1364/oe.25.009901.

[115] S.R. Ahmed, M.A. Hossain, J.Y. Park, S.H. Kim, D. Lee, T. Suzuki, J. Lee, E.Y. Park, Metal enhanced fluorescence on nanoporous gold leaf-based assay platform for virus detection, Biosens. Bioelectron. 58 (2014) 33–39. https://doi.org/10.1016/j.bios.2014.02.039.

[116] A.N. Koya, X. Zhu, N. Ohannesian, A.A. Yanik, A. Alabastri, R. Proietti Zaccaria, R. Krahne, W.C. Shih, D. Garoli, Nanoporous Metals: From Plasmonic Properties to Applications in Enhanced Spectroscopy and

Photocatalysis, ACS Nano. 15 (2021) 6038–6060. https://doi.org/10.1021/acsnano.0c10945.

[117] W.C. Shih, G.M. Santos, F. Zhao, O. Zenasni, M.M.P. Arnob, Simultaneous chemical and refractive index sensing in the 1-2.5 μm near-infrared wavelength range on nanoporous gold disks, Nano Lett. 16 (2016) 4641–4647. https://doi.org/10.1021/acs.nanolett.6b01959.

[118] D. Steinebrunner, G. Schnurpfeil, D. Wöhrle, A. Wittstock, Photocatalytic coatings based on a zinc(ii) phthalocyanine derivative immobilized on nanoporous gold leafs with various pore sizes, RSC Adv. 10 (2019) 53–59. https://doi.org/10.1039/c9ra08841e.

[119] R. Ron, D. Gachet, K. Rechav, A. Salomon, Direct Fabrication of 3D Metallic Networks and Their Performance, Adv. Mater. 29 (2017) 1604018. https://doi.org/10.1002/adma.201604018.

[120] Z. Zhang, C. Zhang, H. Zheng, H. Xu, Plasmon-Driven Catalysis on Molecules and Nanomaterials, Acc. Chem. Res. 52 (2019) 2506–2515. https://doi.org/10.1021/acs.accounts.9b00224.

[121] G. Ruffato, D. Garoli, S. Cattarin, S. Barison, F. Romanato, FIB lithography of nanoporous gold slits for extraordinary transmission, in: Microelectron. Eng., Elsevier, 2012: pp. 419–423. https://doi.org/10.1016/j.mee.2012.07.091.

[122] G.M. Santos, F. Zhao, J. Zeng, W.C. Shih, Characterization of nanoporous gold disks for photothermal light harvesting and light-gated molecular release, Nanoscale. 6 (2014) 5718–5724. https://doi.org/10.1039/c4nr01266f.

[123] G.M. Santos, F.I. de S. Ferrara, F. Zhao, D.F. Rodrigues, W.-C. Shih, Photothermal inactivation of heat-resistant bacteria on nanoporous gold disk arrays, Opt. Mater. Express. 6 (2016) 1217. https://doi.org/10.1364/ome.6.001217.

[124] J. Song, X. Yang, Z. Yang, L. Lin, Y. Liu, Z. Zhou, Z. Shen, G. Yu, Y. Dai, O. Jacobson, J. Munasinghe, B. Yung, G.J. Teng, X. Chen, Rational Design of Branched Nanoporous Gold Nanoshells with Enhanced Physico-Optical Properties for Optical Imaging and Cancer Therapy, ACS Nano. 11 (2017) 6102–6113. https://doi.org/10.1021/ACSNANO.7B02048/SUPPL_FILE/NN7B02048_SI_001.PDF.

[125] D. Kramer, R.N. Viswanath, J. Weissmüller, Surface-stress induced macroscopic bending of nanoporous gold cantilevers, Nano Lett. 4 (2004) 793–796. https://doi.org/10.1021/NL049927D/SUPPL_FILE/NL049927DSI20040223_023436.PDF.

[126] E. Detsi, S.H. Tolbert, S. Punzhin, J.T.M. De Hosson, Metallic muscles and beyond: nanofoams at work, J. Mater. Sci. 51 (2015) 615–634. https://doi.org/10.1007/s10853-015-9317-1.

[127] R.N. Viswanath, D. Kramer, J. Weissmüller, Adsorbate effects on the surface stress-charge response of platinum electrodes, Electrochim. Acta. 53 (2008) 2757–2767. https://doi.org/10.1016/j.electacta.2007.10.049.

[128] T. Fujita, H. Abe, T. Tanabe, Y. Ito, T. Tokunaga, S. Arai, Y. Yamamoto, A. Hirata, M. Chen, Earth-Abundant and Durable Nanoporous Catalyst for Exhaust-Gas Conversion, Adv. Funct. Mater. 26 (2016) 1609–1616. https://doi.org/10.1002/adfm.201504811.

[129] R.N. Viswanath, J. Weissmüller, Electrocapillary coupling coefficients for hydrogen electrosorption on palladium, Acta Mater. 61 (2013) 6301–6309. https://doi.org/10.1016/j.actamat.2013.07.013.

[130] H.J. Jin, J. Weissmüller, Bulk nanoporous metal for actuation, Adv. Eng. Mater. 12 (2010) 714–723. https://doi.org/10.1002/adem.200900329.

[131] E. Detsi, P. Onck, J.T.M. De Hosson, Metallic muscles at work: High rate actuation in nanoporous gold/polyaniline composites, ACS Nano. 7 (2013) 4299–4306. https://doi.org/10.1021/nn400803x.

[132] J. Biener, A. Wittstock, L.A. Zepeda-Ruiz, M.M. Biener, V. Zielasek, D. Kramer, R.N. Viswanath, J. Weissmüller, M. Bäumer, A. V. Hamza, Surface-chemistry-driven actuation in nanoporous gold, Nat. Mater. 2009 81. 8 (2008) 47–51. https://doi.org/10.1038/nmat2335.

[133] Z. Yang, X. Han, H.K. Lee, G.C. Phan-Quang, C.S.L. Koh, C.L. Lay, Y.H. Lee, Y.E. Miao, T. Liu, I.Y. Phang, X.Y. Ling, Shape-dependent thermo-plasmonic effect of nanoporous gold at the nanoscale for ultrasensitive heat-mediated remote actuation, Nanoscale. 10 (2018) 16005–16012. https://doi.org/10.1039/c8nr04053b.

[134] K.U. Lee, J.Y. Byun, H.J. Shin, S.H. Kim, A high-performance supercapacitor based on polyaniline-nanoporous gold, J. Alloys Compd. 779 (2019) 74–80. https://doi.org/10.1016/j.jallcom.2018.11.022.

[135] X.Y. Lang, H.T. Yuan, Y. Iwasa, M.W. Chen, Three-dimensional nanoporous gold for electrochemical supercapacitors, Scr. Mater. 64 (2011) 923–926. https://doi.org/10.1016/j.scriptamat.2011.01.038.

[136] N. Kobayashi, H. Ogata, K.C. Park, K. Takeuchi, M. Endo, Investigation on capacitive behaviors of porous Ni electrodes for electric double layer capacitors, Electrochim. Acta. 90 (2013) 408–415. https://doi.org/10.1016/j.electacta.2012.12.002.

[137] N. Kobayashi, T. Sakumoto, S. Mori, H. Ogata, K.C. Park, K. Takeuchi, M. Endo, Investigation on capacitive behaviors of porous Ni electrodes in ionic liquids, Electrochim. Acta. 105 (2013) 455–461. https://doi.org/10.1016/J.ELECTACTA.2013.05.017.

[138] J. Kang, A. Hirata, H.J. Qiu, L. Chen, X. Ge, T. Fujita, M. Chen, Self-grown oxy-hydroxide@nanoporous metal electrode for high-performance supercapacitors, Adv. Mater. 26 (2014) 269–272. https://doi.org/10.1002/adma.201302975.

[139] P.C. Chen, S.J. Hsieh, J. Zou, C.C. Chen, Selectively dealloyed Ti/TiO2 network nanostructures for supercapacitor application, Mater. Lett. 133 (2014) 175–178. https://doi.org/10.1016/j.matlet.2014.06.165.

[140] J. Kang, L. Chen, Y. Hou, C. Li, T. Fujita, X. Lang, A. Hirata, M. Chen, Electroplated Thick Manganese Oxide Films with Ultrahigh Capacitance, Adv. Energy Mater. 3 (2013) 857–863. https://doi.org/10.1002/aenm.201201046.

[141] Q. Lu, J.G. Chen, J.Q. Xiao, Nanostructured electrodes for high-performance pseudocapacitors, Angew. Chemie - Int. Ed. 52 (2013) 1882–1889. https://doi.org/10.1002/anie.201203201.

[142] F. Meng, Y. Ding, Sub-micrometer-thick all-solid-state supercapacitors with high power and energy densities, Adv. Mater. 23 (2011) 4098–4102. https://doi.org/10.1002/adma.201101678.

[143] J. Zhang, Z. Wang, Y. Hong, S. Li, X. Jin, G.Z. Chen, Electrochemical fabrication of porous Sn/SnSb negative electrodes from mixed SnO2-Sb2O3, Electrochem. Commun. 38 (2014) 36–39. https://doi.org/10.1016/j.elecom.2013.10.030.

[144] Y. Yu, L. Gu, X. Lang, C. Zhu, T. Fujita, M. Chen, J. Maier, Li storage in 3D nanoporous au-supported nanocrystalline tin, Adv. Mater. 23 (2011) 2443–2447. https://doi.org/10.1002/adma.201004331.

[145] C. Hou, X.M. Shi, C.X. Zhao, X.Y. Lang, L.L. Zhao, Z. Wen, Y.F. Zhu, M. Zhao, J.C. Li, Q. Jiang, SnO2 nanoparticles embedded in 3D nanoporous/solid copper current collectors for high-performance reversible lithium storage, J. Mater. Chem. A. 2 (2014) 15519–15526. https://doi.org/10.1039/c4ta02604g.

[146] S. Ni, X. Yang, T. Li, Fabrication of porous Ni3S2/Ni nanostructured electrode and its application in lithium ion battery, Mater. Chem. Phys. 132 (2012) 1103–1107. https://doi.org/10.1016/j.matchemphys.2011.12.077.

[147] X. Wang, D. Liu, Q. Weng, J. Liu, Q. Liang, C. Zhang, Cu/Li4Ti5O12 scaffolds as superior anodes for lithium-ion batteries, NPG Asia Mater. 7 (2015) e171–e171. https://doi.org/10.1038/am.2015.23.

[148] Y. Xue, F. Scaglione, F. Celegato, P. Denis, H.J. Fecht, P. Rizzi, L. Battezzati, Shape controlled gold nanostructures on de-alloyed nanoporous gold with excellent SERS performance, Chem. Phys. Lett. 709 (2018) 46–51.

[149] A. Wichmann, A. Wittstock, K. Frank, M.M. Biener, B. Neumann, L. Mädler, J. Biener, A. Rosenauer, M. Bäumer, Maximizing activity and stability by turning gold catalysis upside down: Oxide particles on nanoporous gold, ChemCatChem. 5 (2013) 2037–2043. https://doi.org/10.1002/cctc.201200759.

[150] J. Shi, A. Schaefer, A. Wichmann, M.M. Murshed, T.M. Gesing, A. Wittstock, M. Bäumer, Nanoporous gold-supported ceria for the water-gas shift reaction: UHV inspired design for applied catalysis, J. Phys. Chem. C. 118 (2014) 29270–29277. https://doi.org/10.1021/jp505433a.

[151] J. Van Der Zalm, S. Chen, W. Huang, A. Chen, Review — Recent Advances in the Development of Nanoporous Au for Sensing Applications Review — Recent Advances in the Development of Nanoporous Au for Sensing Applications, (2020). https://doi.org/10.1149/1945-7111/ab64c0.

[152] K. Wang, A. Kobler, C. Kübel, H. Jelitto, G. Schneider, J. Weissmüller, Nanoporous-gold-based composites: Toward tensile ductility, NPG Asia Mater. 7 (2015) 1–11. https://doi.org/10.1038/am.2015.58.

Chapter 2

NP Au and NP Cu from mechanically alloyed precursors

2.1 Introduction

Up to now, NP noble metals have been produced in different ways through the manipulation of important factors: precursor alloy, sample form, and dealloying parameters such as temperature, solution/electrolyte type and concentration, external electrical potential, and treatment time. Among them, the different precursor alloys gave rise to NP metals with different sets of integral features, such as density and characteristic lengths, which are partially disentangled [1–4]. This is quite important because specific combinations of NP metal features can be more or less favorable for diverse applications: mechanical properties are enhanced when small characteristic lengths are coupled with a high relative density, while small characteristic lengths and a low density are ideal for enabling high catalytic activity and enhanced mass transport in catalytic/electrocatalytic applications [5]. The choice of the alloy is generally limited by the availability of suitable phases, either crystalline or amorphous, and by the parting limit of each phase [6]. It is therefore interesting to explore new possible precursors to extend or enhance the suitable arrays of properties that an NP metal can display.

In this chapter the fabrication and morphological characterization of NP Au from a precursor with Ag content beyond parting limit and NP Cu from a new precursor alloy will be presented; those of NP Au from the common $Au_{30}Ag_{70}$ precursor and of NP Al will be reported in the following chapters instead, together with the studies carried on them.

In this thesis, the precursor alloys used to fabricate NP metals were produced by mechanical alloying (MA). MA is a powder processing technique used for producing homogenous stable and metastable alloys starting from elemental or prealloyed powder mixtures. It is an easy, scalable, and relatively inexpensive technique that enables the production of alloys without reaching melting temperatures [7]. Similar to rapid solidification processing, vapor deposition, and laser processing, it enables the production of metastable phases, such as supersaturated solid solutions, nanocrystalline and amorphous phases, fine dispersion of second phases in the main phase, disordering of ordered intermetallics [7–11]. The process involves the repeated cold welding, fracturing, and rewelding of powders in high energy ball mills. In some cases, especially when ductile materials are used, particle size reduction can be hampered by excessive

cold welding, which can also cause the complete agglomeration of particles among themselves or on the milling mediums. This can be avoided by adding a 1-2 wt % of a process control agent (PCA), in general an organic compound, which adsorbs on the particle surface and reduces cold welding, allowing the size reduction up to the nanometer level. The milled powders can then be compacted into the desired shape and heat-treated to modulate the microstructure and properties of the material.

Dealloying from AuAg precursor can efficiently be performed in a short range of compositions, namely around 25-35 at. % of Au. When Au content is too low, the NP structure can be formed but the macroscopic sample can be destroyed in particles due to severe cracking resulting from dealloying [12]. When Au content is too high (over 40 at. %), it slows down the dealloying until blocking the dealloying to the first atomic layers. This is due to a percolation threshold related to the geometry of the FCC crystalline structure. Kinetic Monte Carlo simulations showed that the experimentally noticed parting limit was in agreement with a theoretical percolation threshold model in which only Ag atoms with less than 10 coordinated atoms can be dissolved [13]. The simulations showed that the phenomenon was mainly governed by the geometry of the lattice and not by kinetic parameters, such as surface diffusion. However, in this work we found that nanoporous layers of µm order can arise from $Au_{50}Ag_{50}$ precursor dealloying for prolonged times. This can be ascribed to the surface diffusion of Au atoms that can eventually expose other Ag atoms to dissolution and enable dealloying to slowly proceed.

As said in **Chapter 1**, NP metals can exhibit new or enhanced properties when combined with other materials. Since its discovery, graphene has attracted huge interest for its excellent properties. Moreover, it was noted that its properties can be enhanced when combined with metal nanoparticles: Au nanoparticles/graphene nanocomposites have shown high potential for fuel cells applications [14,15], optical [16], and electrochemical [17,18] sensing, photocatalysis [19] and catalysis [20]. Up to now, Au nanostructures have been usually grown or deposited on graphene. It would be interesting to fabricate the “inverse” material, in which graphene can be dispersed on a monolithic NP Au. However, NP Au/graphene composites have not been fabricated yet, probably due to the challenges related to the possible methods of fabrication. As an example, porous Ni was used as scaffold for graphene deposition in order to form porous metal/graphene composite: porous Ni was used as scaffold for chemical vapor deposition of graphene at 750°C. However, the characteristic lengths of the as-produced material were above 500 nm and considering the typical ligament sizes arising for NP Au at these

temperatures, they would be even higher for this material [21]. We attempted the fabrication of NP Au/graphene composite (hereinafter NP Au@G) by producing firstly a nanocomposite of graphene dispersed in Au30Ag70 alloy through mechanical milling of the elemental powders with graphene. After dealloying, the nanoporous morphology and graphene structure were studied employing SEM and Raman spectroscopy, respectively.

NP Cu is among the most studied and promising NP metals. Compared with the other noble metals, Cu presents an economical enormous advantage, complemented by excellent electrical and thermal conductivities and low reactivity. At the same time, it is more reactive than the major group of noble metals and the presence of copper oxide at the surface can have a serious impact on catalysis, electrocatalysis, and photocatalysis [22,23]. Moreover, Cu nanostructures exhibit interesting plasmonic activity [24,25]. Thus, NP Cu has been widely studied as an alternative to NP noble metals and has shown interesting value for several applications: SERS [25,26], fuel cells [27,28], electrode material for Li-ion batteries [29–32], and supercapacitors [33], electrochemical sensing [27,34,35], catalysis in click chemistry [36].

NP Cu can be fabricated by chemical/electrochemical dealloying of various binary precursor alloys with less noble elements, such as Mn [23,37], Al [27], and Zn, from multimetallic [38,39] and amorphous alloys [2,3,33,40]. Cu-Zn alloys are particularly interesting and have been extensively exploited as NP Cu precursors thanks to their low-cost, non-toxicity, and easy preparation by electrodeposition [22,35,49–53,41–48]. However, the production of fine bicontinuous porous structures of NP Cu from this alloy has not been obtained, yet. This is probably due to the difficult achievement of a precursor with a single-phase solid solution with the same crystal structure of Cu, which is the ideal condition for the production of an NP metal with a bicontinuous structure of nano-sized ligaments and pores from a crystalline precursor. To the best of our knowledge, Cheng et al. [22] and Egle et al. [42] produced the examples of bicontinuous NP Cu with the smallest characteristic lengths found in literature, of around 60 nm and 46 nm, respectively. Both the groups prepared the material from a Goodfellow $Cu_{20}Zn_{80}$ commercial precursor alloy. Egle et al. reported that the precursor was made of a hexagonal single-phase ε-$CuZn_4$. Besides, even if carrying a different crystal structure compared to Cu, this is probably the best condition for obtaining a homogeneous NP Cu with high porosity. Indeed, even at higher Cu contents, there are no phase-diagram regions in which an FCC single-phase is favorable until Cu contents higher than 80 at. %, when Zn atoms can completely be dissolved in the Cu lattice [54]. Typically, in-lab-produced CuZn precursors are made by melting [52] and in thin films

by electrodeposition [35]. However, we did not find any reports in which NP Cu was fabricated by dealloying of mechanically alloyed precursors. To explore the effect of this preparation method, we fabricated NP Cu from a mechanically alloyed $Cu_{20}Zn_{80}$ precursor. From XRD measurements we found that the alloyed powder possesses a dominant ε-$CuZn_4$ phase. Thus, we attempted the dealloying through either chemical either vapor phase dealloying, exploiting the high differences in chemical reactivity and vapor pressure between the two metals.

2.2 Materials and methods

2.2.1 Materials

Au powder (99.995 %, Alfa Aesar), Ag powder (99.9%, Aldrich), Cu powder (99.9 %, Alfa Aesar), Zn powder (99.9 %, Alfa Aesar), Nitric acid (HNO_3 70 %, BDH), Hydrochloric acid (HCl 37 %, Honeywell), graphene powder (Inter Est Group). Ultrapure water (18.2 MΩ·cm) was produced with a Milli-Q Millipore water purification system.

2.2.2 NP Au fabrication

Au50Ag50 alloy fabrication

2 g of AuAg powder mixture was prepared in an atomic ratio of 50:50. The powders were mechanically milled in a SPEX *8000M Mixer/Mill* ball mill for 16h in a hardened steel vial with two hardened steel balls of 8g each. The powders were removed from the sides of the vial every 30 minutes in the first 2 hours and then every 5 h, in order to homogenize the mixture. Pellets of 1.3 cm of diameter and around 0.3 mm of thickness were prepared by cold pressing under 10 tons for 5 min with a hydraulic press.

Dealloying of AuAg alloy

$Au_{50}Ag_{50}$ pellets were immersed in concentrated HNO_3 (70%) for 15 min, 1 h, 6 h, and 96 h. During the treatment, the acidic solution was repeatedly stirred and was substituted with a fresh one every 24 h. After the treatment, the pellets were rinsed three times and stored in ultrapure water for 24 h. Then, the samples were dried in a desiccator and stored under Ar atmosphere.

NP Au/graphene fabrication

10 at. % of graphene was dispersed in $Au_{30}Ag_{70}$ powder mixture. 2 g of the mixture were subjected to mechanical milling, cold pressing, and dealloying with the same procedure used for $Au_{50}Ag_{50}$ alloy fabrication.

2.2.3 NP Cu fabrication

CuZn alloy fabrication

8 g of Cu and Zn powders were mixed in a 1:4 atomic ratio and placed in a hardened steel vial with two hardened steel balls of 8 g each under Ar atmosphere with O_2 impurities below 2 ppm. The powders were mechanically alloyed in a SPEX *8000M Mixer/Mill* ball mill. The powders were removed from the sides of the vial every 30 min in the first 2 h and then every 5 h, in order to homogenize the mixture. Pellets of 1.3 cm of diameter and around 0.3 mm of thickness were prepared by cold pressing under 10 tons for 5 min with a hydraulic press.

NP Cu fabrication

NP Cu fabrication was attempted both by chemical dealloying both by vapor phase dealloying. Chemical dealloying was performed by immersion of CuZn pellets in different HCl solutions (1M and 0.1M) for different times. After the treatment, the pellets were washed and rinsed with ultrapure water at least five times, dried in vacuum and stored in Ar filled glovebox. Vapor phase dealloying was carried out by placing CuZn pellets in a glass tube connected to a turbomolecular vacuum pump. The samples were kept for 1 h under high-vacuum conditions with pressure around 10^{-2} Pa. Then, the temperature was raised at 25 °C min^{-1} up to the target temperature. The samples were annealed at 500 °C and 600 °C for 1 h and then cooled gradually under high-vacuum conditions.

2.2.4 SEM imaging

The precursor and dealloyed materials were investigated by SEM using a Zeiss Merlin microscope, equipped with a Schottky electron source, working with an acceleration voltage of 5 kV at short working distance (high-resolution mode). Secondary electrons (SE) were collected to provide fine details on the surface morphology. SE were gathered using an in-lens detector. SEM-Energy Dispersive Spectroscopy (EDS) measurements were performed by an Oxford silicon drift detector (SDD) with a detection area of 60 mm^2 at an acceleration voltage of 15 kV. Image analysis (IA) was performed with Fiji software [55].

2.2.5 XRD measurements

The structural and microstructural evolution of processed powders was investigated by X-Ray Diffraction (XRD). XRD measurements were carried out with a Rigaku Miniflex II Diffractometer equipped with a 600W X-ray

source using Cu $K\alpha_1$ with an incident beam angle 2θ ranging from 30 to 120 degrees. Quantitative phase and microstructural analyses were performed using the Rietveld method [56].

2.2.6 TEM imaging

Transmission Electron Microscopy (TEM) imaging on graphene powders was carried out with a JEOL-JEM 1400 Plus microscope operating at an acceleration voltage of 120 kV.

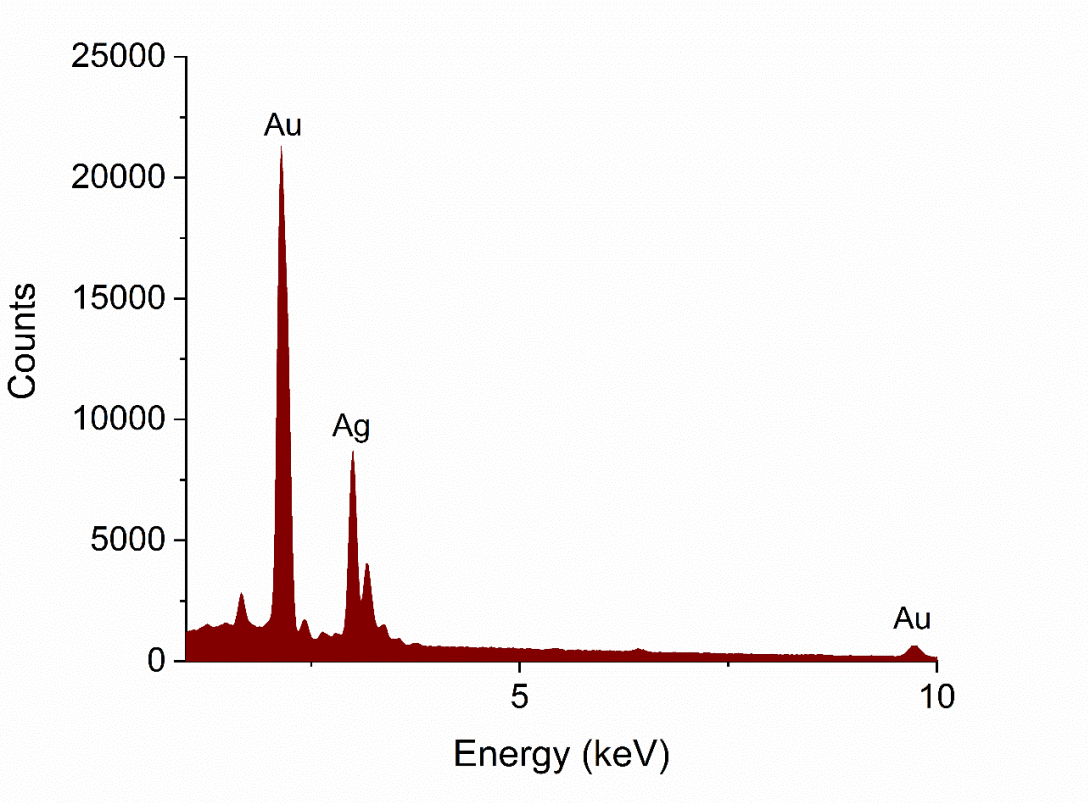

Fig. 2.1 EDS spectrum of $Au_{50}Ag_{50}$ pellet after mechanical alloying and cold pressing.

2.3 Results and discussion

EDS was carried out on the surface of the precursor $Au_{50}Ag_{50}$ alloys in order to study the alloy composition. An EDS spectrum is shown in Fig. 2.1. The results of the analysis confirm the equimolar composition of the two elements. Typically, in the case of dealloying from suitable AuAg alloys, the color of the sample changes from the silvery of the precursor to a darker one that can space from red to brown. In this case, immersed the pellet in HNO3 solution, the color had not changed to the naked eye for the first hours. SEM observations confirmed that the specimen surface wasn't porous after 6 h. However, by prolonging dealloying over 96 h a reddish reflection could be observed from the sample surface, typical color of NP Au.

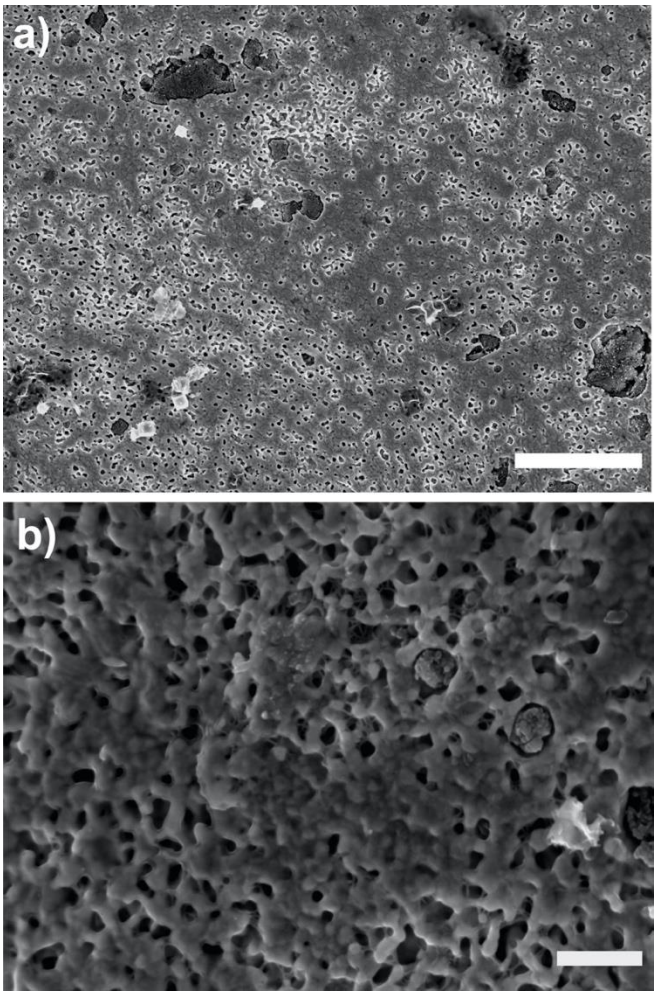

Fig. 2.2 Low magnification (a, scale bar: 2 µm) and high magnification (b, scale bar: 300 nm) SEM images of $Au_{50}Ag_{50}$ surface after 96 h of dealloying.

SEM observations shown in Fig. 2.2 further confirmed the presence of a nanoporous structure on the surface. In order to evaluate the depth of the nanoporous layer, we performed SEM imaging of the cross-section of the sample. Fig. 2.3 shows a low-magnification image of the cross-section area near the surface of the sample. It can be seen that the sample is not porous apart from a region near the surface, with thick between 1 and 2 μm, which appears darker due to the lower electrical conductivity of the porous structure that causes a minor charging of the surface. The inset of the figure shows at higher magnifications the porous area of the sample. To the best of our knowledge, this is the first case in which a nanoporous layer was formed from an AuAg alloy beyond the common parting limit of 45% of Au atomic content. However, investigating the corrosion of several AuAg alloys, Artymowicz et al. suggested the formation of thin (few tens of nanometers) NP layers, to explain the slight stress corrosion cracking observed by Maier et al. for alloys with Au content up to 50 at. %, subjected to immersion in 1M $HClO_4$ [13].

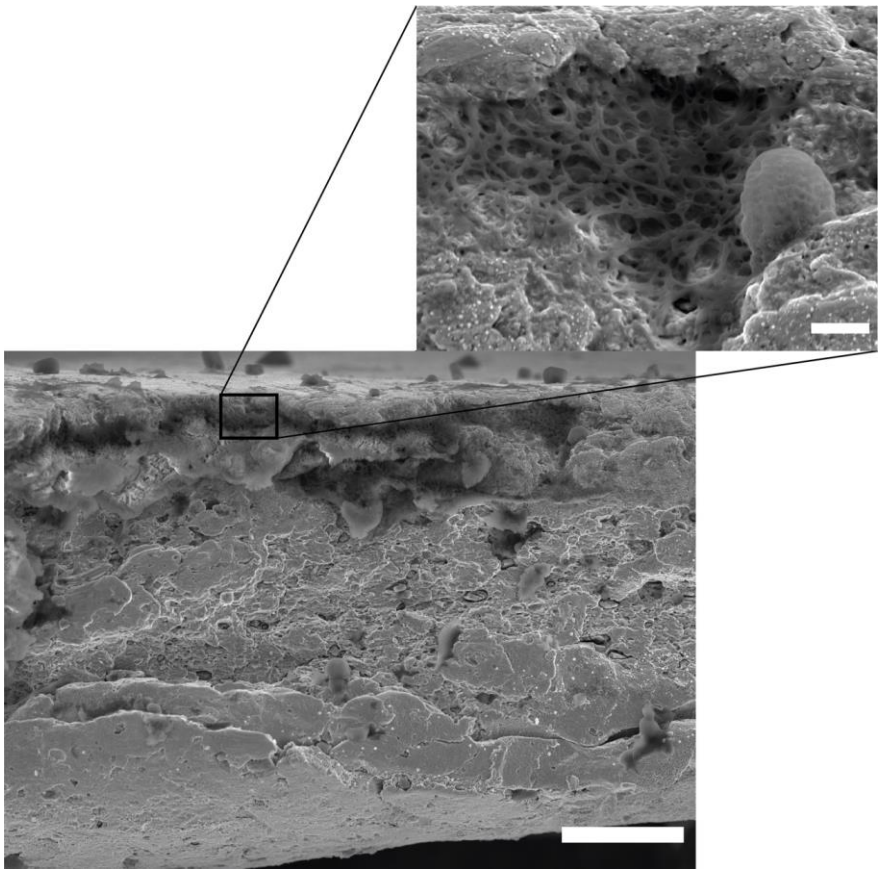

Fig. 2.3 SEM image of cross-section area near surface of $Au_{50}Ag_{50}$ treated for 96h; scale bar: 5 μm. An higher magnification image of the porous area is shown in the inset; scale bar: 500 nm.

2.3.1 NP Au/Graphene composite

Graphene quality before and after mechanical milling with Au and Ag powders was investigated through Raman spectroscopy: the two different spectra are shown in Fig. 2.4. The graphene spectrum shows the characteristic D band around 1310 cm^{-1}, the G band around 1600 $cm^{-1,}$ and

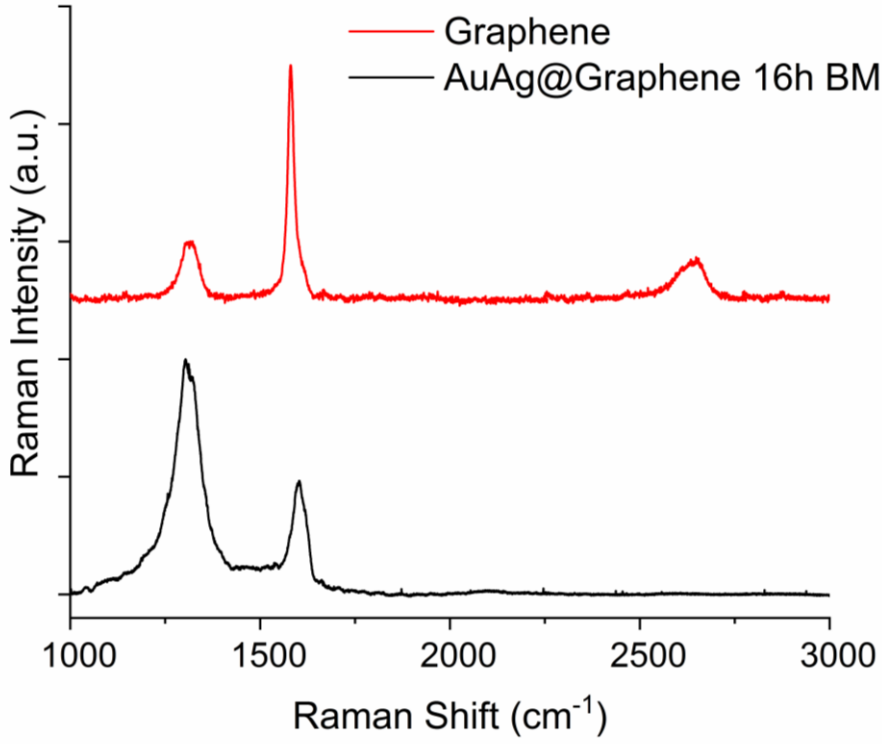

Fig. 2.4 Raman spectra of pristine graphene and of AuAg/Graphene composite made by mechanical milling.

the 2D band around 2655 cm^{-1} [57]. For symmetry reasons, the Raman spectrum of a single-layer, defect-free graphene is composed only of G and 2D bands, with the intensity of the 2D band I_{2D} larger than that of the G band I_G; moreover, the D band can only arise from an inelastic scattering of an excited charge carrier with a phonon, followed by an elastic scattering by a defect or a boundary zone, resulting in recombination. Its presence is therefore associated with a disordered kind of structure [57]. In our case, the intensity relationship between the two bands is inverted; moreover, the D band can be appreciated.

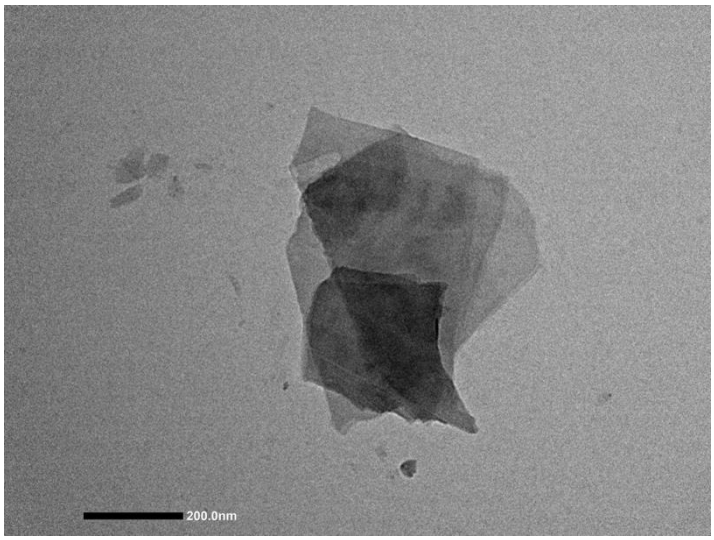

Fig. 2.5 TEM image of graphene sheets showing a multilayer structure.

These results are consistent with a multi-layer graphene structure with significant defects density and are confirmed by TEM imaging, which reveals the presence of large multi-layer sheets (Fig. 2.5). After the mechanical milling, the 2D band of the Raman spectrum had disappeared,

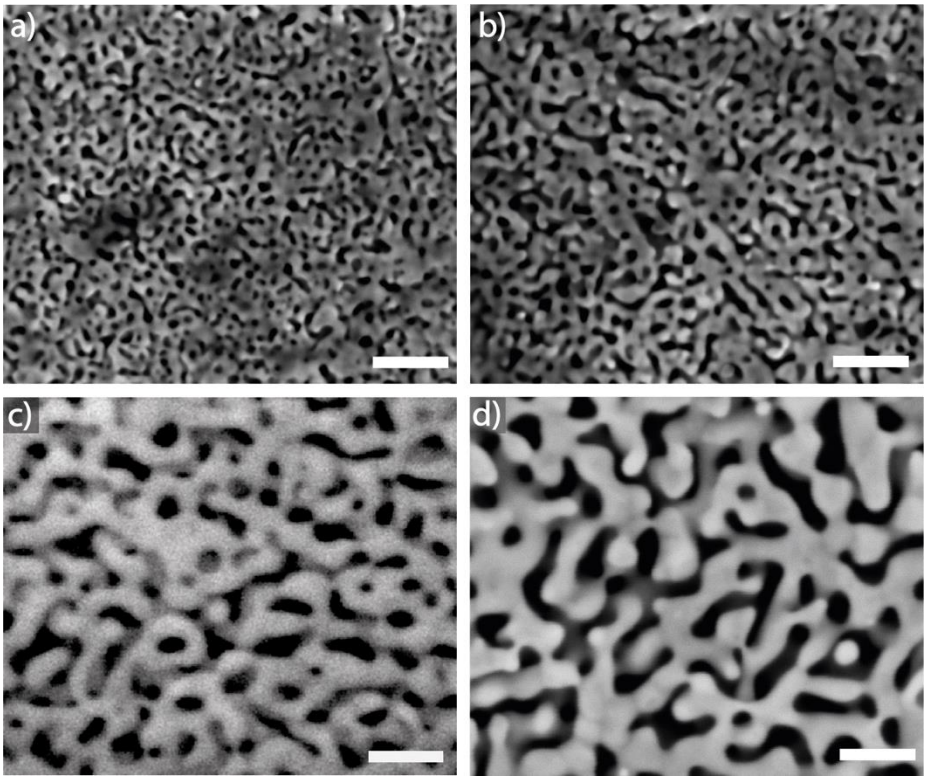

Fig. 2.6 Evolution of porosity in NP Au@G after dealloying for 15 min (a), 1 h (b), 6 h (c), 24 h (d); scale bars: 100 nm.

while the intensity of D band I_D increased with respect to I_G, suggesting a further increase in defect density.

Fig. 2.6 shows the SEM images of NP Au@G after 15 min, 1h, 6h, and 24h of immersion in concentrated HNO_3. The morphology is the typical bicontinuous network of ligaments and pores. During the immersion in HNO_3 ligament and pores coarsening can be easily appreciated. The ligament diameter distributions are shown in Fig. 2.7. It can be seen that a major shift of the distribution happens from 1 h to 6 h of treatment time. The mean ligament diameter increases from around 7 ± 2 nm after 15 min to around 23 ± 7 nm after 24 h.

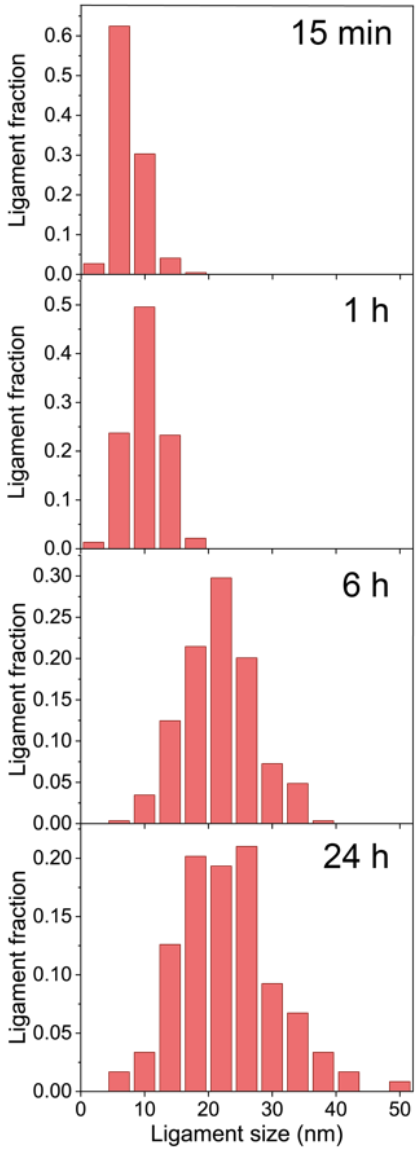

Fig. 2.7 Histogram distributions of ligament size after 15 min, 1 h, 6 h and 24 h of dealloying

Raman spectroscopy performed on NP Au@G doesn't reveal appreciable differences with respect to pristine alloy (see Fig. 2.8). In particular, it has

been shown that graphene oxide is associated with an enhanced I_G with respect to I_D [58], and so any eventual oxidation by HNO_3 exposure was not noticed from Raman spectroscopy

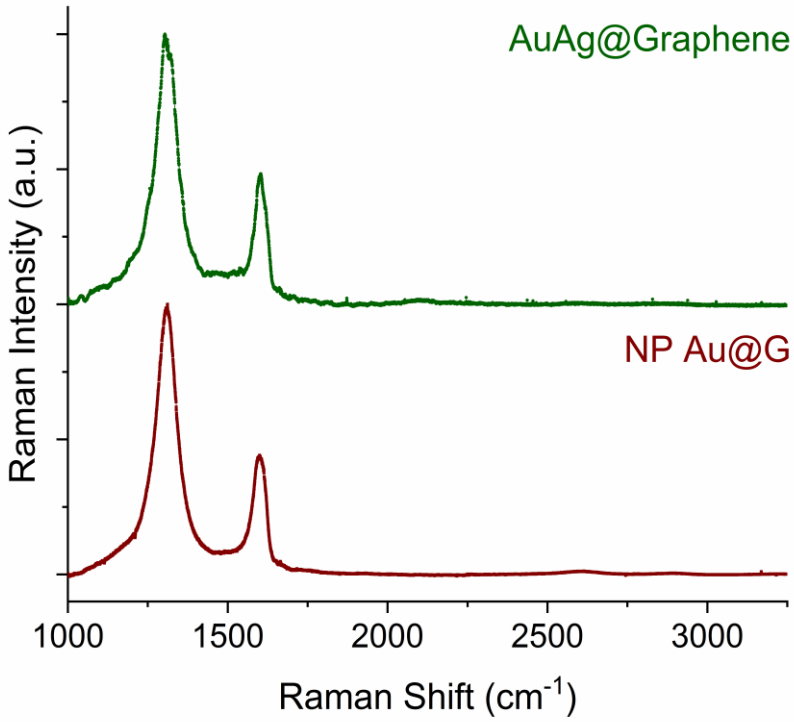

Fig. 2.8 Raman spectra of AuAg/graphene alloy and NP Au@G after 6 h of dealloying.

2.3.2 NP Cu fabrication

Fig. 2.9 shows the XRD pattern of $Cu_{20}Zn_{80}$ precursor alloy produced by mechanical alloying for 12 h. By Rietveld analysis, we estimate a composition of around 90 at. % of the ε-$CuZn_4$ and another 10 at. % of the Cu_5Zn_8 cubic phase. Further mechanical milling did not result in any increase of the ε phase content but only in the contamination level. Dealloying of CuZn pellet was carried out for different times in a 0.1 M HCl solution. The corrosion was also attempted in HCl 1 M but the high acidic concentration caused the rapid disintegration of the sample, maybe because of the stresses derived from the faster crystal structure change from HCP of the ε-phase of the alloy to FCC of Cu. The residual Zn content

after dealloying in HCl 0.1 M was estimated from weight loss measurements and is reported in Fig. 2.10.

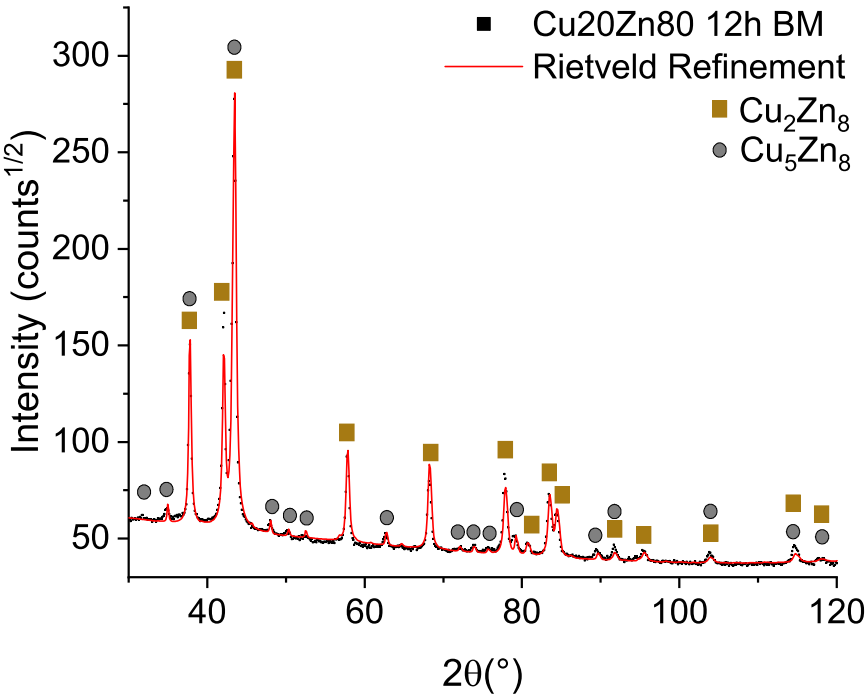

Fig. 2.9 XRD pattern of Cu20Zn80 mechanically alloyed for 12 h.

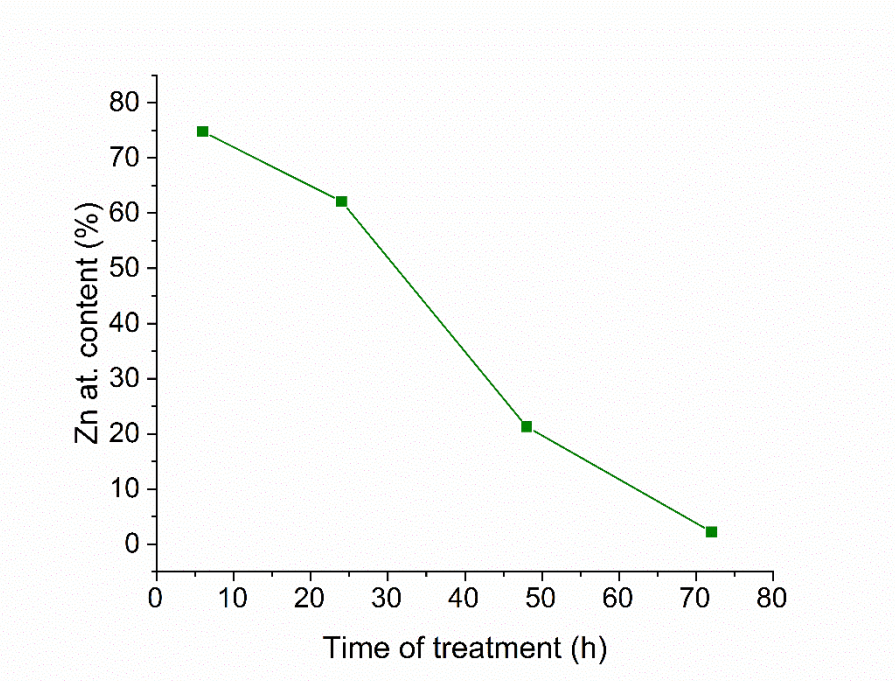

Fig. 2.10 Kinetics of the Zn content after different times of dealloying.

After 48 h the residual content was around 21 at. %, while it decreased down to around 2 at. % when was left in HCl solution for 72 h. However, after that time the sample was completely disrupted into powders. This can be caused by stresses accumulation derived from the crystal structure change during dealloying. Therefore, we consider dealloying for 48 h a good compromise between purity of the material and preservation of the monolithic form.

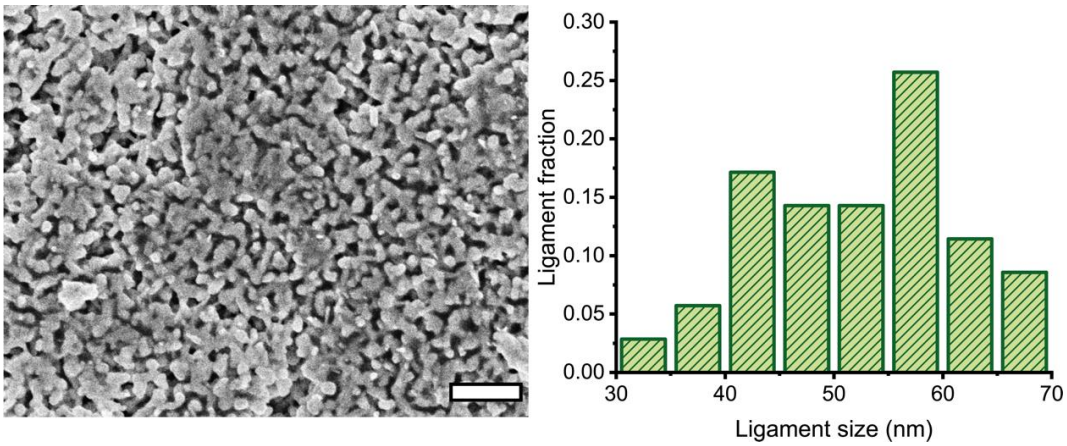

Fig. 2.11 SEM image of NP Cu surface, scale bar: 500 nm; distribution of ligament diameter of NP Cu surface.

The SEM image of the surface and the distribution of ligament thickness values are shown in Fig. 2.11. The treatment resulted in an NP surface with a mean ligament size of around 60 nm. By looking at cross-section image in Fig. 2.12, it can be seen that the porosity is extended into the sample interior, where the material is made of a homogenous and bicontinuous structure along the entire 300 µm thickness (other images can be found in **Appendix A.I**). In this case, the ligament sizes are slightly larger, with a distribution centered around 68 nm. The characteristic lengths of the material are among the smallest found in literature for NP Cu produced by CuZn precursors. However, it is still necessary to optimize the fabrication

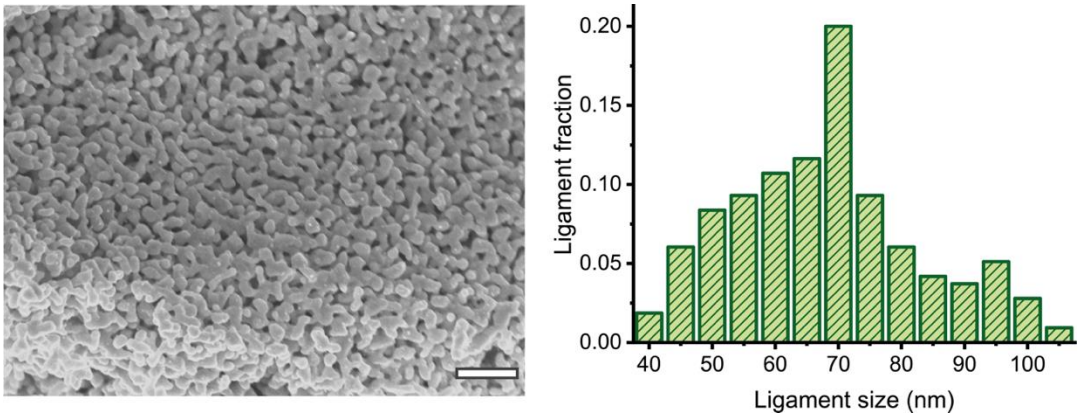

Fig. 2.12 Cross-section image of NP Cu, scale bar: 500 nm; Distribution of ligaments diameters in the cross-section.

conditions to further decrease the ligament and pore diameters, on which many important properties of NP metals strongly depend.

The fabrication of NP Cu was attempted also by VPD. Fig. 2.13a shows the surface of CuZn treated in high vacuum at 500°C for 1 h. The sample reveals an irregular and porous structure on the µm scale with a nanometric roughness that can be appreciated from the higher magnification image in Fig. 2.13b. The morphology arising from this method is very different compared to that found by chemical dealloying. This can be caused by the Cu ligaments' instability at high temperatures.

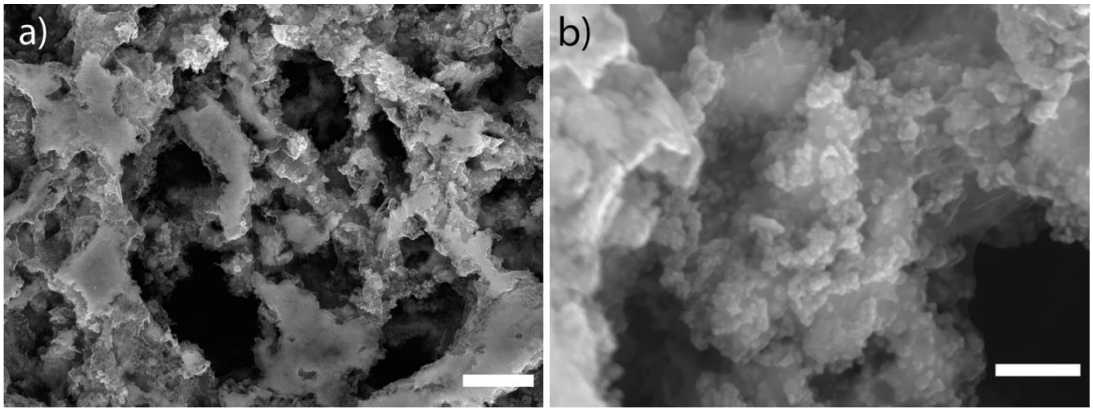

Fig. 2.13 SEM image of CuZn treated at 500°C for 1 h at lower (a, scale bar: 1 µm) and higher magnification (b, scale bar: 200 nm).

2.4 Conclusions

In this chapter, two studies of the fabrication of NP noble metals from mechanically fabricated precursors have been reported.

NP Au from an $Au_{50}Ag_{50}$ precursor alloy was prepared with a thickness of around 1-2 µm. This is quite surprising because the composition used is with an Ag content under the common parting limit for dealloying to proceed. The result can be ascribed to the surface diffusion of Au atoms at the solid-HNO_3 solution interface.

NP Au/graphene composite was produced by mechanical alloying of graphene powder with Au and Ag powders. The resulting material after dealloying was characterized through Raman spectroscopy and SEM. The as-produced material shows the presence of graphene also after dealloying and shows the typical bicontinuous nanoscale porosity of common NP Au. The material's properties could have interesting properties for different applications, from catalysis to sensing, that will be studied in future work.

NP Cu was for the first time produced from a CuZn alloy produced by mechanical milling. We studied the dealloying kinetics and we found that a treatment for 48 h was a suitable compromise between residual Zn content and mechanical stability of the monolithic sample. The material prepared is made of a bicontinuous porous structure of fine ligaments and pores, with mean characteristic lengths under 80 nm.

References

[1] J. Erlebacher, M.J. Aziz, A. Karma, N. Dimitrov, K. Sieradzki, Evolution of nanoporosity in dealloying, Nature. 410 (2001) 450–453. https://doi.org/10.1038/35068529.

[2] H. Xu, S. Pang, Y. Jin, T. Zhang, General synthesis of sponge-like ultrafine nanoporous metals by dealloying in citric acid, Nano Res. 9 (2016) 2467–2477. https://doi.org/10.1007/s12274-016-1133-7.

[3] H. Xu, T. Zhang, Formation of ultrafine spongy nanoporous metals (Ni, Cu, Pd, Ag and Au) by dealloying metallic glasses in acids with capping effect, Corros. Sci. 153 (2019) 1–11. https://doi.org/10.1016/j.corsci.2019.03.029.

[4] J. Zhang, Y. Li, Q. Zhang, Synthesis of uniform crack-free nanoporous gold by dealloying of Au-Cu alloy prepared using permanent magnetic stirring, Mater. Lett. 263 (2020) 127226. https://doi.org/10.1016/j.matlet.2019.127226.

[5] Y. Ding, Z. Zhang, Nanoporous metals for advanced energy technologies, 2016. https://doi.org/10.1007/978-3-319-29749-1.

[6] I. McCue, E. Benn, B. Gaskey, J. Erlebacher, Dealloying and Dealloyed Materials, 46 (2016) 263–286. https://doi.org/https://doi.org/10.1146/annurev-matsci-070115-031739.

[7] C. Suryanarayana, Mechanical Alloying: A Novel Technique to Synthesize Advanced Materials, Research. 2019 (2019) 1–17. https://doi.org/10.34133/2019/4219812.

[8] C. Suryanarayana, Mechanical alloying and milling, Prog. Mater. Sci. 46 (2001) 1–184. https://doi.org/10.1016/S0079-6425(99)00010-9.

[9] A. Patra, S.K. Karak, S. Pal, Effects of Mechanical Alloying on Solid Solubility, Adv. Eng. Forum. 15 (2016) 17–24. https://doi.org/10.4028/www.scientific.net/aef.15.17.

[10] L. Schultz, Formation of amorphous metals by mechanical alloying, Mater. Sci. Eng. 97 (1988) 15–23. https://doi.org/10.1016/0025-5416(88)90004-3.

[11] O.D. Neikov, Mechanical Alloying, in: Handb. Non-Ferrous Met. Powders, Elsevier, 2009: pp. 63–79. https://doi.org/10.1016/B978-1-85617-422-0.00003-3.

[12] T. Juarez, J. Biener, J. Weissmüller, A.M. Hodge, Nanoporous Metals with Structural Hierarchy: A Review, Adv. Eng. Mater. 19 (2017) 1–23. https://doi.org/10.1002/adem.201700389.

[13] M. Artymowicz D., J. Erlebacher, C. Newman R., Relationship between the parting limit for dealloying and a particular geometric high-density site percolation threshold, Philos. Mag. 89 (2009) 1663–1693. https://doi.org/10.1080/14786430903025708.

[14] H. Yin, H. Tang, D. Wang, Y. Gao, Z. Tang, Facile synthesis of surfactant-free Au cluster/graphene hybrids for high-performance oxygen reduction reaction, ACS Nano. 6 (2012) 8288–8297. https://doi.org/10.1021/nn302984x.

[15] C. Xu, X. Wang, J. Zhu, Graphene - Metal particle nanocomposites, J. Phys. Chem. C. 112 (2008) 19841–19845. https://doi.org/10.1021/jp807989b.

[16] L. Wu, H.S. Chu, W.S. Koh, E.P. Li, Highly sensitive graphene biosensors based on surface plasmon resonance, Opt. Express. 18 (2010) 14395. https://doi.org/10.1364/oe.18.014395.

[17] J. Ju, W. Chen, In situ growth of surfactant-free gold nanoparticles on nitrogen-doped graphene quantum dots for electrochemical detection of hydrogen peroxide in biological environments, Anal. Chem. 87 (2015) 1903–1910. https://doi.org/10.1021/ac5041555.

[18] C. Shan, H. Yang, D. Han, Q. Zhang, A. Ivaska, L. Niu, Graphene/AuNPs/chitosan nanocomposites film for glucose biosensing, Biosens. Bioelectron. 25 (2010) 1070–1074. https://doi.org/10.1016/j.bios.2009.09.024.

[19] Z. Xiong, L.L. Zhang, J. Ma, X.S. Zhao, Photocatalytic degradation of dyes over graphene-gold nanocomposites under visible light irradiation, Chem. Commun. 46 (2010) 6099–6101. https://doi.org/10.1039/c0cc01259a.

[20] V.K. Gupta, N. Atar, M.L. Yola, Z. Üstündağ, L. Uzun, A novel magnetic Fe@Au core-shell nanoparticles anchored graphene oxide recyclable nanocatalyst for the reduction of nitrophenol compounds, Water Res. 48 (2014) 210–217. https://doi.org/10.1016/j.watres.2013.09.027.

[21] J. Han, C. Li, Z. Lu, H. Wang, Z. Wang, K. Watanabe, M. Chen, Acta Materialia Vapor phase dealloying : A versatile approach for fabricating 3D porous materials, Acta Mater. 163 (2019) 161–172. https://doi.org/10.1016/j.actamat.2018.10.012.

[22] I.C. Cheng, A.M. Hodge, Morphology, oxidation, and mechanical behavior of nanoporous Cu foams, Adv. Eng. Mater. 14 (2012) 219–226. https://doi.org/10.1002/adem.201100252.

[23] J. Wang, S. Yang, Superior Degradation Performance of Nanoporous Copper Catalysts on Methyl Orange, Met. 2021, Vol. 11, Page 913. 11 (2021) 913. https://doi.org/10.3390/MET11060913.

[24] K. Sugawa, T. Tamura, H. Tahara, D. Yamaguchi, T. Akiyama, Metal-Enhanced Fluorescence Platforms Based on Plasmonic Ordered Copper Arrays : Wavelength Dependence of Quenching and Enhancement E ff ects, (2013) 9997–10010. https://doi.org/10.1021/nn403925d.

[25] F. Diao, X. Xiao, B. Luo, H. Sun, F. Ding, L. Ci, P. Si, Applied Surface Science Two-step fabrication of nanoporous copper films with tunable morphology for SERS application, Appl. Surf. Sci. 427 (2018) 1271–1279. https://doi.org/10.1016/j.apsusc.2017.08.117.

[26] L.Y. Chen, J.S. Yu, T. Fujita, M.W. Chen, Nanoporous copper with tunable nanoporosity for SERS applications, Adv. Funct. Mater. 19 (2009) 1221–1226. https://doi.org/10.1002/adfm.200801239.

[27] A. Liu, H. Geng, C. Xu, H. Qiu, A three-dimensional hierarchical nanoporous PdCu alloy for enhanced electrocatalysis and biosensing, Anal. Chim. Acta. 703 (2011) 172–178. https://doi.org/10.1016/J.ACA.2011.07.039.

[28] E.J. Coleman, A.C. Co, Galvanic displacement of Pt on nanoporous copper: An alternative synthetic route for obtaining robust and reliable oxygen reduction activity, J. Catal. 316 (2014) 191–200. https://doi.org/10.1016/j.jcat.2014.05.012.

[29] C. Hou, X.M. Shi, C.X. Zhao, X.Y. Lang, L.L. Zhao, Z. Wen, Y.F. Zhu, M. Zhao, J.C. Li, Q. Jiang, SnO2 nanoparticles embedded in 3D nanoporous/solid copper current collectors for high-performance reversible

lithium storage, J. Mater. Chem. A. 2 (2014) 15519–15526. https://doi.org/10.1039/c4ta02604g.

[30] G. Han, J.H. Um, H. Park, K. Hong, W.S. Yoon, H. Choe, Hierarchically structured nanoporous copper for use as lithium-ion battery anode, Scr. Mater. 163 (2019) 9–13. https://doi.org/10.1016/j.scriptamat.2018.12.030.

[31] S. Zhang, Y. Xing, T. Jiang, Z. Du, F. Li, L. He, W. Liu, A three-dimensional tin-coated nanoporous copper for lithium-ion battery anodes, J. Power Sources. 196 (2011) 6915–6919. https://doi.org/10.1016/j.jpowsour.2010.12.021.

[32] Z. Wang, J. Liu, C. Qin, H. Yu, X. Xia, C. Wang, Y. Zhang, Q. Hu, W. Zhao, Dealloying of cu-based metallic glasses in acidic solutions: Products and energy storage applications, Nanomaterials. 5 (2015) 697–721. https://doi.org/10.3390/nano5020697.

[33] M. Li, J. Liu, C. Wang, Y. Liu, Y. Sun, C. Qin, Z. Wang, Y. Li, L. Liu, S. Liu, Controllable nanoporous copper synthesized by dealloying metallic glasses: New insights into the tuning pore structure and applications, Chem. Eng. J. 427 (2022) 130861. https://doi.org/10.1016/j.cej.2021.130861.

[34] S. Sattayasamitsathit, P. Thavarungkul, C. Thammakhet, W. Limbut, A. Numnuam, C. Buranachai, P. Kanatharana, Fabrication of Nanoporous Copper Film for Electrochemical Detection of Glucose, Electroanalysis. 21 (2009) 2371–2377. https://doi.org/10.1002/elan.200904697.

[35] F. Jia, C. Yu, K. Deng, L. Zhang, Nanoporous metal (Cu, Ag, Au) films with high surface area: General fabrication and preliminary electrochemical performance, J. Phys. Chem. C. 111 (2007) 8424–8431. https://doi.org/10.1021/jp071815y.

[36] T. Jin, M. Yan, Menggenbateer, T. Minato, M. Bao, Y. Yamamoto, Nanoporous Copper Metal Catalyst in Click Chemistry: Nanoporosity-Dependent Activity without Supports and Bases, Adv. Synth. Catal. 353 (2011) 3095–3100. https://doi.org/10.1002/ADSC.201100760.

[37] J.R. Hayes, A.M. Hodge, J. Biener, A. V Hamza, K. Sieradzki, Monolithic nanoporous copper by dealloying Mn-Cu, J. Mater. Res. 21 (2006) 2611–2616. https://doi.org/10.1557/jmr.2006.0322.

[38] A. Aziz, J. Carrasco, Y. Grosu, Towards tuning the modality of hierarchical macro-nanoporous metals by controlling the dealloying kinetics

of close-to-eutectic alloys, Phys. Chem. Chem. Phys. 23 (2021) 25388–25400. https://doi.org/10.1039/d1cp03878h.

[39] Z.H. Dan, F.X. Qin, N. Hara, The refinement of the nanoporous copper by adding third elements, in: Mater. Sci. Forum, Trans Tech Publications Ltd, 2014: pp. 1986–1989. https://doi.org/10.4028/www.scientific.net/msf.783-786.1986.

[40] Y.Y. Zhao, F. Qian, C. Zhao, C. Xie, J. Wang, C. Chang, Y. Li, L.C. Zhang, Facile fabrication of ultrathin freestanding nanoporous Cu and Cu-Ag films with high SERS sensitivity by dealloying Mg-Cu(Ag)-Gd metallic glasses, J. Mater. Sci. Technol. 70 (2021) 205–213. https://doi.org/10.1016/j.jmst.2020.08.049.

[41] N.T. Tuan, J. Park, J. Lee, J. Gwak, D. Lee, Synthesis of nanoporous Cu films by dealloying of electrochemically deposited Cu-Zn alloy films, Corros. Sci. 80 (2014) 7–11. https://doi.org/10.1016/j.corsci.2013.11.043.

[42] T. Egle, C. Barroo, N. Janvelyan, A.C. Baumgaertel, A.J. Akey, M.M. Biener, C.M. Friend, D.C. Bell, J. Biener, Multiscale Morphology of Nanoporous Copper Made from Intermetallic Phases, ACS Appl. Mater. Interfaces. 9 (2017) 25615–25622. https://doi.org/10.1021/acsami.7b05648.

[43] K. Mohan, N. Shahane, R. Sosa, S. Khan, P.M. Raj, A. Antoniou, V. Smet, R. Tummala, Demonstration of Patternable All-Cu Compliant Interconnections with Enhanced Manufacturability in Chip-to-Substrate Applications, in: Proc. - Electron. Components Technol. Conf., Institute of Electrical and Electronics Engineers Inc., 2018: pp. 301–307. https://doi.org/10.1109/ECTC.2018.00053.

[44] C. Yang, Q.B. Zhang, M.Y. Gao, Y.X. Hua, C.Y. Xu, In Situ Electrochemical Fabrication of Three Dimensional Hierarchical Nanoporous Copper Films and Their Electrocatalytic Performance, J. Electrochem. Soc. 163 (2016) D469–D475. https://doi.org/10.1149/2.0461609jes.

[45] Y. Tang, B. Tang, J. Qing, Q. Li, L. Lu, Nanoporous metallic surface: Facile fabrication and enhancement of boiling heat transfer, Appl. Surf. Sci. 258 (2012) 8747–8751. https://doi.org/10.1016/j.apsusc.2012.05.085.

[46] B. Hecker, C. Dosche, J. Knake, M. Oezaslan, Preparation and Characterization of Nanoporous Copper Films by Chemical Dealloying, ECS Trans. 80 (2017) 541–550. https://doi.org/10.1149/08010.0541ECST/XML.

[47] B. Hecker, C. Dosche, M. Oezaslan, Ligament Evolution in Nanoporous Cu Films Prepared by Dealloying, J. Phys. Chem. C. 122 (2018) 26378–26384. https://doi.org/10.1021/acs.jpcc.8b06801.

[48] S. Vivegnis, M. Krid, J. Delhalle, Z. Mekhalif, F.U. Renner, Use of pyrophosphate and boric acid additives in the copper-zinc alloy electrodeposition and chemical dealloying, J. Electroanal. Chem. 848 (2019) 113310. https://doi.org/10.1016/j.jelechem.2019.113310.

[49] Q.B. Zhang, A.P. Abbott, C. Yang, Electrochemical fabrication of nanoporous copper films in choline chloride–urea deep eutectic solvent, Phys. Chem. Chem. Phys. 17 (2015) 14702–14709. https://doi.org/10.1039/C5CP01276G.

[50] K. Li, X. Liu, M. Chen, S. Liu, Preparation and performances of nanoporous copper for low temperature bonding, in: Proc. Electron. Packag. Technol. Conf. EPTC, Institute of Electrical and Electronics Engineers Inc., 2014: pp. 14–18. https://doi.org/10.1109/ICEPT.2014.6922561.

[51] H. Yue, C. Zhang, Z. Yang, H. Wang, G. Ding, X. Zhao, A preparation method of patterned nanoporous copper, in: Adv. Mater. Res., Trans Tech Publications Ltd, 2013: pp. 322–325. https://doi.org/10.4028/www.scientific.net/AMR.663.322.

[52] R. Mao, S. Liang, X. Wang, Q. Yang, B. Han, Effect of preparation conditions on morphology and thermal stability of nanoporous copper, Corros. Sci. 60 (2012) 231–237. https://doi.org/10.1016/j.corsci.2012.03.032.

[53] Q. Yang, S. Liang, B. Han, J. Wang, R. Mao, Preparation and properties of enhanced bulk nanoporous coppers, Mater. Lett. 73 (2012) 136–138. https://doi.org/10.1016/j.matlet.2012.01.027.

[54] S.M. Liang, R. Schmid-Fetzer, Thermodynamic assessment of the Al-Cu-Zn system, part II: Al-Cu binary system, Calphad Comput. Coupling Phase Diagrams Thermochem. 51 (2015) 252–260. https://doi.org/10.1016/j.calphad.2015.10.004.

[55] J. Schindelin, I. Arganda-Carreras, E. Frise, V. Kaynig, M. Longair, T. Pietzsch, S. Preibisch, C. Rueden, S. Saalfeld, B. Schmid, J.Y. Tinevez, D.J. White, V. Hartenstein, K. Eliceiri, P. Tomancak, A. Cardona, Fiji: An open-source platform for biological-image analysis, Nat. Methods. 9 (2012) 676–682. https://doi.org/10.1038/nmeth.2019.

[56] H.M. Rietveld, A profile refinement method for nuclear and magnetic structures, J. Appl. Crystallogr. 2 (1969) 65–71. https://doi.org/10.1107/s0021889869006558.

[57] L.M. Malard, M.A. Pimenta, G. Dresselhaus, M.S. Dresselhaus, Raman spectroscopy in graphene, Phys. Rep. 473 (2009) 51–87. https://doi.org/10.1016/j.physrep.2009.02.003.

[58] I. Childres, L.A. Jauregui, W. Park, H. Caoa, Y.P. Chena, Raman spectroscopy of graphene and related materials, in: New Dev. Phot. Mater. Res., 2013: pp. 403–418.

Chapter 3

On the thermal stability of NP Au

3.1 Introduction

Coarsening has been previously introduced in **Chapter 1** with a description of the ideal process and its influence on the properties and applications of NP metals. In this chapter, we dwell on the interpretation of different behaviors that can be found in the literature for the special case of NP Au. We focus on NP Au since it is the most studied NP metal and there is a good amount of data available to be compared. Besides, a common problem in this field is that the properties of NP metals are influenced by many parameters, often not all described in experimental procedures. It is therefore difficult to understand the causes of different results between experimental procedures, especially without a good number of studies. Ideally, coarsening is regarded as a surface diffusion process that makes NP Au evolve in a self-similar way without densification [1]. However, several reports show that thermal treatments can also lead to non-self-similar structures, with partial densification or even with a complete collapse of the porous structure [2-4]. Moreover, the evolution of ligament and pore sizes can greatly vary from paper to paper [4,5]. In this chapter, we attempted to understand the reasons that bring to such different behaviors, through interpretation and image analysis (IA) of published reports and by experimental work. Particular attention will be paid to the effect of different forms and microstructures of the precursor alloys used for NP Au fabrication. For this reason, a brief description of common NP Au precursor alloys is given.

Common monolithic AuAg alloys used for the fabrication of NP Au are commercial products or are made in lab by melting, casting, subsequent annealing for homogenization and residual stresses relief. This is a standard procedure that is probably used also for commercial products. It gives rise to grain sizes that can range from few to hundreds of μm and so, at least two orders of magnitude larger than ligament and pore sizes of NP Au [6-8]. A different discussion should be made for 2D and 1D parent alloys such as thin films, micro- and nanowires. In this case, the preparative usually involves deposition methods such as sputtering or physical vapor deposition (PVD), processes that lead to smaller grain sizes. An exception is represented by the commonly called “gold leaf”, an AuAg thin foil with thickness down to 100 nm, obtained by hammering thicker rolled foils. In this case, the alloy is prepared by the common melting, casting, and

annealing before the mechanical thinning. Thus, the leaf presents grain sizes comparable to those of macroscopic 3D samples. As mentioned in **Chapter 1**, during and after dealloying the material preserves the crystal orientation and grain size of the parent alloy – apart from the exceptions in which the precursor alloy has a different type of crystal unit cell or has an amorphous structure – leading to an NP metal with same crystal orientation and grain size of the parent alloy. The influence of the alloy type on the thermal stability of NP Au will be the major subject of the study based on analysis of literature data.

Moreover, to clarify the role of microstructure on the thermal stability of NP Au, we studied the behavior of NP Au produced from an AuAg precursor prepared by mechanical alloying, a process that generally leads to the formation of nanocrystalline materials [9]. Since, as said in **Chapter 1**, dealloying preserves the initial microstructure of the parent alloy, we produced a nanocrystalline NP Au from this precursor. We found that NP Au produced in this way presents low thermal stability, which can be enhanced by performing thermal annealing before dealloying.

3.2 Materials and methods

3.2.1 NP Au fabrication

AuAg alloy fabrication

2g of AuAg powder mixture was prepared in an atomic ratio of 30:70. The powders were mechanically milled in a SPEX *8000M Mixer/Mill* ball mill for 16h in a hardened steel vial with two hardened steel balls of 8g each. The powders were removed from the sides of the vial every 30 minutes in the first 2 hours and then every 5 hours, to homogenize the mixture. Pellets of 1.3 cm of diameter and 1 mm of thickness were prepared by cold pressing under 10 tons for 5 min with a hydraulic press.

Dealloying of AuAg alloy

NP Au was prepared by chemical dissolution of Ag in concentrated HNO_3 for 24h. During the treatment, the acidic solution was repeatedly stirred. After the treatment, the pellets were rinsed three times and stored in ultrapure water for 24h. Then, the samples were dried in a desiccator.

Post-dealloying annealing treatments

The dealloyed NP Au samples were subjected to thermal treatments at 100°C, 200°C, 300°C, 400°C and at 600°C for 1h in an SN 388589 (Nabertherm GmbH, Bremen, Germany) oven in air. The samples were quickly inserted into the oven when it had reached a stable target temperature.

3.2.2 Scanning Electron Microscopy measurements

Scanning Electron Microscopy (SEM) was carried out with an S400 (Hitachi, Tokyo, Japan) scanning electron microscope, equipped with an Everhart-Thornley secondary electrons detector and an UltraDry EDS detector (Thermo Fisher Scientific, Waltham, MA, USA).

3.2.3 X-Ray Diffraction Measurements

X-Ray Diffraction (XRD) measurements were carried out with a Rigaku *Miniflex II* diffractometer with a Bragg-Brentano geometry working in a $\theta - 2\theta$ configuration. Quantitative phase and microstructure analysis were performed through an extended Rietveld refinement method [10,11] using MAUD software.

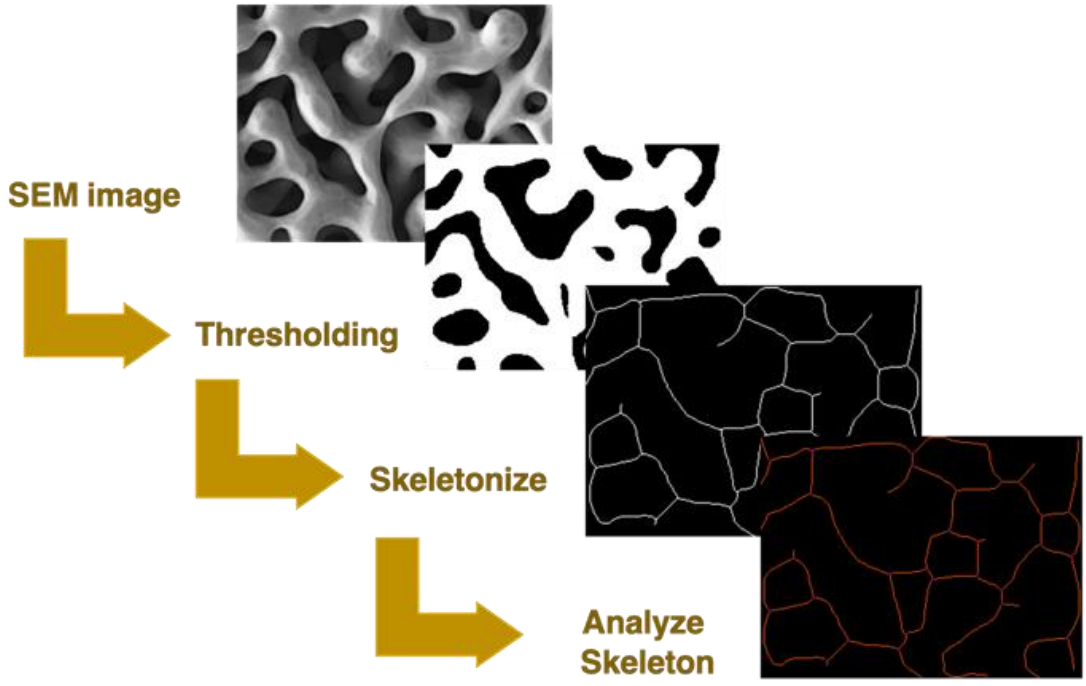

Fig. 3.1 Scheme of image analysis by thresholding, skeletonization and successive analysis through Fiji.

3.2.4 Image analysis

SEM images were collected and analyzed from our measurements and literature [2–5,12-18] with Fiji [19]. The images were firstly binarized, then different procedures were applied to obtain different parameters:

- ligament diameters were measured manually through *Measure* function;
- pore diameters, pore densities, the perimeter per unit of surface, and the density of the material were measured through the function *Analyze Particles*. In this algorithm, pores are fitted as ellipses and the mean diameter is estimated as the average between major and minor axis of the ellipse;
- ligament lengths, ligament and node density were measured by converting the binarized image in a skeleton of branches and nodes, by using the *skeletonize* function. The output was then analyzed through *analyze skeleton* function. The process is illustrated in Fig. 3.1.

3.3 Results and Discussion

IA was firstly performed on literature data indicated in paragraph 3.2.4, to check for some relationship between initial features of dealloyed NP Au and its evolution after thermal treatment. In particular, Fig. 3.2 shows the relationship between ligament diameter (or thickness) s after a thermal treatment and initial values of sample thickness, aspect ratio (ligament diameter/length ratio) s_0/l_0, density d_0 and ligament thickness s_0. The treatments were subdivided into classes defined by the temperature of the treatment. From these data, it can be observed that the studied initial parameters are not strictly related to the NP morphology evolution after annealing. This is probably due to the surface diffusion nature of coarsening, which is heavily influenced by the atomic-scale surface state of ligaments, of which we don't have sufficient knowledge.

On the other side, although coarsening, as a surface diffusion phenomenon, shouldn't bring itself densification, several papers reported this phenomenon, which becomes predominant at certain annealing conditions and can even bring to the complete collapse of the 3D porous structure

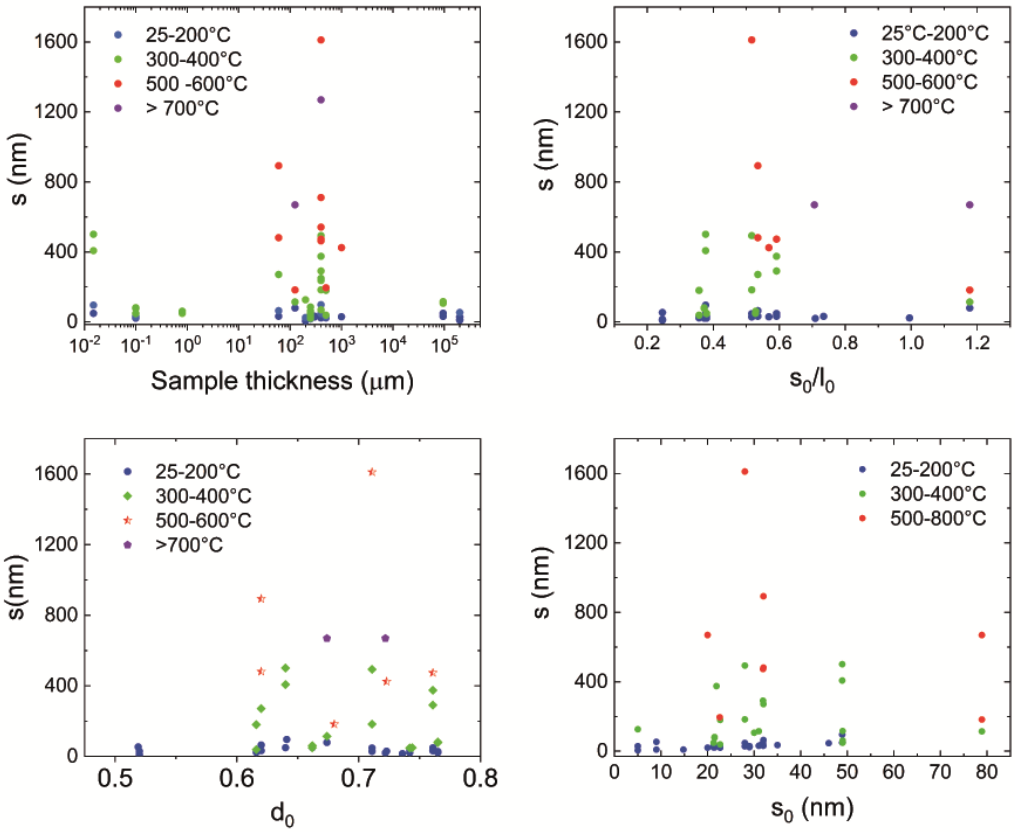

Fig. 3.2 Ligament thickness of NP Au versus initial values of ligament thickness, aspect ratio, density and sample thickness.

[2,4,14]. By studying literature data, we firstly observed a common characteristic of NP Au coarsening: the major changes in the structure happen at temperatures higher than 300°C, regardless of the time of the treatment. Therefore, in order to discern among samples that tend or not to densify, we selected only papers which report the material behavior for temperatures equal to or higher than 300°C: 19 papers were found to satisfy this requirement [1–5,12,14,18,20-30]. Among them we found 8 cases in which densification is prominent [2,4,5,12,14,20,21,26] and 11 in which there isn't or is minimal [1,3,5,17,18,22–25,27,30]. 5 cases of the first group (63 %) are thin films, nanowires, or nanoparticles [2,4,14,20,21]; 2 cases are macroscopic AuAg alloys [5,26] and one is a macroscopic AuAgCuNiZn alloy, whose microstructure wasn't reported [12]; among the second group, the 82 % is occupied by bulk AuAg alloys [1,17,18,23–25,27,28,30], another case is of a 100 nm thick gold leaves [3], that, as said before, present coarse grains, and another from an intermediate thickness of 1 μm gold leaf [22].

From the other side, as it is known, the morphology of ligament/pore structure of the dealloyed systems hasn't specific correlation with the sample form and we can find bicontinuous and tunable structures produced both from 0D, 1D, 2D, and 3D materials. From these observations, it seems clear that densification is a process that heavily depends on the form of the material and is not proper of the nanoporous structure morphology. The different behavior can be caused by stresses that arise from geometrical constraints, that lead to shrinkage and the consequent pore closing. Moreover, as said in the introduction of the chapter, the grain size of low-dimensional samples can be smaller as a result of the different preparation methods. Besides, the only two cases of thin films stable against densification were made from a coarse-grained precursor but there is also a case in which, even if the structure doesn't collapse, the leaf densifies [2]. Thus, there are a too small number of cases for making a certain conclusion about this last issue.

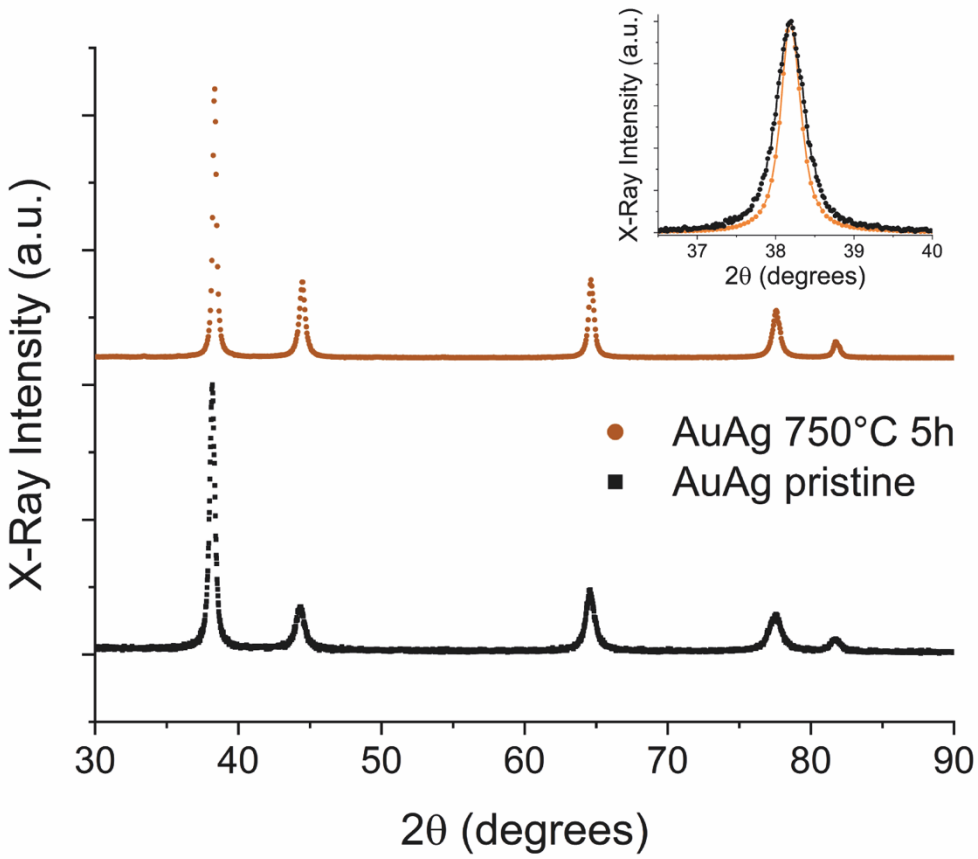

Fig. 3.3 XRD pattern of NPA and PA samples.

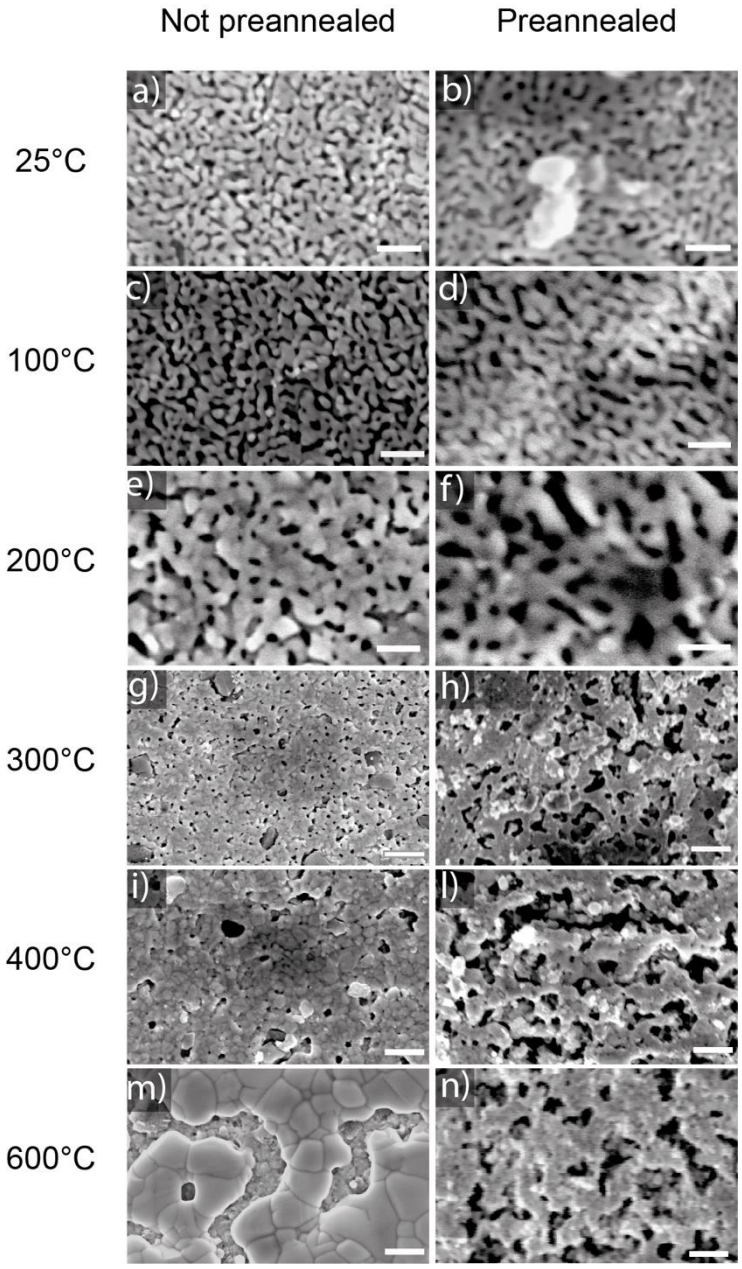

Fig. 3.4 SEM images of NPA NP Au as prepared (a), after thermal treatment for 1 h at 100°C (c), 200°C (e), 300°C (g), 400°C (i), 600°C (m) and images of PA NP Au as prepared (b)), after thermal treatment for 1 h at 100°C (b), 200°C (f), 300°C (h), 400°C (l), 600°C (n). Scale bars: a-f: 200 nm, g-n: 1 µm.

With the purpose of better understanding the microstructure role, we studied its influence on the thermal stability of NP Au by experimental work. NP Au was produced by nanocrystalline mechanically alloyed $Au_{30}Ag_{70}$ alloys and we studied the influence of annealing prior to dealloying. XRD measurements of not preannealed (NPA) and preannealed (PA) AuAg pellets are reported in Fig. 3.3 and present the known peaks related to Au and Ag crystal structure. As shown in the inset for the (111) reflection, the peaks of the PA sample are narrower than those of the NPA specimen.

Rietveld refinement was performed on both patterns to calculate the grain size of the alloys: the pristine alloy shows a crystallite size around 30 nm, while the annealed one around 50 nm.

Both the samples were subjected to dealloying in HNO_3 70% for 24 h. SEM images of the resulting materials are shown in Fig. 3.4a and Fig. 3.4b: they show a bicontinuous porous structure, with ligament diameters around 30 nm, ligament lengths around 50 nm and pore diameters around 40 nm.

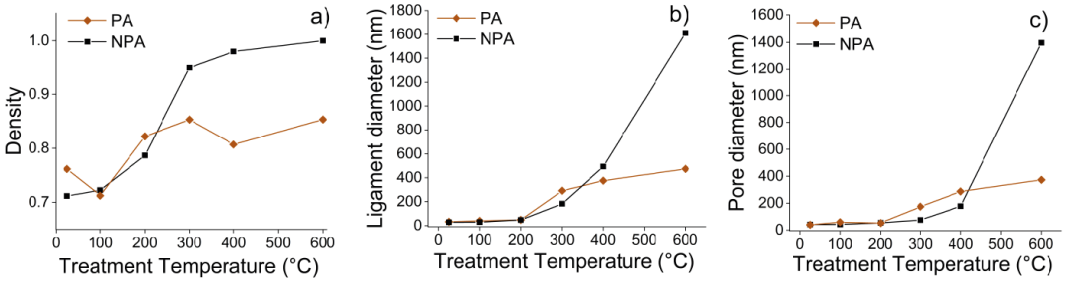

Fig. 3.5 Trends of density (a), ligament diameter (b) and pore diameter (c) versus temperature of treatment.

Besides, the thermal annealing didn't bring any important variation in the dealloyed NP morphology. NP Au images after thermal treatments for 1 h at 100 °C, 200°C, 300°C, 400°C, and 600°C are shown in Fig. 3.4c-n for either NPA either PA samples, which both present rounded ligaments after thermal treatments up to 200°C. Above this temperature, the ligaments become facetted and important differences can be found between the NPA and PA porous structures. The NPA material shows an important densification trend from an initial 70% to almost 100% for the sample annealed at 600°C. At 300°C the structure is already collapsing. The observations are confirmed by IA results, as can be seen in Fig. 3.5a. On the other side, the pre-annealed sample shows enhanced thermal stability, resulting in reduced densification and smaller coarsening of characteristic lengths. The latter can be observed in Fig. 3.5b and Fig. 3.5c, where ligament and pore diameter trends are shown, respectively. The preannealing effect on thermal stability is therefore fundamental for preserving the porous structure at high temperatures.

In addition, looking at Fig. 3.5, it can be noted that also for the preannealed NP Au, the structure observes the major changes between 200°C and 300°C. The density grows by 8% from an initial value around 0.76 to around 0.82 at 200°C and by only 3% from 200°C to 600°C, temperature at which it is around 0.85. In addition, distribution curves of ligament diameters and lengths, and of pore diameters have been made. Since they present a similar trend over temperature, in Fig. 3.6 we just show the ligament diameter distributions at 25°C, 200°C, 400°C, and 600°C. The distributions

are asymmetric and for this reason, we chose a lognormal function to fit them:

$$f(x) = \frac{e^{-\frac{(lnx-\mu)^2}{2\sigma^2}}}{x\sqrt{2\pi}\sigma} \qquad for\ x > 0 \qquad \text{Eq. 3-1}$$

The normalized curves over normalized ligament thickness values, plotted in Fig. 3.8, reveal two groups of similar curves: from 25°C to 200°C and from 300°C to 600°C. Indeed, for temperatures higher than 300°C, the distributions are wider and with longer codes to higher values of thickness. This is another indication of how the structure drastically changes from this temperature. Moreover, from Fig. 3.5 and Fig. 3.8 we can see that the sample treated at 100°C presents the lowest density and narrower distribution, while its ligaments and pores have comparable sizes with those

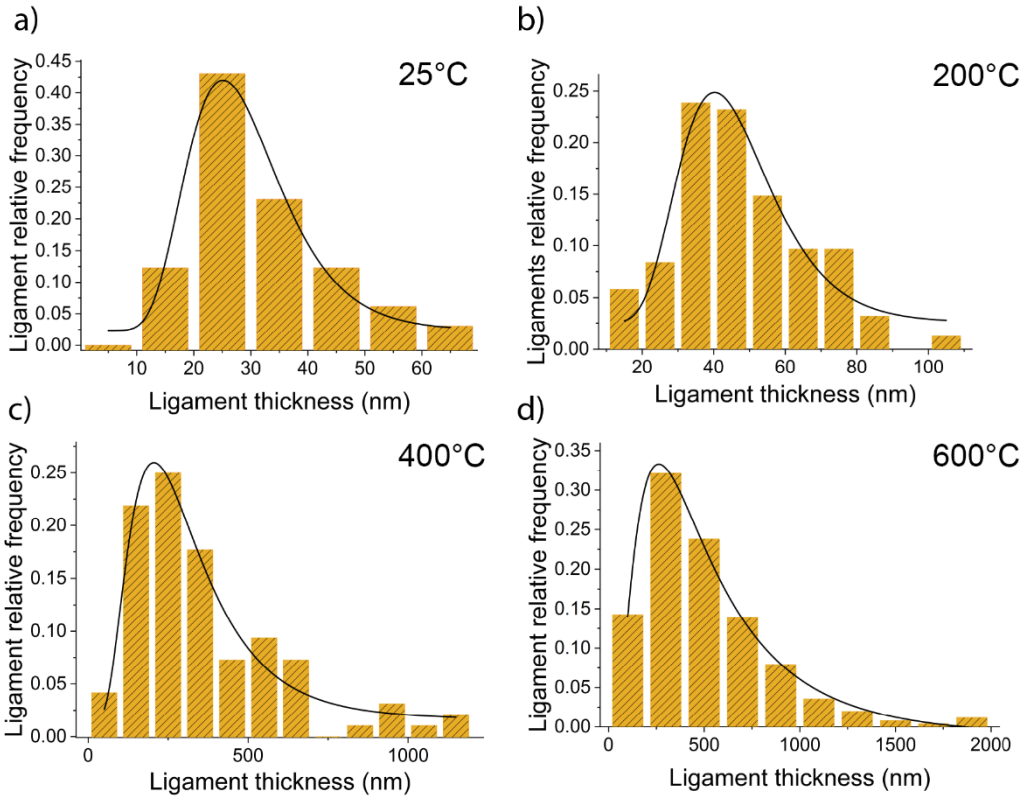

Fig. 3.6 Distribution curves of preannealed NP Au as-dealloyed (a), after annealing at 200°C (b), 400°C (c) and 600°C (d).

of the as-dealloyed sample. A possible explanation is that at this temperature, coarsening does not still occur, but the increased atomic diffusivity leads firstly to a reorganization of the ligaments' structure by surface diffusion.

The beneficial effect of preannealing on the thermal stability can be ascribed to a decrease of grain boundaries concentration, due to the larger grain size of PA NP Au of about 67 %. This is a significant difference at this scale, where grain boundary density heavily varies with grain size [31]. Besides, it is known that grain boundary diffusion causes densification [32-34], while surface diffusion doesn't [35]. Therefore, the lowering of the density of grain boundaries compared to the surface area probably led to a decrease in densification in the PA sample.

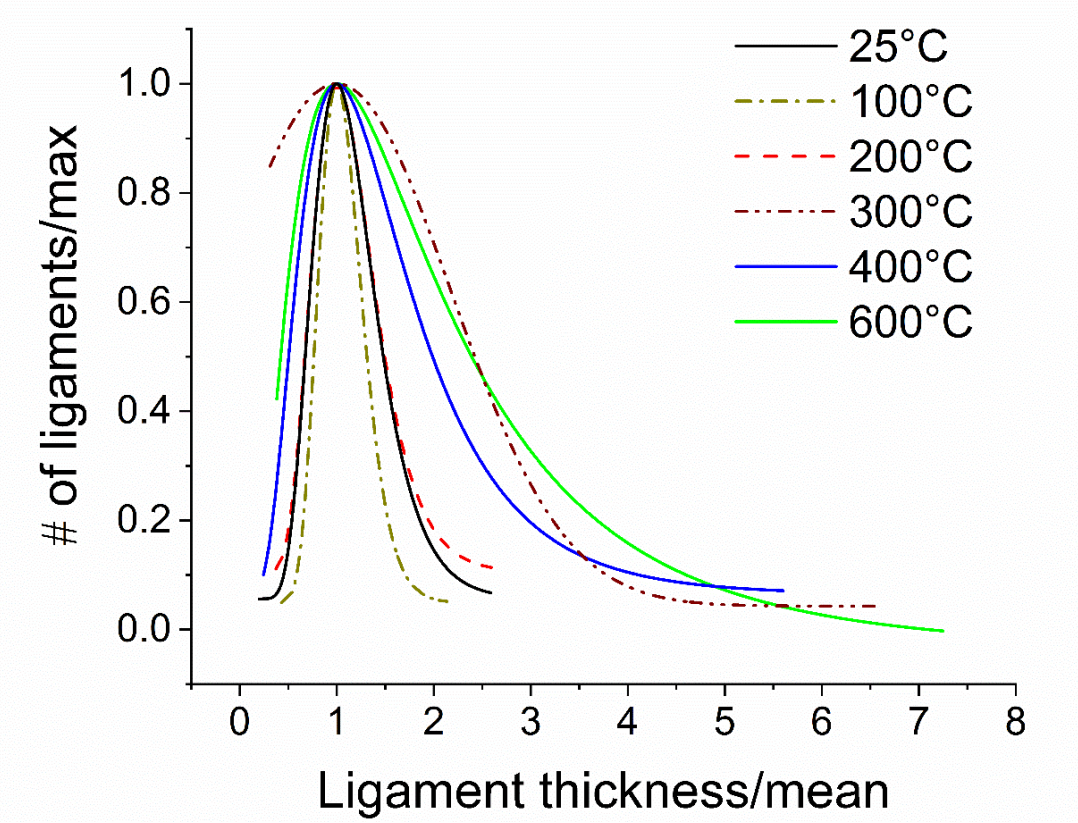

Fig. 3.7 Distribution curves of ligament thickness of preannealed NP Au, wherein either the number (#) of ligaments either the ligament thickness values were normalized by their maximum values.

The evolution of the as-fabricated NP Au samples has been compared with data analyzed from papers object of the above discussion: Fig. 3.7 shows the evolution of density at different temperature values, while Fig. 3.9 shows the temperature trends of ligament diameter and length, and of pore diameter. To give to the reader a better view, only some representative trends were plotted together with those observed in our samples: we show those of the 3D samples made by Badwe et al. [18], Sun et al. [5], and Qian et al. [29] and of thin microbeams of NP Au fabricated by Seker et al. [4]. NPA NP Au prepared by us presents much lower stability compared to commonly produced NP Au examples. PA NP Au displays ligament and pore sizes comparable with those reported in the literature, while it still shows more significant densification compared to 3D samples of NP Au

produced from AuAg alloys, being more similar to the behavior observed by Seker et al. in their fabricated microbeams [4]. The larger increase in density of PA NP Au compared with the majority of 3D NP Au samples can be ascribed to grain sizes still smaller than those of common NP Au. These

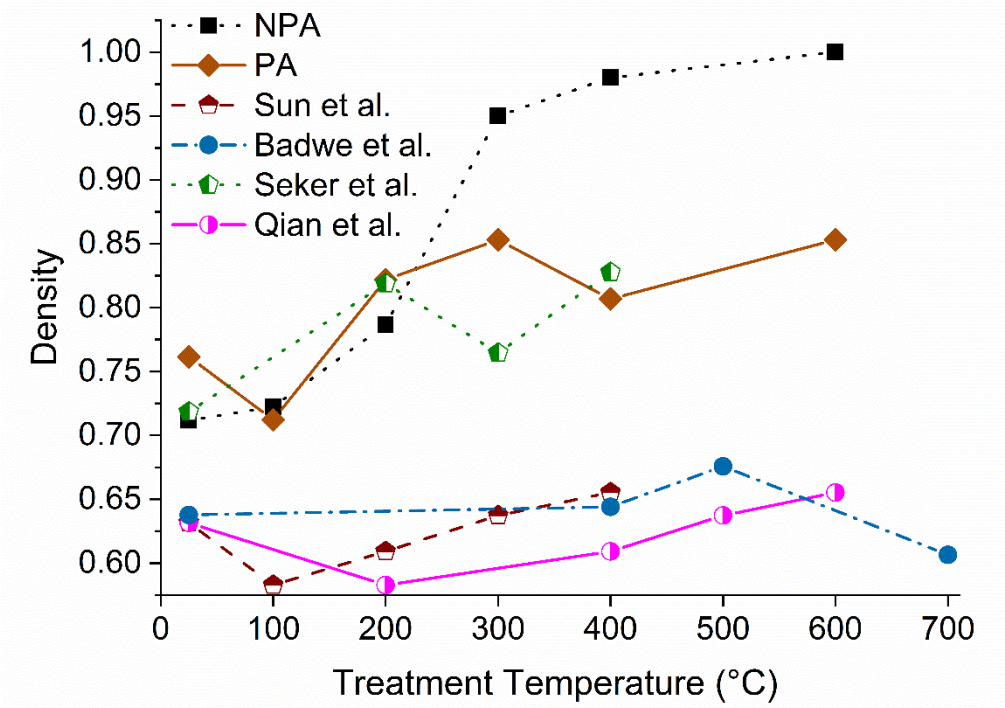

Fig. 3.8 Density trends over annealing temperature of our samples and literature ones. The samples in the selected reports were submitted to annealing for 10 min (Seker et al. [4] and Sun et al. [5]), 15 min (Badwe et al. [18]) and 120 min (Qian et al. [29]).

observations confirm that the microstructure heavily influences the NP Au structure at high temperatures, while it doesn't bring significant effects in the morphology during dealloying. Furthermore, the work shows that the thermal stability of NP Au produced by mechanical alloying depends on temperature treatments made before the dealloying.

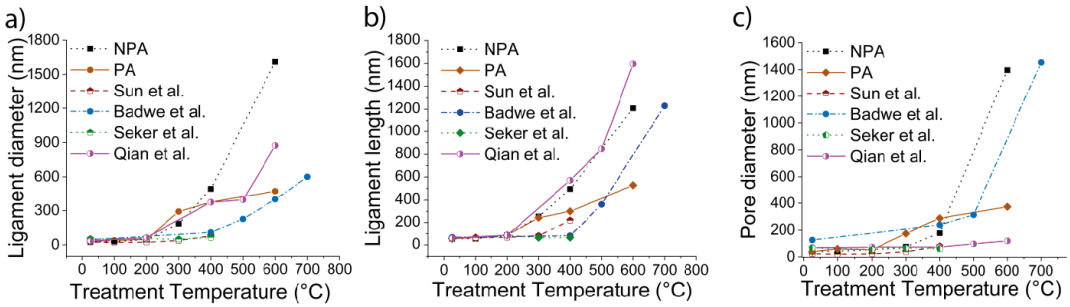

Fig. 3.9 Values of ligament diameter (a), ligament length (b), pore diameter (c) at different treatment temperatures from image analysis of our samples and literature ones.

It is thus necessary to optimize this procedure to further reduce the densification in the material in potential applications at high temperatures. It is probably necessary to achieve grain sizes larger than the ligament sizes at least by one or two orders of magnitude, in order to make surface diffusion the dominant process during coarsening. Thermal treatments at 750°C for 12 h and at 950°C for 5 h didn't bring any appreciable difference in grain size and thermal stability. The effect of longer annealing times will be studied in future investigations.

3.4 Conclusions

This chapter attempts to explore the possible causes of different coarsening behaviors published in the literature concerning NP Au. We found an important heterogeneity of ligament and pore sizes which is not directly linkable with morphological features and fabrication form of dealloyed NP Au. This can be caused by the dominant phenomenon of coarsening, the surface diffusion, which heavily depends on the atomic-scale surface state of the ligaments. Moreover, while it is believed that NP metals' coarsening doesn't involve densification, several reports demonstrate the contrary. By taking into account the differences between papers that report important densification or breakdown of the porous network, it seems that NP metals with one or more dimensions of micro/nano scale or with complex microstructures present lower thermal stability. Moreover, we also show experimentally that the precursor alloy microstructure heavily influences NP Au structure evolution during thermal treatments, influencing both the density and the characteristic lengths of the material. In particular, nanocrystalline NP Au produced by mechanically alloyed AuAg precursors shows lower thermal stability, which makes it not suitable for applications above 200°C without any further treatment. Pre-dealloying annealing of the alloy has been found to be beneficial, by reducing ligament and pore coarsening and reducing the densification. The latter is still more pronounced than in monolithic coarse-grained NP Au produced by AuAg alloys, due to grain sizes still comparable with ligament sizes, in our system. Further efforts will be made to find proper pre-dealloying treatments, in order to obtain coarse-grained AuAg precursor from mechanical alloying.

References

[1] H. Jeon, N.R. Kang, E.J. Gwak, J. il Jang, H.N. Han, J.Y. Hwang, S. Lee, J.Y. Kim, Self-similarity in the structure of coarsened nanoporous gold, Scr. Mater. 137 (2017) 46–49. https://doi.org/10.1016/j.scriptamat.2017.05.009.

[2] A.Y. Chen, S.S. Shi, F. Liu, Y. Wang, X. Li, J.F. Gu, X.F. Xie, Effect of annealing atmosphere on the thermal coarsening of nanoporous gold films, Appl. Surf. Sci. 355 (2015) 133–138. https://doi.org/10.1016/j.apsusc.2015.07.065.

[3] S. Kuwano-Nakatani, T. Fujita, K. Uchisawa, D. Umetsu, Y. Kase, Y. Kowata, K. Chiba, T. Tokunaga, S. Arai, Y. Yamamoto, N. Tanaka, M. Chen, Environment-Sensitive Thermal Coarsening of Nanoporous Gold, Mater. Trans. 56 (2015) 468–472. https://doi.org/10.2320/MATERTRANS.MF201403.

[4] E. Seker, J.T. Gaskins, H. Bart-Smith, J. Zhu, M.L. Reed, G. Zangari, R. Kelly, M.R. Begley, The effects of post-fabrication annealing on the mechanical properties of freestanding nanoporous gold structures, Acta Mater. 55 (2007) 4593–4602. https://doi.org/10.1016/j.actamat.2007.03.018.

[5] Y. Sun, S.A. Burger, T.J. Balk, Controlled ligament coarsening in nanoporous gold by annealing in vacuum versus nitrogen, Philos. Mag. 94 (2014) 1001–1011. https://doi.org/10.1080/14786435.2013.876113.

[6] B.A.M. Hodge, J.R. Hayes, J.A. Caro, J. Biener, A. V. Hamza, A.M. Hodge, J.R. Hayes, J.A. Caro, J. Biener, A. V. Hamza, Characterization and Mechanical Behavior of Nanoporous Gold **, Adv. Eng. Mater. 8 (2006) 853–857. https://doi.org/10.1002/adem.200600079.

[7] Y. Ding, Y.J. Kim, J. Erlebacher, Nanoporous gold leaf: "Ancient technology "/advanced material, Adv. Mater. 16 (2004) 1897–1900. https://doi.org/10.1002/ADMA.200400792/FORMAT/PDF.

[8] E.J. Gwak, J.Y. Kim, Weakened Flexural Strength of Nanocrystalline Nanoporous Gold by Grain Refinement, Nano Lett. 16 (2016) 2497–2502. https://doi.org/10.1021/acs.nanolett.6b00062.

[9] C. Suryanarayana, Mechanical alloying and milling, Prog. Mater. Sci. 46 (2001) 1–184. https://doi.org/10.1016/S0079-6425(99)00010-9.

[10] H.M. Rietveld, A profile refinement method for nuclear and magnetic structures, J. Appl. Crystallogr. 2 (1969) 65–71. https://doi.org/10.1107/s0021889869006558.

[11] L. Lutterotti, Total pattern fitting for the combined size-strain-stress-texture determination in thin film diffraction, Nucl. Instruments Methods Phys. Res. Sect. B Beam Interact. with Mater. Atoms. 268 (2010) 334–340. https://doi.org/10.1016/j.nimb.2009.09.053.

[12] Y.H. Tan, J.A. Davis, K. Fujikawa, N.V. Ganesh, A. V. Demchenko, K.J. Stine, Surface area and pore size characteristics of nanoporous gold subjected to thermal, mechanical, or surface modification studied using gas adsorption isotherms, cyclic voltammetry, thermogravimetric analysis, and scanning electron microscopy, J. Mater. Chem. 22 (2012) 6733–6745. https://doi.org/10.1039/c2jm16633j.

[13] H. Jeon, S. Lee, J.Y. Kim, Tension-compression asymmetry in plasticity of nanoporous gold, Acta Mater. 199 (2020) 340–351. https://doi.org/10.1016/j.actamat.2020.08.054.

[14] M. Koifman Khristosov, S. Dishon, I. Noi, A. Katsman, B. Pokroy, Pore and ligament size control, thermal stability and mechanical properties of nanoporous single crystals of gold, Nanoscale. 9 (2017) 14458–14466. https://doi.org/10.1039/c7nr04004k.

[15] C. Lakshmanan, R.N. Viswanath, S.R. Polaki, R. Rajaraman, S. Dash, A.K. Tyagi, Electrochimica Acta Surface area of nanoporous gold : Effect on temperature, Electrochim. Acta. 182 (2015) 565–572. https://doi.org/10.1016/j.electacta.2015.09.104.

[16] Y.K.C.K. Chen-Wiegart, S. Wang, Y.S. Chu, W. Liu, I. McNulty, P.W. Voorhees, D.C. Dunand, Structural evolution of nanoporous gold during thermal coarsening, Acta Mater. 60 (2012) 4972–4981. https://doi.org/10.1016/j.actamat.2012.05.012.

[17] L.H. Qian, X.Q. Yan, T. Fujita, A. Inoue, M.W. Chen, Surface enhanced Raman scattering of nanoporous gold: Smaller pore sizes stronger enhancements, Appl. Phys. Lett. 90 (2007) 153120. https://doi.org/10.1063/1.2722199.

[18] N. Badwe, X. Chen, K. Sieradzki, Mechanical properties of nanoporous gold in tension, Acta Mater. 129 (2017) 251–258. https://doi.org/10.1016/j.actamat.2017.02.040.

[19] J. Schindelin, I. Arganda-Carreras, E. Frise, V. Kaynig, M. Longair, T. Pietzsch, S. Preibisch, C. Rueden, S. Saalfeld, B. Schmid, J.Y. Tinevez, D.J. White, V. Hartenstein, K. Eliceiri, P. Tomancak, A. Cardona, Fiji: An open-source platform for biological-image analysis, Nat. Methods. 9 (2012) 676–682. https://doi.org/10.1038/nmeth.2019.

[20] J. Zeng, F. Zhao, J. Qi, Y. Li, C.H. Li, Y. Yao, T.R. Lee, W.C. Shih, Internal and external morphology-dependent plasmonic resonance in monolithic nanoporous gold nanoparticles, RSC Adv. 4 (2014) 36682–36688. https://doi.org/10.1039/c4ra04922e.

[21] A. Chauvin, L. Molina-Luna, J. Ding, C.H. Choi, P.Y. Tessier, A.A. El Mel, Study of the Coarsening of Nanoporous Gold Nanowires by In Situ Scanning Transmission Electron Microscopy During Annealing, Phys. Status Solidi - Rapid Res. Lett. 13 (2019) 2–7. https://doi.org/10.1002/pssr.201900376.

[22] Y. Ding, J. Erlebacher, Nanoporous metals with controlled multimodal pore size distribution, J. Am. Chem. Soc. 125 (2003) 7772–7773. https://doi.org/10.1021/ja035318g.

[23] A. Wittstock, A. Wichmann, J. Biener, M. Bäumer, Nanoporous gold: A new gold catalyst with tunable properties, Faraday Discuss. 152 (2011) 87–98. https://doi.org/10.1039/c1fd00022e.

[24] K.R. Mangipudi, E. Epler, C.A. Volkert, Morphological similarity and structure-dependent scaling laws of nanoporous gold from different synthesis methods, Acta Mater. 140 (2017) 337–343. https://doi.org/10.1016/j.actamat.2017.08.039.

[25] M. Hakamada, M. Mabuchi, Nanoporous gold prism microassembly through a self-organizing route, Nano Lett. 6 (2006) 882–885. https://doi.org/10.1021/nl0602443.

[26] R.N. Viswanath, V.A. Chirayath, R. Rajaraman, G. Amarendra, C.S. Sundar, Ligament coarsening in nanoporous gold: Insights from positron annihilation study, Appl. Phys. Lett. 102 (2013). https://doi.org/10.1063/1.4812290.

[27] M. Hakamada, M. Mabuchi, Thermal coarsening of nanoporous gold: Melting or recrystallization, J. Mater. Res. 24 (2009) 301–304. https://doi.org/10.1557/jmr.2009.0037.

[28] A.M. Hodge, J. Biener, J.R. Hayes, P.M. Bythrow, C.A. Volkert, A. V. Hamza, Scaling equation for yield strength of nanoporous open-cell foams,

Acta Mater. 55 (2007) 1343–1349. https://doi.org/10.1016/j.actamat.2006.09.038.

[29] L.H. Qian, X.Q. Yan, T. Fujita, A. Inoue, M.W. Chen, Surface enhanced Raman scattering of nanoporous gold: Smaller pore sizes stronger enhancements, Appl. Phys. Lett. 90 (2007) 3–6. https://doi.org/10.1063/1.2722199.

[30] F. Kertis, J. Snyder, L. Govada, S. Khurshid, N. Chayen, J. Erlebacher, Structure/processing relationships in the fabrication of nanoporous gold, JOM. 62 (2010) 50–56. https://doi.org/10.1007/s11837-010-0087-6.

[31] M.A. Meyers, A. Mishra, D.J. Benson, Mechanical properties of nanocrystalline materials, Prog. Mater. Sci. 51 (2006) 427–556. https://doi.org/10.1016/j.pmatsci.2005.08.003.

[32] J. Svoboda, H. Riedel, Quasi-equilibrium sintering for coupled grain-boundary and surface diffusion, Acta Metall. Mater. 43 (1995) 499–506. https://doi.org/10.1016/0956-7151(94)00249-H.

[33] W.D. Kingery, M. Berg, Study of the initial stages of sintering solids by viscous flow, evaporation-condensation, and self-diffusion, J. Appl. Phys. 26 (1955) 1205–1212. https://doi.org/10.1063/1.1721874.

[34] S.H. Hillman, R.M. German, Constant heating rate analysis of simultaneous sintering mechanisms in alumina, J. Mater. Sci. 27 (1992) 2641–2648. https://doi.org/10.1007/BF00540683.

[35] L.C. De Jonghe, M.N. Rahaman, Sintering of Ceramics, in: Handb. Adv. Ceram. Mater. Appl. Process. Prop., Elsevier Inc., 2003: pp. 187–264. https://doi.org/10.1016/B978-012654640-8/50006-7.

Chapter 4

NP Au behavior in methyl-orange solutions

4.1 Introduction

The interest in NP Au for catalytic applications has been introduced in **Chapter 1**. In addition to more studied reactions, a few years ago, Hakamada et al. [1] proposed NP Au monolith as catalyst for methyl orange (MO) degradation in solution. MO is a molecule that belongs to the class of azo dyes (R-N=N-R'); this family of compounds is largely employed in the textile industry because of its intense color and its stability [2]. Moreover, MO has been used also as probe for tests in photocatalytic studies devoted to the degradation of this class of organic dyes, which are pollutants and therefore damage the natural environment. In particular, in the cases of heterogenous semiconductor photocatalysts, the reactions between holes or electrons with water or oxygen form several oxygen-containing species, such as perhydroxyl, superoxide and hydroxyl radicals, which cause the dyes degradation thanks to their high reactivity as oxidizing agents [3–7]

In the present work, we show that in the presence of monolithic NP Au only a partial degradation of MO occurs, whereas most of the dye is adsorbed onto the NP Au surface.

Our study has been carried out by mean of ultraviolet-visible (UV-Vis), energy-dispersive X-ray spectroscopy (EDS) and X-ray photoelectron spectroscopy (XPS) spectroscopies, high-performance liquid chromatography (HPLC), scanning electron microscopy (SEM) and electrochemical impedance spectroscopy (EIS).

4.2 Materials and methods

4.2.1 Materials

Au powders (99.995 %) were purchased from Alfa Aesar, Ag powders (99.9 %) from Aldrich, Nitric Acid (70 %) from BDH, Methyl Orange powders from Acros Organics, Ultrapure water (18.2 MΩ·cm) was produced with a Milli-Q Milllipore water purification system.

4.2.2 NP Au fabrication

The AuAg precursor alloy was prepared by mechanical alloying of Au and Ag powders in atomic proportion 3:7. 2 g of the mixture was put inside a hardened steel vial with two hardened steel spheres of 8 g each. The

powders were milled in a SPEX 8000M ball miller for 16 h. NP Au was prepared by cold-pressing the as-prepared AuAg powders into pellets followed by chemical corrosion in HNO_3 70% for 24 h. After the dealloying, the pellets were washed 5 times with MilliQ water and then dried overnight under vacuum.

4.2.3 UV-Vis measurements

Electronic absorption spectra were recorded with a UV-Vis spectrophotometer Agilent Technologies (Cary Series Spectrophotometer) in a quartz cell of 10 mm of path length.

4.2.4 High-Performance Liquid Chromatography (HPLC)

Solutions were analyzed by a 1260 Infinity II (Agilent Technologies) HPLC system, equipped with a Kinetex (5 µm C18 100 Å, 250 mm x 4.6 mm) column (Phenomenex) and a UV-Vis absorption detector. Analyses were performed at 40 °C under isocratic conditions, with a mobile phase (flow rate 0.8 mL min^{-1}) composed of a mixture (24/76 vol/vol) of acetonitrile and a 10 mM ammonium acetate solution. Absorption at 462 nm was recorded.

4.2.5 SEM/EDS

The precursor and dealloyed materials were investigated by SEM using a Zeiss Merlin microscope, equipped with a Schottky electron source, working with an acceleration voltage of 5 kV at short working distance (high-resolution mode). Secondary electrons (SE) were collected to provide fine details on the surface morphology. SE were gathered using an in-lens detector. SEM-Energy Dispersive Spectroscopy (EDS) measurements were performed by an Oxford silicon drift detector (SDD) with a detection area of 60 mm^2 at an acceleration voltage of 15 kV.

4.2.6 Electrochemical measurements

The NP Au has been characterized by means of electrochemical impedance spectroscopy (EIS) with using a 0.1 M $HClO_4$ solution in a conventional three-electrode cell in which Saturated Calomel Electrode (SCE) was the reference and a platinated titanium net was used as counter electrode. All the EIS measurements were carried out using an AUTOLAB PGSTAT302N (Metrohm, Switzerland) potentiostat/galvanostat equipped with the FRA analyzer and controlled with the NOVA software at the open circuit potential (OCP); the frequency was varied from 63 kHz down to 0.1 Hz with an amplitude of 0.01 Hz.

4.2.7 X-ray Photoelectron Spectroscopy (XPS)

XPS analyses were carried out with a Kratos Axis Ultra^{DLD} spectrometer using a monochromatic Al Kα source operated at 20 mA and 15 kV. Wide scan analyses were carried out with an analysis area of 300 x 700 microns and a pass energy of 160 eV. High resolution analyses were carried out with the same analysis area and a pass energy of 10 eV over the binding energy regions typical for N 1s, Ag 3d, Au 4d, S 2p and Au 4f signals. Spectra were analyzed using CasaXPS software (version 2.3.24).

4.3 Results and discussion

Au in nanoporous form was fabricated by chemical etching of a cold pressed pellet of an Au-Ag alloy using nitric acid at 70% as corrosive agent for 24 h. The starting alloy was obtained by ball milling of gold and silver powders in the atomic ratio of 30:70.

The morphology and the composition of the obtained NP Au were investigated by SEM and EDS measurements, respectively. Fig. 4.1 reports the SEM image of and an EDS spectrum of the examined area. The NP Au shows a bicontinuous structure of interconnected ligaments and pores with a mean ligament diameter around 15 ± 5 nm, whereas the residual Ag atomic content is around 12 %.

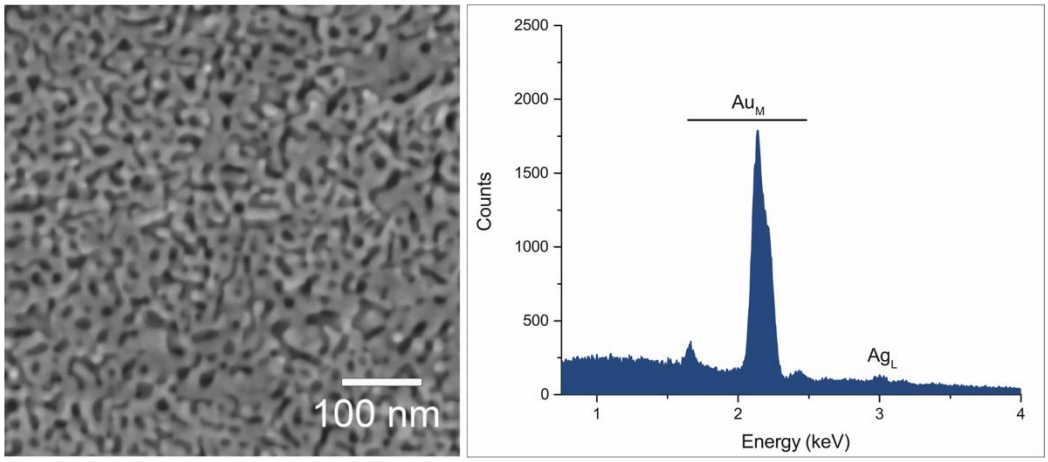

Fig. 4.1 SEM image and EDS spectrum of NP Au after 24h of dealloying

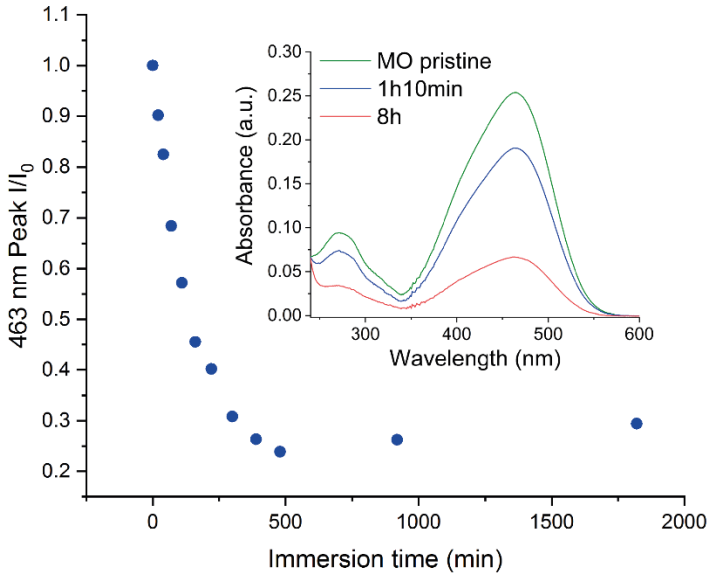

Fig. 4.2 MO discoloration kinetics. The inset shows UV-Vis spectrum of MO before NP Au immersion, 70 min and 8h after the immersion.

In order to investigate the behavior of the NP Au with the MO, a monolith of this material was immersed into an aqueous solution of the dye with a concentration of $2 \cdot 10^{-5}$ M. The trend over time of this system was monitored by UV-Vis spectroscopy measuring the solution absorption spectrum at different time intervals. Fig. 4.2 shows the discoloration kinetics of MO after the immersion of NP Au, calculated by considering the ratio between the intensity of the absorption MO peak around 463 nm after a certain time of

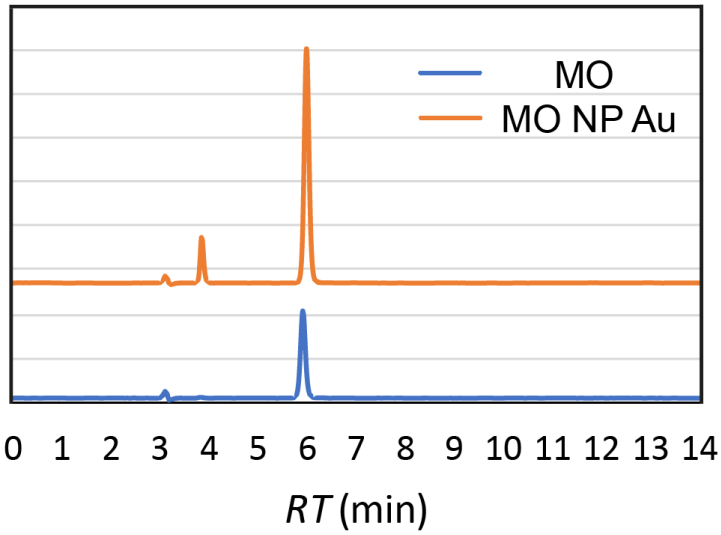

Fig. 4.3 HPLC chromatograms of reference MO solution and of residual solution after NP Au immersion in MO.

immersion and that of pristine MO solution. The peak intensity decreases with time until 8h. Then, it slightly increases before reaching an equilibrium value around 29 % of the initial peak intensity. The discoloration tests were repeated several times and the final I/I_0 ratio ranges between 19 and 29%; these variations are probably due to different surface areas of the NP Au pellets employed in the tests.

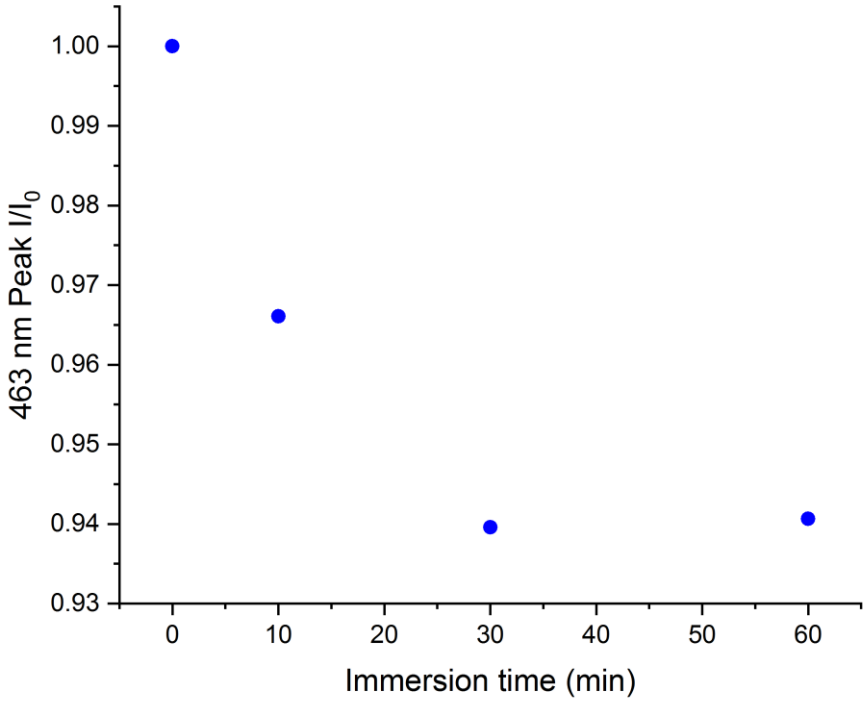

Fig. 4.4 Trend of relative concentration vs immersion time for NP Au pellet dealloyed for 5s in order to obtain a thin nanoporous layer.

The MO solution after 30 h of NP Au pellet immersion was studied by HPLC measurements (see Fig. 4.3). The chromatogram of a reference solution of pure MO shows a peak at ca. 5.9 min. of retention time, whereas that of the residual solution of the above-described discoloration test presents the characteristic peak of MO along with a peak at 3.84 min. However, the small peak at 3.1 min can also be found in the initial MO solution and in MilliQ H_2O, with comparable intensities. These findings suggest that NP Au can cause MO degradation, as reported by Hakamada et al. [1], although only partial, in accordance with the UV-Vis data. Moreover, the calculated MO concentration by HPLC is systematically lower than that calculated from UV-Vis measurements. This feature can be ascribed to the superposition of the absorption peak of MO and that of the degradation product, which could lead to a concentration overestimation with spectroscopic measurements. Since the peak around 463 nm is characteristic of N=N bond, we can

suppose that this bond was not broken in the degradation product, in agreement with the results found for the MO photodegradation in the presence of TiO_2 [4]. Another interesting fact is that only this peak appears in the HPLC chromatograms of different residual MO solutions, suggesting that the degradation process does not continue after the formation of this compound. Meanwhile, from the discoloration kinetics, it seems that also this compound could be adsorbed by NP Au.

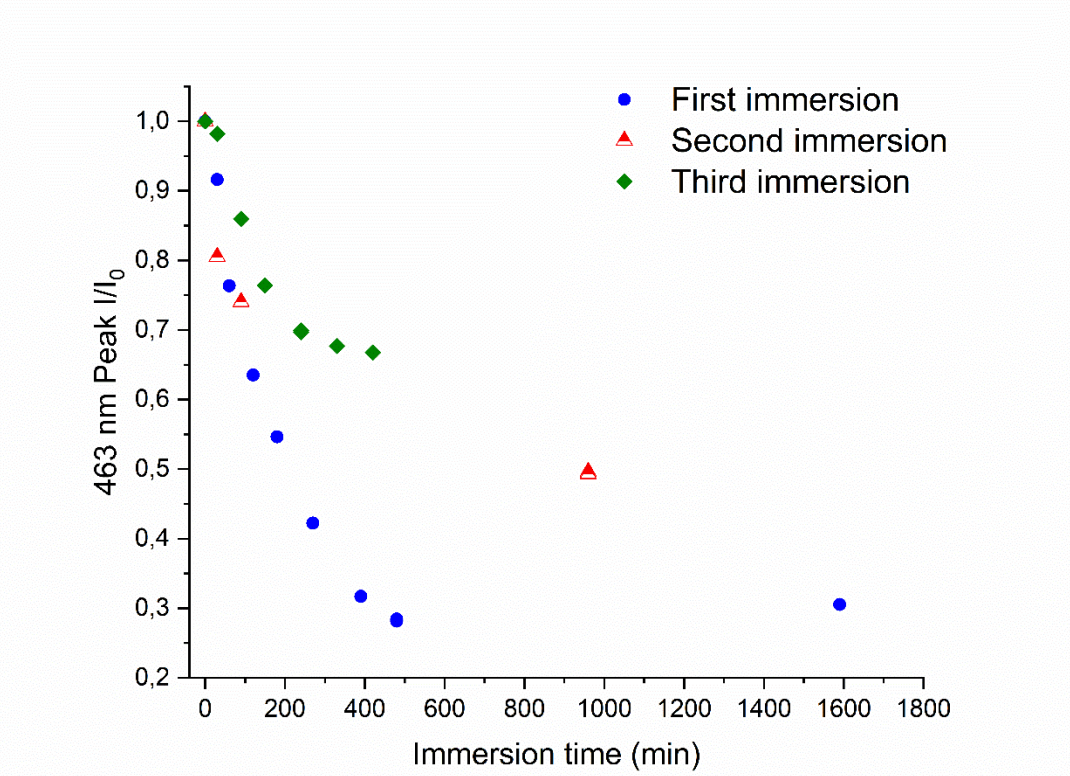

Fig. 4.5 Relative concentration of MO over time for the same sample repeatedly immersed in fresh MO solution.

In order to evaluate the effect of a reduction of the surface area of gold, we prepared a NP Au sample by treating with HNO_3 and just for 5s, only one face of a pellet of AuAg alloy. Since the short time of dealloying induces the formation of only a thin nanoporous layer, an important decrease of the surface area can be expected in comparison with the NP Au obtained with 24 h of leaching on both faces. In Fig. 4.4 is reported the discoloration kinetics when a pellet of NP Au with a thin nanoporous layer was immersed into a solution of MO. It can be observed that the intensity of the peak at 463 nm slightly decreases at the beginning and then reach a plateau at around 94 % of I/I_0. This fact points to a dominant non-catalytic process; indeed, in the case of a prevalent catalytic degradation, we should expect a slower discoloration kinetics (due to a lower active surface area accessible

to the reactant molecules) but not such a dramatic change of the final I/I_0 ratio.

Fig. 4.5 shows instead the discoloration kinetics of MO when an NP Au was repeatedly immersed in fresh solutions at the same concentration. Here, we can see that the plateau level (the final I/I_0 ratio) increases after each immersion, suggesting the presence of equilibrium of absorption. Therefore, to have further adsorption, a higher MO equilibrium concentration is needed when more NP Au adsorption sites are occupied. To investigate in deep the nature of this process, the desorption of MO from NP Au pellet was attempted. When the pellet was immersed in water, no observable MO

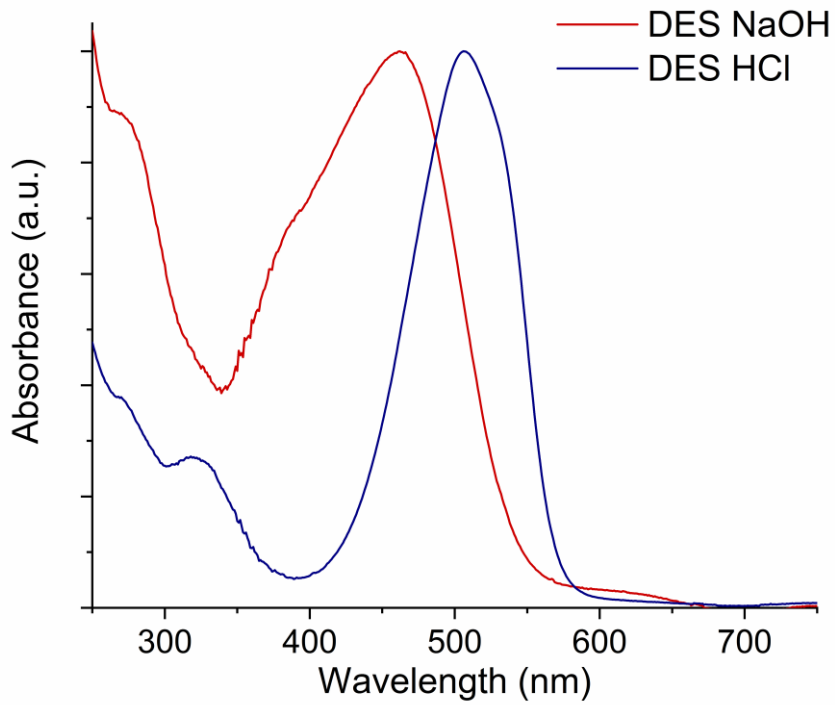

Fig. 4.6 Normalized UV-Vis spectra of solutions desorbed from different NP Au pellets in HCl and NaOH 0.1 M.

desorption was noticed, while when the pellet was immersed either in NaOH or in HCl the solution turned colored. The obtained solutions were analyzed by UV-Vis (see Fig. 4.6) and HPLC measurements, which highlight the presence of MO along with other undefined compounds. In the UV-Vis spectra of Fig. 4.6, the characteristic peak of MO is red-shifted when desorbed in HCl and blue-shifted when desorbed in NaOH. This is a typical behavior of MO, by which is used as a pH indicator: by varying the pH of the solution, the ratio between protonated (red) and deprotonated (yellow) forms of the molecule changes and it involves a change in position and shape of the resulting absorption peak [8]. After the desorption in both solutions, we observed that NP Au pellet does not cause MO discoloration

anymore, also after having neutralized the surface with the HCl and NaOH for the samples treated with NaOH and HCl, respectively. This finding suggests that an irreversible change occurred to the NP Au surface following its contact with the MO solution.

In order to clarify the adsorption-desorption mechanism, we constructed an

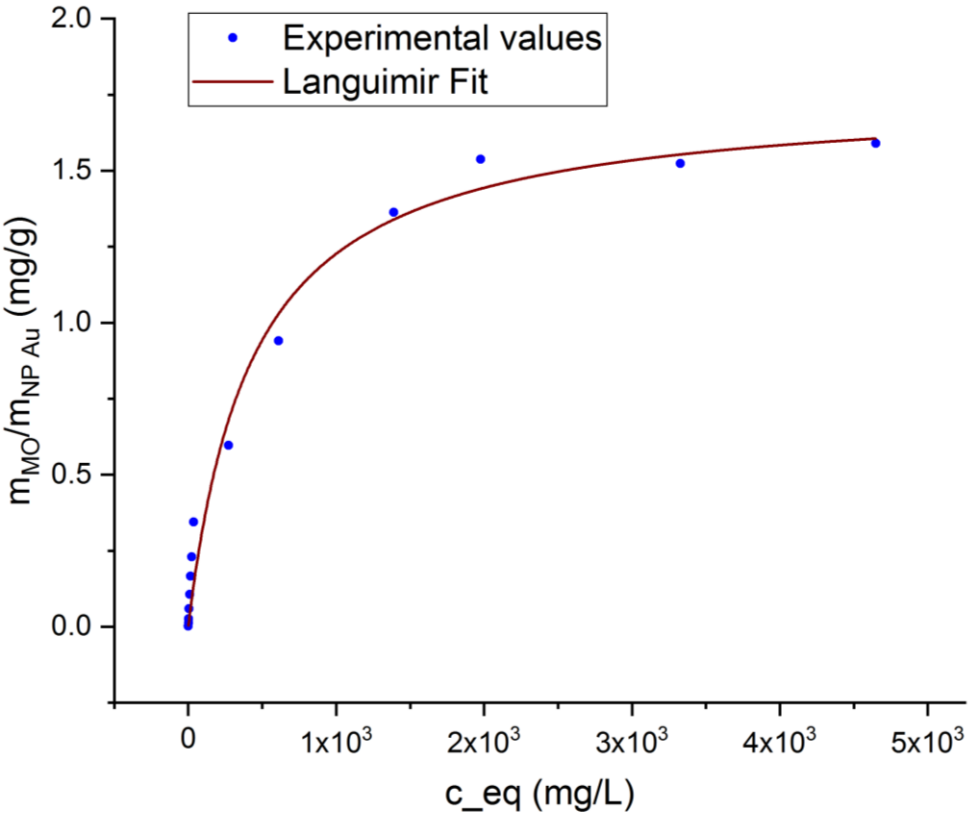

Fig. 4.7 Adsorption isotherm of MO in NP Au pellet.

adsorption isotherm by exposing the same NP Au pellet to gradually higher concentrations of MO solution, from $4 \cdot 10^{-6}$ M to $1.4 \cdot 10^{-2}$ M. The adsorption isotherm is shown in Fig. 4.7 and can be well fitted by the Langmuir adsorption model [9]. The total amount of MO that disappeared from the solutions is around 1.6 mg with a pellet of 230 mg. Moreover, after the complete saturation of the sample, desorption was repeatedly induced by exposing the sample to MO solutions with decreasing concentrations and then to pure water. We estimate that 30 % of MO adsorbed was released. Here we can easily observe from HPLC measurements shown in Fig. 4.8, that, along with the MO, the degradation product found in the residual solutions of adsorption tests, is also present after the desorption. This fact confirms the hypothesis that this compound is also partially adsorbed by NP Au.

Also in this case, a further amount of desorbed material was extracted by immersing the pellet in NaOH 0.1 M, around 5 % of the disappeared MO amount.

It is still difficult to state the percentage of MO adsorbed and that of MO degraded because the amount of degradation product seems to be much lower than the amount of MO disappeared and that was not finally desorbed. Our guess is that MO and the degradation product are not completely desorbed from NP Au surface. With the aim to investigate if the interaction of NP Au with MO causes irreversible changes to the surface and therefore, if whether regeneration of the pellet is possible or not, we performed measurements of XPS and impedance. Electrochemical Impedance Spectroscopy (EIS) proved to be a very useful technique for surface studies and characterizations. NP Au has been analyzed at its original pristine state,

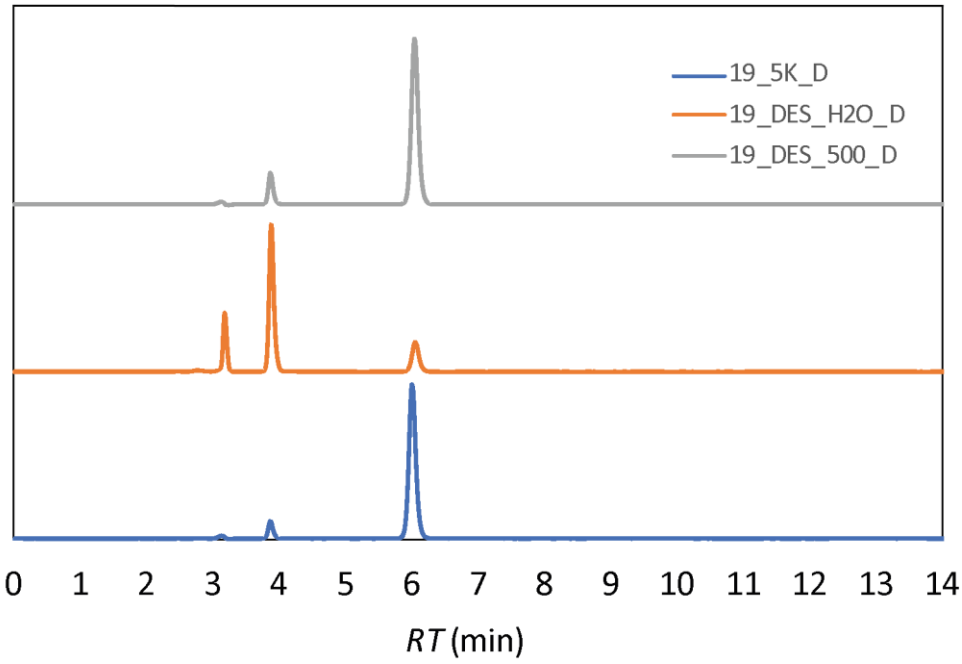

Fig. 4.8 HPLC chromatograms of residual solutions of adsorption and desorption in different concentrations of MO: after adsorption in 10^{-3} M solution (blue), desorption in 10^{-4} M (orange) and desorption in H2O (grey).

after absorption and after the desorption of the dye. Fig. 4.9 reports the Nyquist plot of the analyzed samples, each one rescaled for its own solution resistance (R_S) value. As one can see, the electrochemical response varies significantly in all three situations but, indeed, NP Au after the adsorption differs definitely more than the other two. More in specific, after MO absorption, the NP Au loses part of its capacitive feature for a more resistive response. Then, after the desorption, the material does not regain completely its original behavior. These observations, although qualitative

estimations, can be a hint of not reversible processes that occurs at the surface such as changes in morphology or some species (MO or some degradation products) which, being hardly desorbed, reduces and modify the active surface of the material.

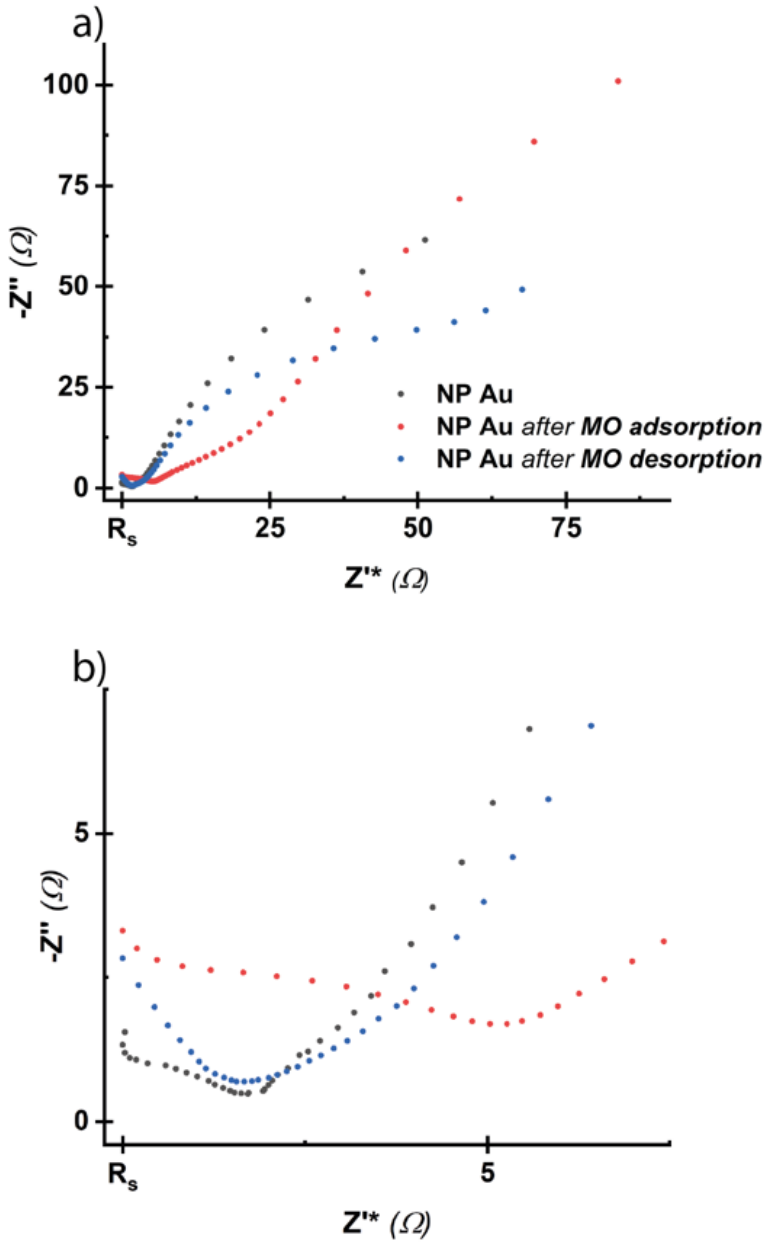

Fig. 4.9 Nyquist plot of NP Au pristine, NP Au after adsorption and NP Au after desorption (a) and magnification on the high-frequency region (b).

Some alternatives for the electrochemical characterization of the surface area of nanoporous gold were explored by Rouya et al [10]. In particular, EIS has been used to calculate the double-layer capacitance and, therefore, the estimation of the surface area. Concerning this method, EIS analysis was conducted at the OCP by using a 0.1 M solution of $HClO_4$, and the

dependence of the imaginary part of the impedance on frequency is reported in Fig. 4.10. In a graph of this kind, a log-log slope of –1 in the medium-to-low frequencies region corresponds to a typical purely capacitive behavior. Since our cases differ from ideality (with log-log slopes ranging from 0.5-0.75), the system should be better described by a constant phase element. Despite the use of this approximation, the slope in the three samples changes in agreement with our previous considerations. Besides,

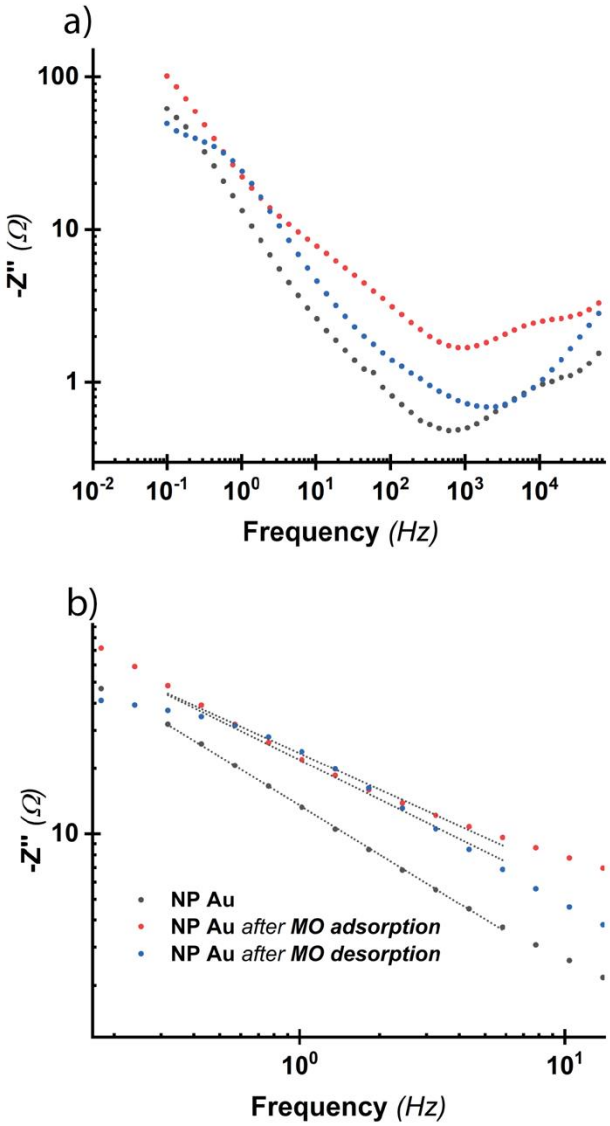

Fig. 4.10 a) Log-log dependance of the imaginary part of the impedance vs frequency. b) Magnitude and fit of the linear part in the medium-to-low frequencies.

the slope changes from -0.75 to -0.55 when the surface is modified with the adsorption of MO, whilst it reaches -0.60 after desorption. As already observed, the not complete desorption of the dye and/or the related surface modifications can be also qualitatively highlighted by the partial recovery of the pristine capacitive behavior.

XPS measurements have also been performed and are reported in Fig. 4.11; the samples NP Au MO 20 mM, NP Au 10 mM and DES NP Au MO 10 mM were washed with distilled water immediately after the immersion. A comparison between the pristine sample and that obtained after the immersion into the MO solution $2 \cdot 10^{-5}$ M does not highlight any important

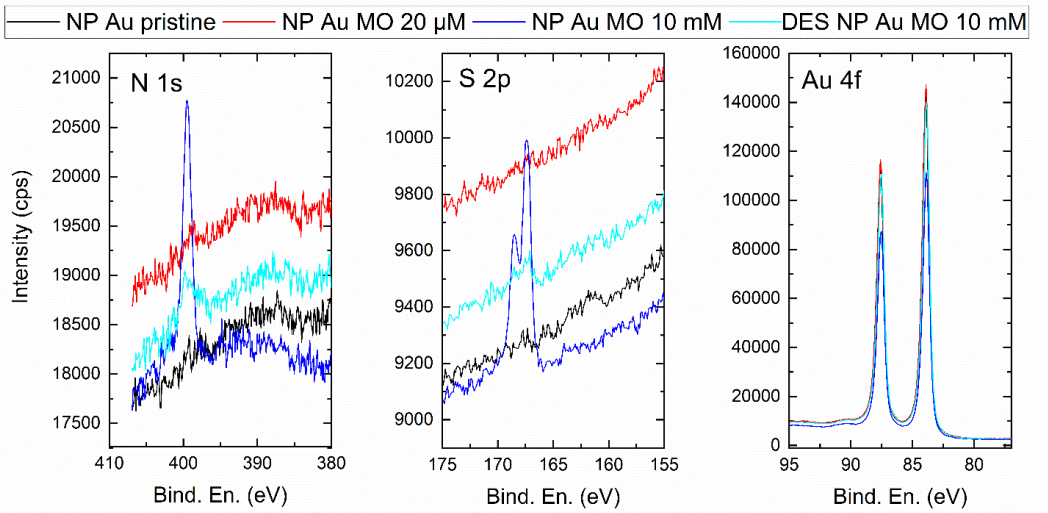

Fig. 4.11 XPS measurements on pristine NP Au and three NP Au immersed in MO solutions. On the left, middle and right are reported the XPS spectra in the regions of N(1s), S(2p) and Au(4f), respectively.

difference. This finding could be related to the low amount of MO adsorbed, which is probably lower than the detection limit of this technique. However, the sample NP Au 10 mM (blue line), which has been immersed into a more concentrated solution, clearly shows the presence on the Au surface of molecules containing N and S. Moreover, the sample DES NP Au MO 10 mM (pale blue line) obtained by immersion in the same solution, and which underwent desorption till the washing solution was colorless, presents the residual presence of the peaks of N and S which can be ascribed to MO and/or its degradation's products adsorbed onto the surface of the NP. It is interesting to note that the peaks corresponding to the 4f gold electrons are not affected by the presence of the molecules absorbed. Indeed, the lack of shift of these peaks was put forward by Hakamada et al. as a proof of the absence of dye molecules in their NP Au sample after immersion into MO solution [1].

4.4 Conclusions

In this chapter, we presented the investigation on the catalytic activity of NP Au in the degradation reactions of MO, a molecule that belongs to the class of azo dyes. Hakamada et al. reported that NP Au is able to catalyze the complete degradation of MO [1]. Our experiments instead show that the degradation of the dye occurs only partially and that an important part of

MO is adsorbed onto the large surface of the NP material. Indeed, UV-Vis measurements on the solutions obtained from the tests of desorption, show that MO, along with (probably MO degradation product), is released in a large amount by the NP Au. Moreover, these findings are also in agreement with the HPLC measurements which proved that MO with another molecule are present in the same solutions. Furthermore, EIS measurements suggested that the surface of NP Au was modified by the immersion into the MO solution and that, even after a prolonged desorption, it did not recover the pristine conditions. XPS analysis showed the presence of molecules with N and S atoms on the surface of NP Au both after the immersion and after the desorption procedures, in agreement with the EIS measurements.

References

[1] M. Hakamada, F. Hirashima, M. Mabuchi, Catalytic decoloration of methyl orange solution by nanoporous metals, Catal. Sci. Technol. 2 (2012) 1814–1817. https://doi.org/10.1039/c2cy20218b.

[2] H. Langhals, Color Chemistry. Synthesis, Properties and Applications of Organic Dyes and Pigments. 3rd revised edition. By Heinrich Zollinger., Angew. Chemie Int. Ed. 43 (2004) 5291–5292. https://doi.org/10.1002/anie.200385122.

[3] M.R. Hoffmann, S.T. Martin, W. Choi, D.W. Bahnemann, Environmental Applications of Semiconductor Photocatalysis, Chem. Rev. 95 (1995) 69–96. https://doi.org/10.1021/cr00033a004.

[4] C. Baiocchi, M.C. Brussino, E. Pramauro, A.B. Prevot, L. Palmisano, G. Marcí, Characterization of methyl orange and its photocatalytic degradation products by HPLC/UV-VIS diode array and atmospheric pressure ionization quadrupole ion trap mass spectrometry, Int. J. Mass Spectrom. 214 (2002) 247–256. https://doi.org/10.1016/S1387-3806(01)00590-5.

[5] I.M. Arabatzis, T. Stergiopoulos, D. Andreeva, S. Kitova, S.G. Neophytides, P. Falaras, Characterization and photocatalytic activity of Au/TiO2 thin films for azo-dye degradation, J. Catal. 220 (2003) 127–135. https://doi.org/10.1016/S0021-9517(03)00241-0.

[6] C.W. Yen, M.A. Mahmoud, M.A. El-Sayed, Photocatalysis in gold nanocage nanoreactors, J. Phys. Chem. A. 113 (2009) 4340–4345. https://doi.org/10.1021/jp811014u.

[7] E. Rouya, S. Cattarin, M.L. Reed, R.G. Kelly, G. Zangari, Electrochemical Characterization of the Surface Area of Nanoporous Gold Films, J. Electrochem. Soc. 159 (2012) K97–K102. https://doi.org/10.1149/2.097204jes.

[8] J. Barbosa, INDICATORS | Acid–Base, Encycl. Anal. Sci. Second Ed. (2005) 360–371. https://doi.org/10.1016/B0-12-369397-7/00270-3.

[9] J. Wang, X. Guo, Adsorption isotherm models: Classification, physical meaning, application and solving method, Chemosphere. 258 (2020) 127279. https://doi.org/10.1016/j.chemosphere.2020.127279.

[10] E. Rouya, S. Cattarin, M.L. Reed, R.G. Kelly, G. Zangari, Electrochemical Characterization of the Surface Area of Nanoporous Gold Films, J. Electrochem. Soc. 159 (2012) K97–K102. https://doi.org/10.1149/2.097204JES/XML.

Chapter 5

NP Au/perovskite nanocrystals heterojunctions

5.1 Introduction

Metal halide perovskites, both organic and inorganic, have attracted extraordinary interest showing high potential for several applications thanks to their excellent optical and electronic properties. Photovoltaic, light-emitting diodes, and other optoelectronic devices [1–4] are technological sectors in which they have taken a dominant position. Moreover, they involve the use of non – polar organic solvents, and they can be processable in solution, showing big potential for efficient and low–cost devices [5]. In this framework, perovskite quantum dot (QD) devices are particularly interesting for their high absorption coefficient, good carrier mobility, flexibility, and broad band-gap tuning by changing QD size and shape. Despite all these promising characteristics, the efficiency of QD devices is far from the theoretically predicted values, probably due to poor charge transfer at the interfaces [6,7]. Further, the poor stability hampers commercial applications of the devices, being them sensitive to heat, light, and environmental stresses [8–11]. In photocatalysis and photovoltaic, for example, the performance of the devices depends on their charge separation ability and the implementation of good nanocrystals (NCs) – electrode interfaces. The development of NCs – metal heterostructures can help to improve both factors and provide new functionalities to the nanostructures, altering the optical properties of semiconductors, notably with photoluminescence quenching or enhancement [12–14]. Noble metals are widely used for their intrinsic capacity to accept electrons, fast capturing the photogenerated electrons at the semiconductor surface, promoting the charge separation and the reduction processes. The presence of metal is also known to induce plasmonic field effects in semiconductor nanostructures, influencing their photocatalytic and photovoltaic performances [15,16]. Several works have been focused on studying the optical properties of lead halide perovskites – Au nanocomposites and their application in photocatalysis and photovoltaic [17–19]. In this framework, NP Au represents an ideal substrate for the growth or deposition of NCs. For these reasons, this chapter shows the possibility to develop a $CsPbBr_3$ – NP Au nanoporous heterostructure (hereafter NCs@NP Au). Indeed, two different approaches were developed and studied to obtain the NCs – Au system, and the optical and structural properties are reported. By analyzing the effect on CsPbBr3 optical properties influenced by the presence of gold, we evidence the efficient charge transfer process in NCs@NP Au

investigating the possible mechanisms of the formation of the heterostructures.

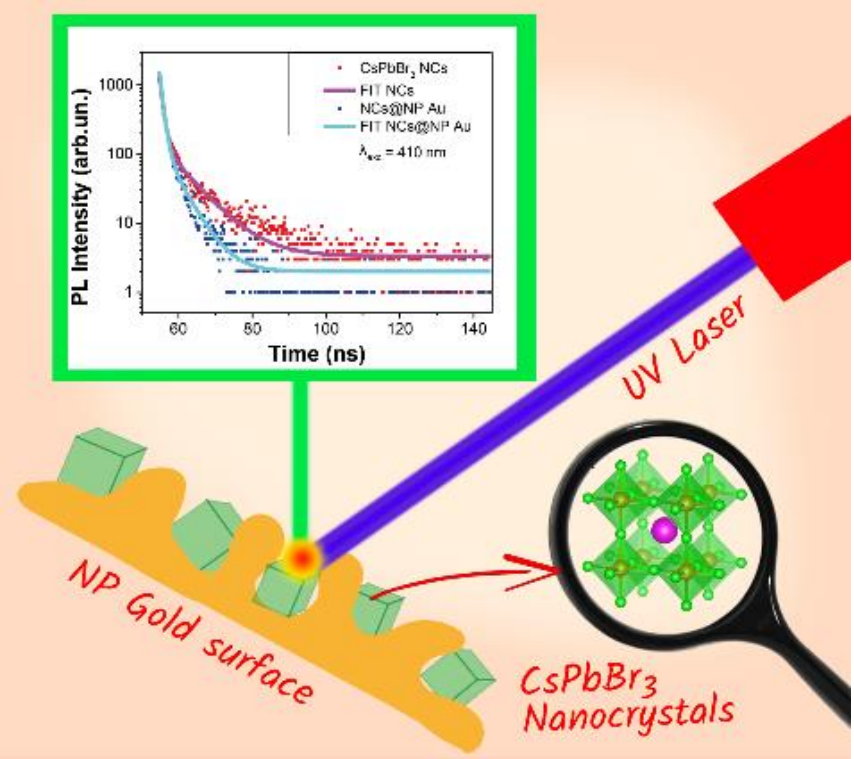

5.2 Materials and methods

5.2.1 Materials

Caesium carbonate (Cs_2CO_3; Aldrich, CAS No. 534-17-8), Octanoic acid (OTAc; Aldrich, CAS No. 124-07-2), Lead bromide ($PbBr_2$; Aldrich, CAS No. 10031-22-8), Tetraoctylammonium bromide (TOAB; Aldrich, CASNo. 14866-33-2), Didodecyldimethylammonium bromide (DDAB; Aldrich, CAS No. 3282-73-3). Toluene, Ethyl acetate, and n-Hexane were of analytical grade. All chemicals were used without any further purification. Au powders (99.995 %, Alfa Aesar, CAS No. 7440-57-5), Ag powders (99.9 %, Aldrich, CAS No. 7440-22-4), Nitric acid (HNO_3 70%, BDH, CAS No. 7697-37-2). Ultrapure water (18.2 MΩ·cm) was produced with a Milli-Q Millipore water purification system.

5.2.2 Synthesis and purification of CsPbBr3 NCs

Synthesis and purification of $CsPbBr_3$ NCs were performed based on previous records [20]. First, caesium precursor was prepared by loading 1

mmol of Cs_2CO_3 and 10 mL of OTAc into a 20 mL vial, and the mixture was stirred for 10 min at room temperature. The $PbBr_2$ precursor solution was prepared by dissolving 1 mmol of $PbBr_2$ and 2 mmol of TOAB in 10 mL of toluene. For the synthesis of $CsPbBr_3$ QDs, 1.0 mL of a cesium precursor solution was swiftly added into 9 mL of a $PbBr_2$–toluene solution into a conical flask. The reaction was magnetically stirred for 5 min at room temperature in open air. Subsequently, 3 mL of DDAB (in toluene 10 mg mL^{-1}) solution was added. After 2 min, ethyl acetate was added into the crude solution with a volume ratio of 2:1; the precipitate was collected separately after centrifugation and dispersed in toluene. The extra ethyl acetate was added into the toluene dispersion, and the precipitate was collected and re-dispersed in n-hexane.

5.2.3 NP Au fabrication

Precursor alloy fabrication

Au and Ag powders were mixed in a ratio 30:70. 2 g of the mixture were ball milled in a SPEX 8000M Mixer/Mill ball mill for 16 hours in a hardened steel vial with two hardened steel spheres of 8 g each. The powders were homogenized every 30 min in the first 2 hours and then every 5 hours.

Dealloying of AuAg alloy

NP Au powders were prepared by chemical dealloying in HNO_3 70 % for 24 h [21,22]. The powders were then washed in MilliQ water 5 times and then dried under vacuum.

5.2.4 Synthesis and purification of CsPbBr3–Au hybrid structure

$CsPbBr_3$ – Au hybrid structures were prepared following two different procedures.

In **procedure 1**, 70 mg of NP Au were just added into the $CsPbBr_3$ NCs (2 mg/mL) dispersed in hexane (3 ml) under ambient conditions. After stirring for 4 h, the powder was filtered and washed several times with hexane under vacuum and then dried overnight.

In **procedure 2**, the synthesis of $CsPbBr_3$ QDs was repeated in presence of NP Au. NP Au (140 mg) was added to the $PbBr_2$ precursor solution, then the synthesis proceeded identically. The hexane dispersion was filtered and washed several times with hexane under vacuum, to separate the nanocrystals not linked to gold, and then dried overnight.

5.2.5 X-Ray Diffraction

X-Ray Diffraction measurements were performed with a Bruker D8 Advance diffractometer operating at 30 kV and 20 mA, equipped with a Cu tube (λ = 1.5418 Å) and a Vantec-1 PSD detector. The powder patterns were recorded in the 10° ≤ 2θ ≤ 70° range.

5.2.6 Raman Spectroscopy

Raman measurements were collected using MS750 spectrograph (sol-instruments) equipped with 600 gr/mm grating. The laser beam (785 nm) was focalized through an Olympus objective (10x), with a laser power of about 7.5 mW. Measurements were performed at room temperature, with a spectral resolution of 1 cm^{-1}.

5.2.7 Time-Resolved Photoluminescence

Time-resolved photoluminescence (TR-PL) measurements were recorded by exciting the samples with 200 fs pulses sourced from an optical parametric amplifier (Light Conversion TOPAS-C) pumped by a regenerative Ti:Sapphire amplifier (Coherent Libra-HE). The repetition frequency was 1 kHz and the TR-PL signal was recorded by a streak camera (Hamamatsu C10910) equipped with a grating spectrometer (Princeton Instruments Acton Spectra Pro SP-2300). All the measurements were collected in the front-face configuration to reduce inner filter effects. Proper emission filters were applied to remove the reflected contribution of the excitation light.

5.2.8 Scanning Electron Microscopy

Scanning Electron Microscopy (SEM) for NP Au was performed with a FEI Quanta Field Emission Electron Microscope, equipped with an Everhart-Thornley secondary electron detector. Imaging was performed at an operating voltage of 20 kV at 10 mm from the examined samples.

SEM studies for heterostructures were carried out using a Carl ZEISS Auriga microscope equipped with an energy-dispersive X-ray spectroscopy (EDX) detector or an ESEM FEI Quanta 200 microscope operating at 25 kV.

5.3 Results and discussion

SEM image of the as-prepared NP Au is shown in Fig. 5.1. NP Au shows a fine nanoporous structure with ligaments and pores diameters around 20 nm.

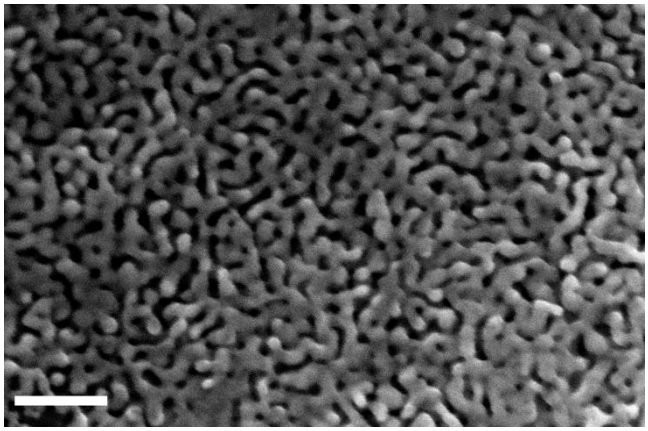

Fig. 5.1 SEM image of NP Au.

$CsPbBr_3$ nanocrystals were synthesized following a room temperature procedure, adopted in previous reports with QDs crystal size of about 10 nm, with a uniform and cubic morphology [20]. X-ray diffraction measurements were performed on nanocrystals precipitate. Fig. 5.2 reports

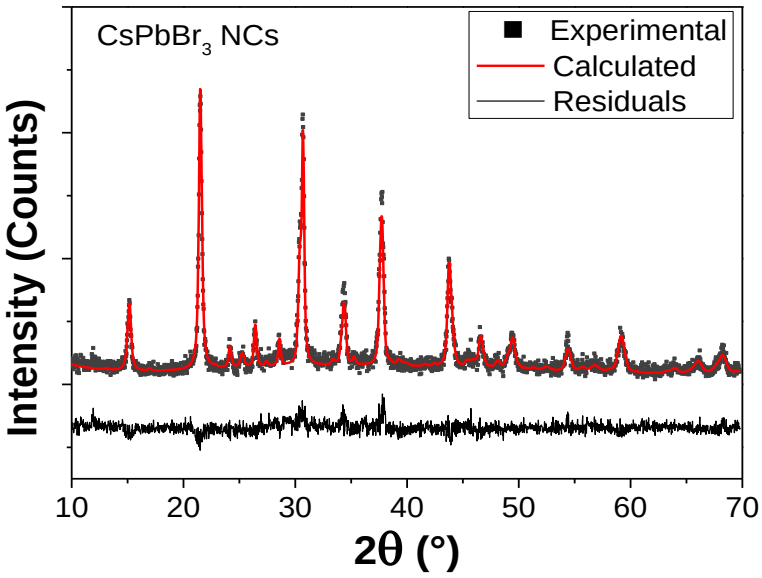

Fig. 5.2 Rietveld refinement of the nanocrystals precipitate. n refers to the Experimental pattern, red line is the pattern calculated by Rietveld refinement, in black line the residuals between the experimental and calculated pattern.

the Rietveld refinement of the pattern, obtained by using the software MAUD [23]. $CsPbBr_3$ NCs are in the orthorhombic g-phase (Pbnm, space group No. 62, COD ID 1533062), with lattice parameters a = 8.219 Å, b = 8.254 Å and c = 11.753 Å.

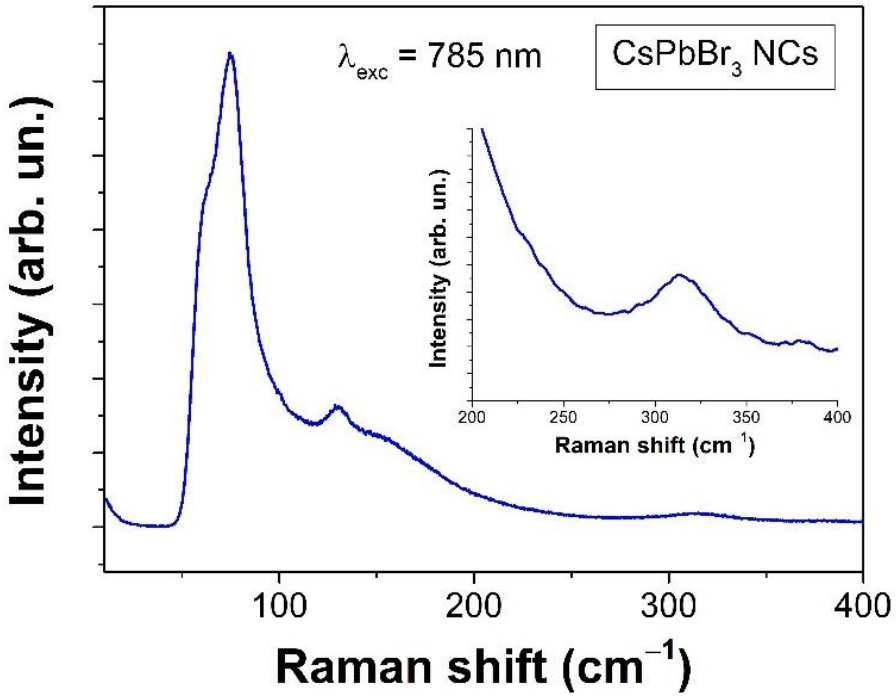

Fig. 5.3 Raman spectrum of nanocrystals precipitate; in the inset a zoom of the region 200 – 400 cm^{-1}. λ_{exc} = 785 nm.

In Fig. 5.3 the Raman spectrum of the nanocrystals precipitate is shown; in the inset the enlarged view of the region 200 – 400 cm^{-1}. The Raman features confirm that $CsPbBr_3$ NCs are in the orthorhombic g-phase, with an intense peak in the region 60 – 80 cm^{-1}, a low-intensity peak around 130 cm^{-1}, and a broad second-order peak around 310 cm^{-1} [24,25].

Fig. 5.4 presents the absorption and emission spectra of colloidal $CsPbBr_3$ dispersed in hexane. The NCs show bright photoluminescence with an emission maximum at 518 nm.

The synthesis of NCs@NP Au followed two different procedures (detailed conditions are reported in paragraph 5.2.4. In procedure **1**, a known amount of NP Au (70 mg) was incorporated into the hexane suspension of $CsPbBr_3$ NCs under ambient conditions. The concentration of the $CsPbBr_3$ NCs was 2 mg/ml. Fig. 5.5 shows the pictures of the solution under UV light (375 nm), before and after the addition of NP Au.

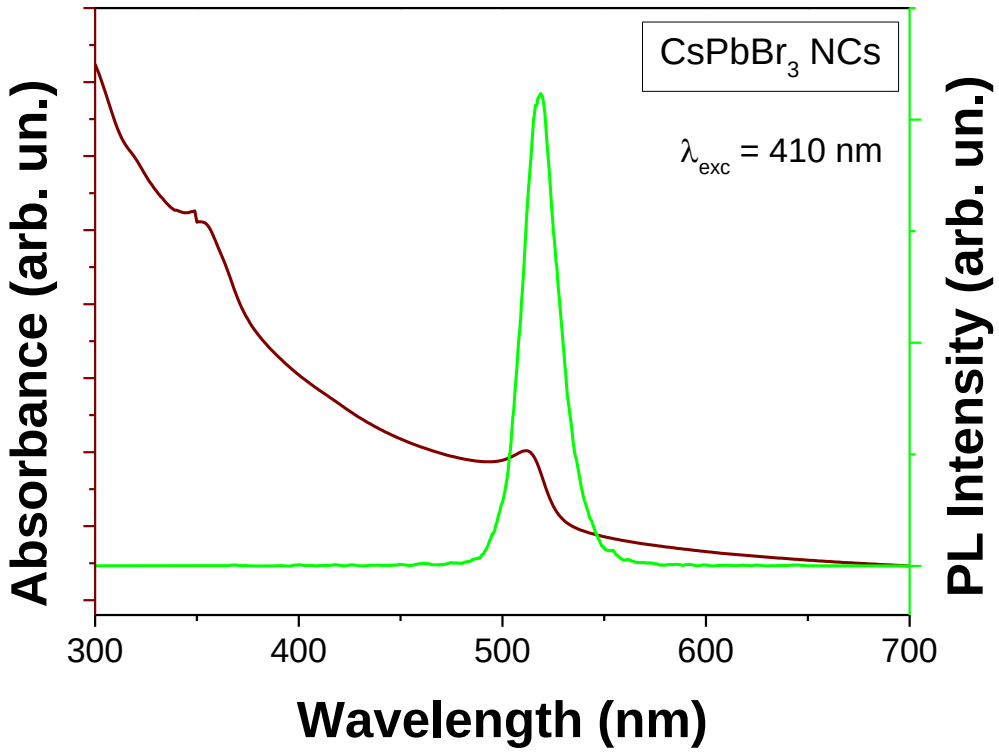

Fig. 5.4 Absorption (brown) and emission (green) spectra of colloidal $CsPbBr_3$ NCs; λ_{exc} = 410 nm.

The solution turns to be colorless with a drastic quenching of the fluorescence. Raman measurements (Fig. 5.6) show the presence of two peaks (135 and 176 cm^{-1}), which cannot be assigned but are in the range of Cs – Pb – Br vibrations [24,26,27]. This can be attributed to the instability of NCs in presence of gold.

The capping agent (namely, DDAB) is formed by the alkyl chain terminating with Nitrogen and methyl groups, respectively. It is widely accepted the strong affinity of the Au surface with ammonium surfactants, and the capping agent likely leaves the nanoparticles to deposit on the Au nanostructures [28–30].

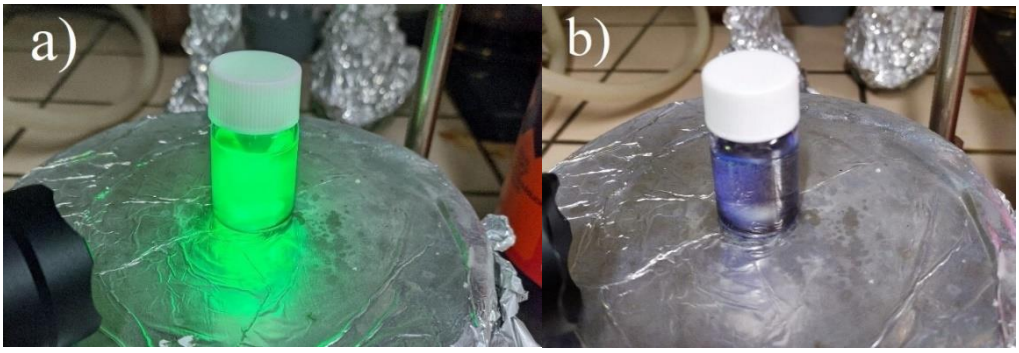

Fig. 5.5 Photographs under UV light (375 nm) of CsPbBr3 NCs dispersion a) before and b) after the introduction of nanoporous gold.

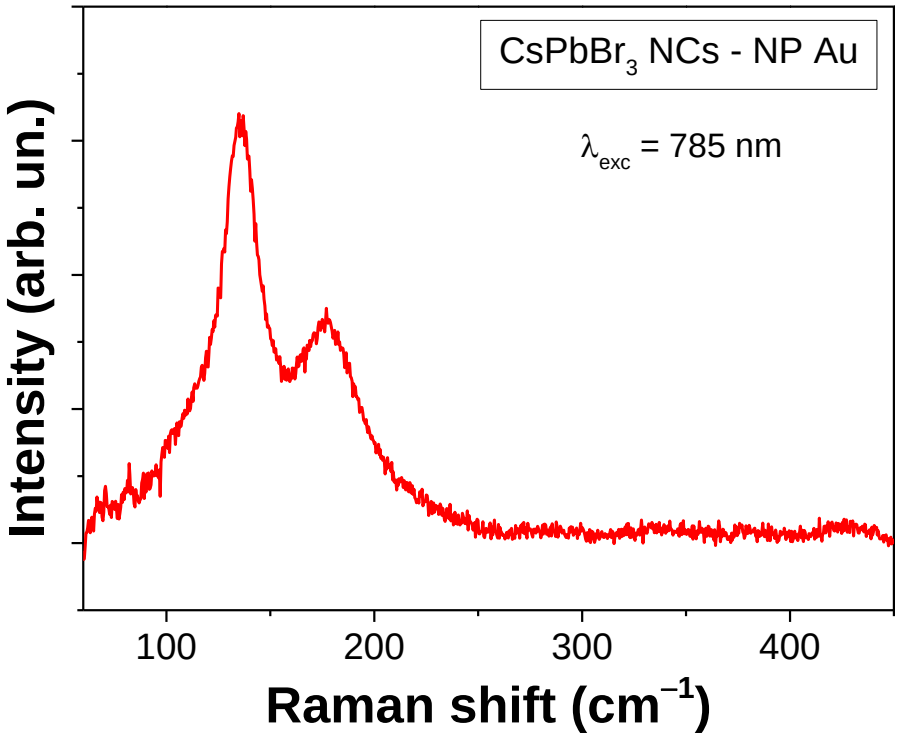

Fig. 5.6 Raman spectrum of NP Au soaked with $CsPbBr_3$ NCs.

We argue that NP Au possesses a good affinity with the capping agent of $CsPbBr_3$ NCs. Stripped of all protection, NCs are no longer stable in hexane and degrade in different stoichiometric phases, as observed in the Raman spectra. To further confirm the hypothesis, the Au nanostructures were covered with the same capping agent and successively added to the $CsPbBr_3$ NCs hexane solution. No interaction between $CsPbBr_3$ NCs and Au nanostructures was observed in this case, the perovskites maintain the structural stability and their characteristic optical properties.

In order to further confirm the hypothesis of the degradation, we performed the elemental analysis on different points of the surface of the sample obtained with **procedure 1**, by means of SEM – EDX measurements. Paying attention to Cs, Pb, and Br, we evidenced the presence of lead or cesium, or both of them, with the disappearance of bromine. This difference in the stoichiometry from the starting $CsPbBr_3$ NCs confirms the absence of perovskites and the formation of amorphous Cs – Pb compounds.

In **procedure 2**, nanoporous gold was added during the synthesis of $CsPbBr_3$ nanocrystals, then the synthesis proceeded as mentioned in paragraph 5.2.4.

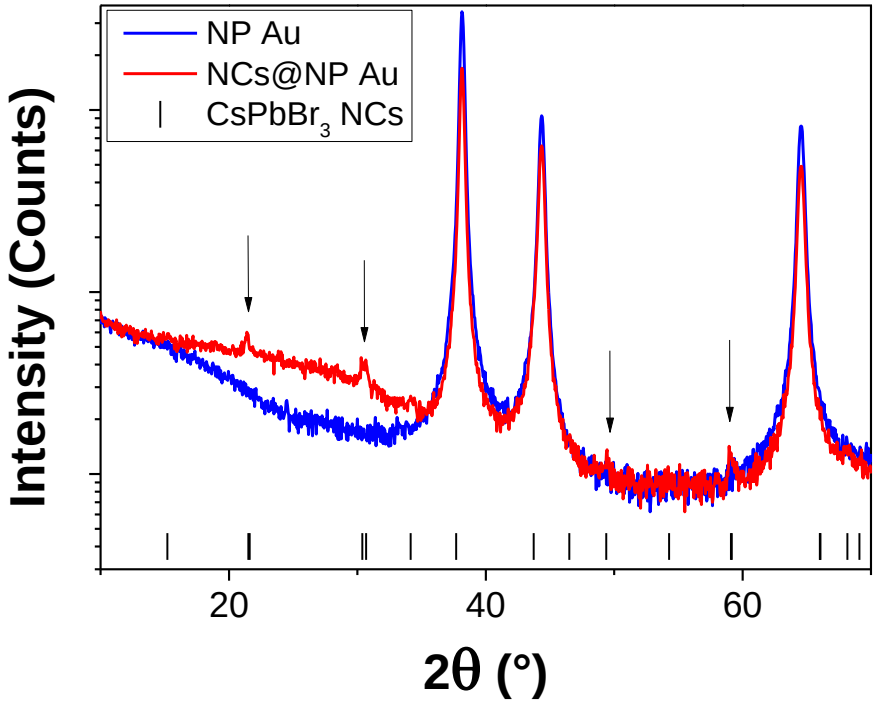

Fig. 5.7 XRD pattern of the sample of pure NP Au (blue) and NCs@NP Au heterostructure (red). The vertical bar individuates the main peaks of pure $CSPbBr_3$ NCs.

Fig. 5.7 reports the XRD pattern of the as-synthesized sample, compared to pure NP Au. It's possible to notice the presence of additional peaks (at 21.5°, 31.5°, 49.4°, and 59.1°), pertaining to pure $CsPbBr_3$ NCs (Rietveld refinement in Fig. 5.2).

Fig. 5.8 shows the steady-state luminescence spectrum of NCs@NP Au heterostructure compared to the emission of the pure $CsPbBr_3$ NCs. The curves have been fitted with a Pseudo-Voigt function, a combination of Gaussian and Lorentzian profiles:

$$I = I_0 + A\left[\mu\frac{2}{\pi}\frac{w}{4(x-x_c)^2+w^2} + (1-\mu)\frac{\sqrt{4\ln(2)}}{\sqrt{\pi}w}e^{-\frac{4\ln(2)}{w^2}(x-x_c)^2}\right] \quad \text{Eq. 5-1}$$

where μ represents the Lorentzian character of the Voigt profile, w is the width parameter of the function and x_c the energy peak center. A slight red shift and a small line broadening are observed. Derived parameters are reported in Table 5.1.

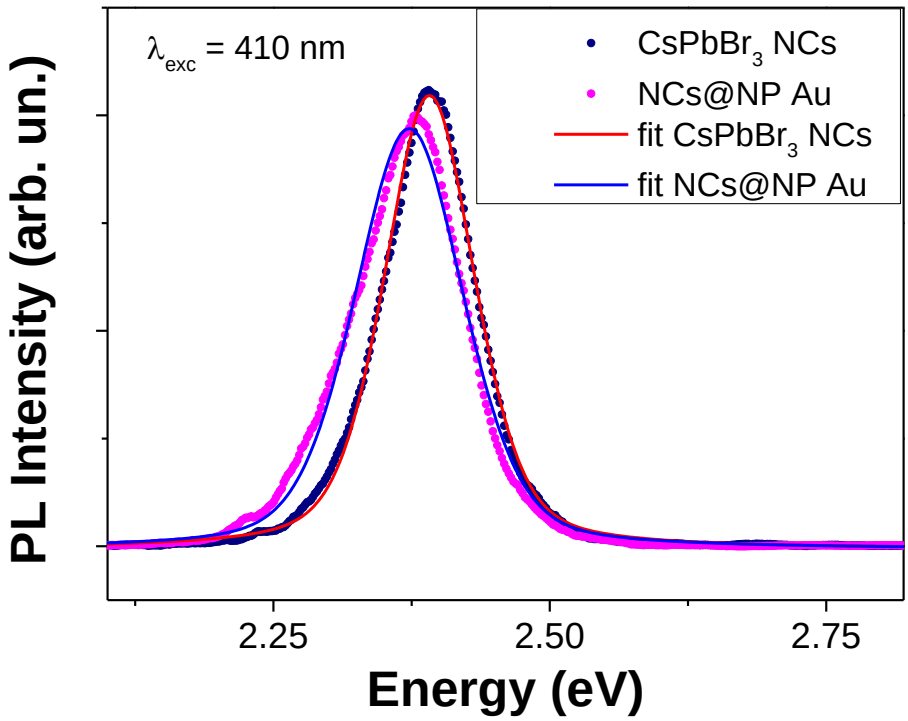

Fig. 5.8 Steady-state luminescence spectra of pure $CsPbBr_3$ NCs and NCs – Au hybrid structure; λ_{exc} = 410 nm.

Table 5.1 Fit parameters of PL measurements on pure $CsPbBr_3$ NCs and NCs – Au hybrid structure.

	x_c (eV)	w (eV)	m
$CsPbBr_3$ NCs	2.39	0.097	0.48
NCs@NP Au	2.37	0.117	0.41

Time-resolved photoluminescence measurements (reported in Fig. 5.9) performed on the samples give more insight into the properties of the recombination mechanism. The curves have been fitted with a biexponential decay function:

$$I(t) = I_0 + \sum_{i=1}^{2} A_i e^{-(t-t_0)/\tau_i} \qquad \text{Eq. 5-2}$$

with $I(t)$ time-dependent PL intensity, I_0 initial PL intensity, A_i amplitude, t time, t_0 initial time, t_i the characteristic lifetime. Table 5.2 retrieves the fitting parameters, which are in accord with previous results [20,31,32]. The average lifetime has been calculated using the following relation [33]:

$$\bar{\tau} = \frac{\sum_i A_i \cdot \tau_i^2}{\sum_i A_i \cdot \tau_i} \qquad \textit{Eq. 5-3}$$

The average lifetime decreases from 3.6 ns to 1.9 ns, showing the interaction between $CsPbBr_3$ NCs and nanoporous gold matrix evidenced by the shortening of the average lifetime with respect to the $CsPbBr_3$ NCs. Indeed, it strongly suggests the presence of non-radiative recombination path and the formation of NCs – NP Au hybrid structure. The transfer efficiency can be calculated by the relation:

$$\eta = 1 - \frac{\tau}{\tau_0} \qquad \textit{Eq. 5-4}$$

Where t_0 is the average lifetime in pure $CsPbBr_3$ NCs and t the average lifetime in presence of gold. The calculated charge transfer efficiency is around 47%.

Table 5.2 Fit parameters of TR – photoluminescence measurements.

	$\bar{\tau}$ (ns)	A_1	t_1 (ns)	A_2	t_2 (ns)
$CsPbBr_3$ NCs	**3.6**	1445.2	0.89	144.02	7.0
NCs@NP Au	**1.9**	1760.9	0.87	140.7	4.4

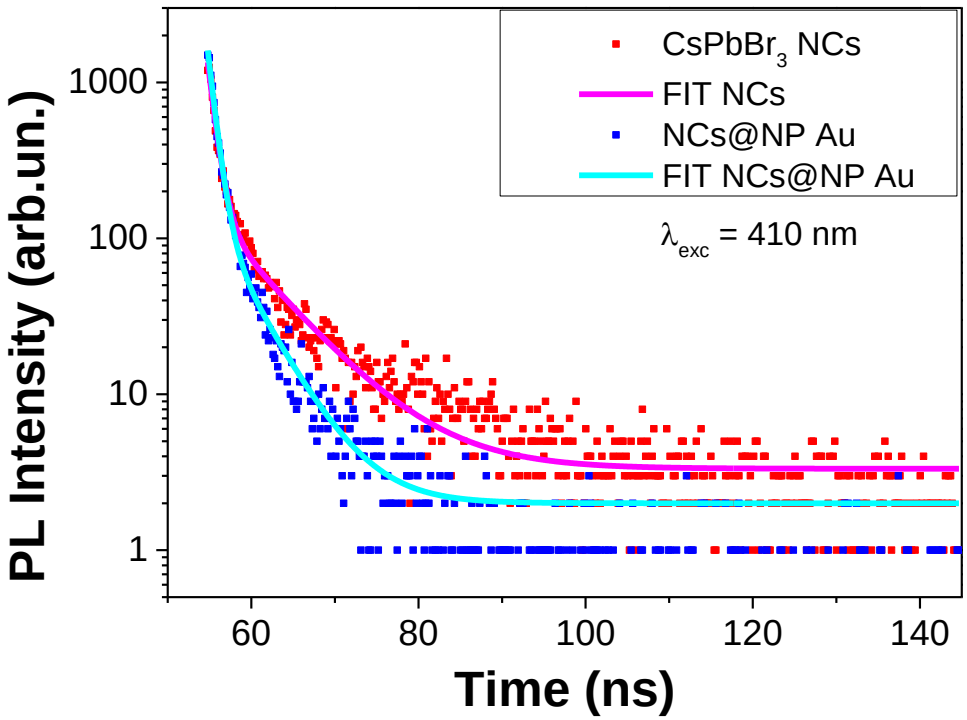

Fig. 5.9 Time-resolved photoluminescence measurement on pure $CsPbBr_3$ NCs and NCs – Au hybrid structure; λ_{exc} = 410 nm.

5.4 Conclusions

To summarize, the goal of this work was to realize a $CsPbBr_3$ – Au heterostructure. By one approach, $CsPbBr_3$ NCs dispersed in hexane were mixed with nanoporous gold. The result is the disappearance of the luminescence, whose cause is assumed to be the degradation of NCs and the subsequent formation of amorphous compounds. The second approach involves the synthesis of NCs directly on the NP Au surface. In this case, it's possible to notice a blue shift in the emission spectrum and a faster decay. Such behavior can be attributed to the achievement of a nanostructure of $CsPbBr_3$ NCs and NP Au, with an efficient charge transfer. The result shows high potential application in all the applications where an efficient charge transfer is required. Further, the possibility to utilize the NCs perovskite as efficient sensitizers strongly suggests the possibility to achieve a tunable photocatalytic device active in all the visible range. In this regard, further specific measurements need to be performed.

References

[1] B. Jeong, H. Han, Y.J. Choi, S.H. Cho, E.H. Kim, S.W. Lee, J.S. Kim, C. Park, D. Kim, C. Park, All-Inorganic CsPbI3 Perovskite Phase-Stabilized by Poly(ethylene oxide) for Red-Light-Emitting Diodes, Adv. Funct. Mater. 28 (2018) 1706401. https://doi.org/10.1002/adfm.201706401.

[2] R.J. Sutton, G.E. Eperon, L. Miranda, E.S. Parrott, B.A. Kamino, J.B. Patel, M.T. Hörantner, M.B. Johnston, A.A. Haghighirad, D.T. Moore, H.J. Snaith, Bandgap-Tunable Cesium Lead Halide Perovskites with High Thermal Stability for Efficient Solar Cells, Adv. Energy Mater. 6 (2016) 1502458. https://doi.org/10.1002/aenm.201502458.

[3] J. Deng, J. Li, Z. Yang, M. Wang, All-inorganic lead halide perovskites: A promising choice for photovoltaics and detectors, J. Mater. Chem. C. 7 (2019) 12415–12440. https://doi.org/10.1039/c9tc04164h.

[4] M. Maqbool, G. Rehman, L. Ali, M. Shafiq, R. Iqbal, R. Ahmad, T. Khan, S. Jalali-Asadabadi, M. Maqbool, I. Ahmad, Structural, electronic and optical properties of CsPbX3(X=Cl, Br, I) for energy storage and hybrid solar cell applications, J. Alloys Compd. 705 (2017) 828–839. https://doi.org/10.1016/j.jallcom.2017.02.147.

[5] D. Chen, X. Chen, Luminescent perovskite quantum dots: synthesis, microstructures, optical properties and applications, J. Mater. Chem. C. 7 (2019) 1413–1446. https://doi.org/10.1039/C8TC05545A.

[6] J.S. Shaikh, N.S. Shaikh, S.S. Mali, J. V. Patil, S.A. Beknalkar, A.P. Patil, N.L. Tarwal, P. Kanjanaboos, C.K. Hong, P.S. Patil, Quantum Dot Based Solar Cells: Role of Nanoarchitectures, Perovskite Quantum Dots, and Charge-Transporting Layers, ChemSusChem. 12 (2019) 4724–4753. https://doi.org/10.1002/cssc.201901505.

[7] J. Zhang, W. Zhang, H.M. Cheng, S.R.P. Silva, Critical review of recent progress of flexible perovskite solar cells, Mater. Today. 39 (2020) 66–88. https://doi.org/10.1016/j.mattod.2020.05.002.

[8] Y. Zhou, Y. Zhao, Chemical stability and instability of inorganic halide perovskites, Energy Environ. Sci. 12 (2019) 1495–1511. https://doi.org/10.1039/c8ee03559h.

[9] J. Satta, A. Casu, D. Chiriu, C.M. Carbonaro, L. Stagi, P.C. Ricci, Formation mechanisms and phase stability of solid-state grown cspbi3 perovskites, Nanomaterials. 11 (2021). https://doi.org/10.3390/nano11071823.

[10] H. Cho, Y.H. Kim, C. Wolf, H.D. Lee, T.W. Lee, Improving the Stability of Metal Halide Perovskite Materials and Light-Emitting Diodes, Adv. Mater. 30 (2018) 1704587. https://doi.org/10.1002/adma.201704587.

[11] J. Satta, C. Melis, C.M. Carbonaro, A. Pinna, M. Salado, D. Salazar, P.C. Ricci, Raman spectra and vibrational analysis of CsPbI3: A fast and reliable technique to identify lead halide perovskite polymorphs, J. Mater. 7 (2021) 127–135. https://doi.org/10.1016/j.jmat.2020.08.004.

[12] N.M. Dimitrijević, T. Rajh, S.P. Ahrenkiel, J.M. Nedeljković, O.I. Mićić, A.J. Nozik, Charge separation in heterostructures of InP nanocrystals with metal particles, J. Phys. Chem. B. 109 (2005) 18243–18249. https://doi.org/10.1021/jp051201y.

[13] M.T. Sheldon, P.E. Trudeau, T. Mokari, L.W. Wang, A. Paul Alivisatos, Enhanced semiconductor nanocrystal conductance via solution grown contacts, Nano Lett. 9 (2009) 3676–3682. https://doi.org/10.1021/nl902186v.

[14] K.C. Nawrot, D. Wawrzyńczyk, O. Bezkrovnyi, L. Kępiński, B. Cichy, M. Samoć, M. Nyk, Functional CdS-Au Nanocomposite for Efficient Photocatalytic, Photosensitizing, and Two-Photon Applications, Nanomaterials. 10 (2020). https://doi.org/10.3390/nano10040715.

[15] H. Wei, D. Ratchford, X. Li, H. Xu, C.K. Shih, Propagating surface plasmon induced photon emission from quantum dots, Nano Lett. 9 (2009) 4168–4171. https://doi.org/10.1021/nl9023897.

[16] S. Dey, J. Zhao, Plasmonic Effect on Exciton and Multiexciton Emission of Single Quantum Dots, J. Phys. Chem. Lett. 7 (2016) 2921–2929. https://doi.org/10.1021/acs.jpclett.6b01164.

[17] S. Carretero-Palacios, A. Jiménez-Solano, H. Míguez, Plasmonic Nanoparticles as Light-Harvesting Enhancers in Perovskite Solar Cells: A User's Guide, ACS Energy Lett. 1 (2016) 323–331. https://doi.org/10.1021/acsenergylett.6b00138.

[18] J.F. Liao, Y.T. Cai, J.Y. Li, Y. Jiang, X.D. Wang, H.Y. Chen, D. Bin Kuang, Plasmonic CsPbBr3–Au nanocomposite for excitation wavelength dependent photocatalytic CO2 reduction, J. Energy Chem. 53 (2020) 309–315. https://doi.org/10.1016/j.jechem.2020.04.017.

[19] X. Zhou, C. Bao, F. Li, H. Gao, T. Yu, J. Yang, W. Zhu, Z. Zou, Hole-transport-material-free perovskite solar cells based on nanoporous gold

back electrode, RSC Adv. 5 (2015) 58543–58548. https://doi.org/10.1039/c5ra11720h.

[20] J. Song, J. Li, L. Xu, J. Li, F. Zhang, B. Han, Q. Shan, H. Zeng, Room-Temperature Triple-Ligand Surface Engineering Synergistically Boosts Ink Stability, Recombination Dynamics, and Charge Injection toward EQE-11.6% Perovskite QLEDs, Adv. Mater. 30 (2018). https://doi.org/10.1002/adma.201800764.

[21] I. McCue, E. Benn, B. Gaskey, J. Erlebacher, Dealloying and Dealloyed Materials, Annu. Rev. Mater. Res. 46 (2016) 263–286. https://doi.org/https://doi.org/10.1146/annurev-matsci-070115-031739.

[22] G. Pia, M. Mascia, F. Delogu, Kinetics of nanoporous Au formation by chemical dealloying, Scr. Mater. 76 (2014) 57–60. https://doi.org/10.1016/J.SCRIPTAMAT.2013.12.016.

[23] L. Lutterotti, Total pattern fitting for the combined size-strain-stress-texture determination in thin film diffraction, Nucl. Instruments Methods Phys. Res. Sect. B Beam Interact. with Mater. Atoms. 268 (2010) 334–340. https://doi.org/10.1016/j.nimb.2009.09.053.

[24] Z. Qin, S. Dai, V.G. Hadjiev, C. Wang, L. Xie, Y. Ni, C. Wu, G. Yang, S. Chen, L. Deng, Q. Yu, G. Feng, Z.M. Wang, J. Bao, Revealing the Origin of Luminescence Center in 0D Cs4PbBr6 Perovskite, Chem. Mater. (2019). https://doi.org/10.1021/acs.chemmater.9b03426.

[25] O. Yaffe, Y. Guo, L.Z. Tan, D.A. Egger, T. Hull, C.C. Stoumpos, F. Zheng, T.F. Heinz, L. Kronik, M.G. Kanatzidis, J.S. Owen, A.M. Rappe, M.A. Pimenta, L.E. Brus, Local Polar Fluctuations in Lead Halide Perovskite Crystals, Phys. Rev. Lett. 118 (2017). https://doi.org/10.1103/PhysRevLett.118.136001.

[26] M. Liu, J. Zhao, Z. Luo, Z. Sun, N. Pan, H. Ding, X. Wang, Unveiling Solvent-Related Effect on Phase Transformations in CsBr-PbBr2 System: Coordination and Ratio of Precursors, Chem. Mater. 30 (2018) 5846–5852. https://doi.org/10.1021/acs.chemmater.8b00537.

[27] L.Q. Xie, T.Y. Zhang, L. Chen, N. Guo, Y. Wang, G.K. Liu, J.R. Wang, J.Z. Zhou, J.W. Yan, Y.X. Zhao, B.W. Mao, Z.Q. Tian, Organic-inorganic interactions of single crystalline organolead halide perovskites studied by Raman spectroscopy, Phys. Chem. Chem. Phys. 18 (2016) 18112–18118. https://doi.org/10.1039/c6cp01723a.

[28] J. Xiao, L. Qi, Surfactant-assisted, shape-controlled synthesis of gold nanocrystals, Nanoscale. 3 (2011) 1383–1396. https://doi.org/10.1039/c0nr00814a.

[29] J.E. Millstone, S.J. Hurst, G.S. Métraux, J.I. Cutler, C.A. Mirkin, Colloidal gold and silver triangular nanoprisms, Small. 5 (2009) 646–664. https://doi.org/10.1002/smll.200801480.

[30] Muniba, G. Naz, M.N. Anjum, M. Irfan, M. Irfan, M. Arshad, S.Z. Bajwa, W.S. Khan, Quats stabilized gold nanospheres for efficient ligand exchange procedure, Results Mater. 5 (2020) 100065. https://doi.org/10.1016/j.rinma.2020.100065.

[31] J. Chen, Z. Shen, P. Liu, Z. Sun, J.G. Liu, C. Shen, D. Song, S. Zhao, Z. Xu, Synergistic function of doping and ligand engineering to enhance the photostability and electroluminescence performance of CsPbBr3quantum dots, Nanotechnology. 32 (2021). https://doi.org/10.1088/1361-6528/abfc73.

[32] S.K. Balakrishnan, P. V. Kamat, Au-CsPbBr3 Hybrid Architecture: Anchoring Gold Nanoparticles on Cubic Perovskite Nanocrystals, ACS Energy Lett. 2 (2017) 88–93. https://doi.org/10.1021/acsenergylett.6b00592.

[33] J.R. Lakowicz, Principles of fluorescence spectroscopy, Springer US, Boston, MA, 2006. https://doi.org/10.1007/978-0-387-46312-4.

Chapter 6

Fabrication, characterization and modeling of NP Al

6.1 Introduction

Aluminum is widely used in transportation, construction, tools and consumables because of its properties such as plasticity, lightweight, non-toxicity, high thermal and electrical conductivity and passivation capability. Among metals, it is the most abundant in Earth's crust and its production is second only to iron [1]. Apart from the well-known and commonly exploited properties of Al, atomized powders showed catalytic activity toward various organic reactions [2]. Moreover, when its characteristic lengths decrease to the nanoscale, other important properties are manifested. Al nanostructures show plasmonic resonance that can be tuned by varying their size, structure, and oxide content from UV to near-infrared (NIR) [3,4]. Fine powders and nanoparticles have also been extensively studied as solid propellants [5–7]. With this regard, NP Al fabrication represents an essential goal for possible and innovative further applications in relevant advanced fields. Indeed, it has been shown that NP Al is a promising material for hydrogen generation [8] and ultraviolet (UV) plasmonic applications, such as Surface Enhanced Raman Spectroscopy (SERS) and Metal Enhanced Fluorescence (MEF) [9]. Moreover, Yang et al. recently reported that NP Al with a natural Al_2O_3 shell presents high chemical and thermal stability, light density and high strength [10]. These features make this material a promising valuable low-cost, self-supported, and tunable substrate for UV and visible-light SERS and MEF. Moreover, NP Al could also be of interest as a catalyst by matching the unique surface area and catalytic properties of NP metals with the Al catalytic activity [2]. Furthermore, the use of self-standing nanostructured material such as a NP metal for catalytic purposes could allow taking the advantages of both homogeneous and heterogeneous catalysis without the pelletizing process, which can be required when nanoparticles are employed as catalyst [11,12].

NP Al fabrication is challenging because of the high Al reactivity toward oxygen and water. The first of the few papers illustrating the preparation of a NP Al has been reported by Suárez et al.; it describes a fabrication method based on the electrochemical dealloying of Zn or Mg [13]. Later, Corsi et al. [8] demonstrated that NP Al could be prepared by this method in non-aqueous electrolytes under Ar atmosphere, thus preventing both Al

oxidation during its removal and ligament coarsening observed by Yang et al. [14] during Galvanic Replacement Reaction.

In this chapter, we address the production of NP aluminum by VPD, by treating an $Al_{20}Zn_{80}$ nanocomposite at a relatively high temperature under vacuum. Three steps are involved in the fabrication method: mechanical alloying of Al and Zn powders under Ar atmosphere, cold-pressing of powders into pellets and Zn removal during a thermal treatment under vacuum conditions. Although ligaments' coarsening could occur because of the relatively high temperature required with VPD, this preparation method is promising because of its ease and the possibility of fabricating relatively large amounts of materials.

Structure features have been investigated at different magnifications by Scanning Electron Microscopy (SEM) and Serial Block Face-Scanning Electron Microscopy (SBF-SEM), while surface area and pore volume have been characterized by N_2 physisorption measurements.

Since mechanical properties of NP Al are not studied in an exhaustive way, nanoindentation tests have been performed to estimate Young's modulus for the first time.

A further investigation of microstructure morphology has been performed by using a phenomenological model based on fractal geometry. Moreover, relevant applications of fractal modeling show its reliability not only to reproduce structure features of several materials, but also to predict their behavior under different conditions [15–17]. In this case, it has been possible to calculate specific surface (by simple geometrical measurements) and Young's modulus (by resolving series and parallel springs' patterns after model conversion), which have then been successfully compared with experimental measurements.

Finally, the optical properties and SERS-activity of NP Al were evaluated. We found that NP Al can be used as a SERS substrate with visible light excitation, too. This is ascribed to the presence of plasmonic absorption also in this spectral range.

6.2 Materials and Methods

6.2.1 Materials

Al with particle size <1 mm and 99.7 % of purity, Zn powders with particle size <0.149 mm and 99.8 % of purity and poly(3,4-ethylenedioxythiophene)-poly(styrenesulfonate) (PEDOT:PSS) (1.1 wt. % in H_2O) were purchased by Aldrich.

6.2.2 NP Al preparation

AlZn precursor fabrication

Elemental metals were mixed to prepare $Al_{20}Zn_{80}$ powder mixtures. The corresponding $Al_{20}Zn_{80}$ alloy was obtained by subjecting the powder mixtures to mechanical processing in a SPEX Mixer/Mill 8000. To this aim, 10 g of powder mixture were placed inside a cylindrical hardened steel reactor together with two 8-g stainless steel balls. Paraffin oil was used as a process-control agent to avoid powder agglomeration. The reactor was sealed under Ar atmosphere with impurities below 2 ppm. The mechanical processing was interrupted after 48 h. Processed powders were cold-pressed in the form of cylindrical pellets about 1.3 cm in diameter and 224 µm in thickness.

NP Al fabrication

The pellets were placed in the glass tube of a tubular furnace. The sample was kept for 1 h under high-vacuum conditions with pressure around 10^{-2} Pa. Then, the temperature was raised at 25 °C min^{-1} up to 550 °C. The sample was annealed at 550 °C for 1 h and then cooled gradually under high-vacuum conditions.

6.2.3 SEM imaging

The precursor alloy and resulting dealloyed material were investigated by SEM using a Zeiss Merlin microscope, equipped with a Schottky electron source, working with an acceleration voltage of 5 kV and an electron current of 150 pA at short working distance (high-resolution mode). Secondary electrons (SE) were collected to provide fine details on the surface morphology, while backscattered electrons (BSE) to detect differences in local composition. SE and BSE were gathered using an in-lens detector and a multiple-sector detector placed on the bottom of the SEM objective lens, respectively. SEM-Energy Dispersive Spectroscopy (EDS) measurements were performed by an Oxford silicon drift detector (SDD) with a detection area of 60 mm^2, collecting EDS spectra from 6 diverse, rectangular-shaped cross-sectional areas placed at increasing depth in the sample, aiming at finally covering the entire 224 µm-thick sample. In order to properly compare the result obtained, rectangular zones with same surface area were scanned by the electron beam, and an EDS spectrum from each of them was collected keeping the same SEM working conditions: acceleration voltage (30 kV), electron probe current (1 nA), and collection real-time (5 minutes per spectrum).

6.2.4 SBF-SEM imaging

For SBF-SEM imaging, the specimen was first embedded in EM-dedicated epoxy resin to obtain a small and compact block, then such a block was mounted on an Al specimen. Silver paint was used to electrically ground as much as possible the edges of the block to the aluminum pin. The entire block was then sputter-coated with a layer of gold capable of reflecting light to perform the fine SBF-SEM alignment. The block containing NP Al was then imaged using a ThermoFischer VolumeScope (VS) device, mounted into a ThermoFischer Teneo FEG SEM equipped with a Schottky field emission electron source, operating at an accelerating voltage of 2 kV, with a beam current of 50 pA, and upon low-vacuum conditions (50 Pa). Serial BSE-SEM images were acquired by a dedicated detector after cutting the specimen with a thickness of 100 nm, at different magnifications, and with resolution and dwell time chosen adequately to prevent further local specimen charging. For 3D reconstruction, rendering and analysis, serial SEM images were aligned and stacked into a volume using AVIZO software (ThermoFischer). 3D structures in image stacks containing hundreds or thousands of 2D ortho slices were traced individually in each plane and automatically surface rendered. From SBF-SEM stacks analysis, the features of larger pores (such as area, shape, characteristic lengths, and pore profile roughness) were estimated through a semi-automatic tool (Analyze Particles) using Fiji software [18]. Fractal dimension was estimated by using “Fractal Box Count” tool of Fiji [18].

6.2.5 XRD measurements

The structural and microstructural evolution of processed powders was investigated by X-Ray Diffraction (XRD). XRD measurements were carried out with a Rigaku Miniflex II Diffractometer equipped with a 600 W X-ray source using Cu $K_{\alpha 1}$ with an incident beam angle 2θ ranging from 30 to 100 degrees. Quantitative phase and microstructural analyses were performed using the Rietveld method [19].

6.2.6 N_2 physisorption measurements

N_2 physisorption measurements were carried out using a Micromeritics ASAP2020 apparatus. Adsorption and desorption isotherms were measured at 77 K. The Brunauer-Emmett-Teller (BET) method was utilized to estimate the specific surface area [20].

6.2.7 Mechanical properties measurements

The mechanical properties of suitably prepared NP Al samples were measured at room temperature using ex situ depth-sensing nanoindentation. To this aim a NanoTest Vantage Micro Materials indenter, equipped with a calibrated three-sided pyramid diamond Berkovich tip about 200 nm in radius, was used. Measurements were carried out within the indentation load range between 400 and 2400 μN. The loading rate was kept constant at 500 μN s^{-1}. Loading and unloading curves were measured on 36 indents per sample. The slope of the linear part of each unloading curve provides an estimate of the Young's modulus. The average Young's modulus was calculated by taking into account all the measured values.

6.2.8 UV-Vis absorption spectroscopy

UV-Vis absorbance spectrum of NP Al was acquired with the UV–Vis–NIR spectrometer Agilent Technologies Cary 5000. The sample was gently crushed into powder with an agate mortar and its absorbance was measured in diffuse reflectance measurement mode.

6.2.9 Raman Spectroscopy measurements

Raman measurements at the excitation wavelength of 532 nm were carried out in backscattering geometry with a wavelength stabilized diode module (LASOS e GLK series-532) coupled with a Reflecting Bragg Grating (Optigrate-Braggrade 532) to narrow the laser line. Measurements were performed at room temperature with a triple spectrometer Jobin-Yvon Dilor integrated system with a spectral resolution of about 1 cm^{-1}. Spectra were recorded in the Stokes region by a 1200 gr /mm grating monochromator and a liquid N-cooled charge coupled device (CCD) detector system.

Micro-Raman spectra at the wavelength of 1064 nm were taken in back scattering geometry with the spectrometer B&W TEK (Newark-USA) i-Raman Ex with a resolution less of 8 cm^{-1} coupled with an Nd:YAG LASER. The measurements were carried out at room temperature in a single spot of 1 mm^2 through the BAC151B Raman Video Micro-sampling system assembled with a 50x Olympus objective.

For SERS measurements, diluted PEDOT:PSS aqueous solution (0.01 wt.%) was drop-casted on glass slide, bulk Al pellet and NP Al. The spectra were recorded with laser excitation at 532 nm and at 1064 nm.

6.2.10 Fractal model

A phenomenological model based on fractal geometry was developed with the aim to reproduce the porous structural features (pore size distribution, pore size range, pore fraction) and predict specific surface area and Young's modulus of NP Al [15]. In particular, the proposed fractal model, called IFU, was obtained by using Sierpinski carpet, a well-known example of fractal geometry as a base unit. This fractal figure was constructed by starting from a square in which each side (l) is divided by a numerical factor *F* generating equal sub-squares (Eq. 6-1). Some of these sub-squares can be removed by creating a structure formed by solid and void with the same characteristic length [15].

$$L_e^{(max)} = \frac{l}{F}. \qquad \textit{Eq. 6-1}$$

The obtained objects were characterized by the non-integer dimension calculated by

$$\mathrm{D_f} = \frac{\log\left(\mathrm{N_{RSQ}}\right)}{\log\left(\mathrm{F}\right)}, \qquad \textit{Eq. 6-2}$$

where N_{RSQ} denotes the number of sub-squares non removed at the first iteration. The described step was repeated on all sub-squares generating a self-similar pattern in which at the n-th iteration, the size of voids was:

$$L_e^{(n)} = \frac{L_e^{(max)}}{F^{(n-1)}}. \qquad \textit{Eq. 6-3}$$

Iteration by iteration, it was possible to note that new classes of voids were generated, and monotonic pore size distribution could be obtained. However, real materials in general have different pore size distribution curves (non-monotonic) in which one or more maxima can be found in correspondence with any pore class. These structures could be approximated by a modeling procedure based on IFU. The number of unit base type was related to complexity of cumulative curve of porous structure. One unit for every inflection point. For the investigated systems, two structural types of units' base were used: 1 unit Sierpinski carpet A and n_B Sierpinski carpet B (for simplicity unit A and unit B), with different characteristic lengths and D_f.

The pore fraction resulting from intermingling was given by

$$\varepsilon_{mod} = \frac{A_{Ap} + n_B \cdot A_{Bp}}{A_A + n_B \cdot A_B} \quad \text{Eq. 6-4}$$

where A_A, A_B, $A_{Ap,}$ and A_{Bp} are total areas and total pore areas of A and B units, respectively. After porosimetric tests or image analysis, it was possible to use the experimental measurement value for calculating n_B

$$n_B = \frac{A_{Ap} - \varepsilon_{exp} \cdot A_A}{\varepsilon_{exp} \cdot A_B - A_{Bp}} \quad \text{Eq. 6-5}$$

where ε_{exp} is the experimental pore fraction. In order to improve the versatility of the model, different settings could be used, such as: (a) maintain *solid forever* some sub-squares of unit A and units B; (b) introduce non-porous surface to control pore fraction of the entire model; (c) make pore profile tortuous in longitudinal or transverse direction for reproducing specific surface and morphological characteristics. In particular, concerning tortuous pore profile, it can be characterized by rough path $L_t^{(n)}$ which was calculated by

$$L_t^{(n)} = L_e^{(n)} \delta^{-i^{1-D_t}} \quad \text{Eq. 6-6}$$

where D_t is tortuous fractal dimension and

$$\delta = F^{-n} \quad \text{Eq. 6-7}$$

As reported in Fig. 6.5, a tortuous pore profile was constructed around the square edge of a void to leave unaffected the solid and void fraction. Consequently, the pore cross-sectional area was considered constant and independent of the specific profile. Since the IFU is the smallest representative part of microstructure, a method to compare data with IA (referred to the examined surface) had to be used. For this, the total length of pore profiles was divided by total model surface (A_{IFU}),

$$L_S = \frac{\sum_1^n L_e^{(n)} \delta^{-i^{1-D_t}}}{A_{IFU}} \quad \text{Eq. 6-8}$$

Moreover, it was possible to calculate specific surface area by considering IFU unitary model extrusion along transversal direction and the specific weight of material solid phase, w_s.

$$S_s = \frac{L_s t}{w_s} \quad \text{Eq. 6-9}$$

After phenomenological reconstruction of microstructure, the fractal model can be converted into an analytical multi-scale homogenization pattern composed of springs allocated in series and parallel. Starting from the smallest cell (generated by the last iteration n), the effective Young's modulus $E^{(i)}$ was computed, and the result was used as the modulus of a solid part at n -1 iteration [15].

At the n iteration, an analytical expression for stiffness of each spring was represented by

$$k_{qr}^{(n)} = \chi_{qr}\, E_s \frac{A_e^{(n)}}{L_e^{(n)}}, q = I, II, III, r = 1, 2, 3 \qquad \text{Eq. 6-10}$$

where χ_{qr} is a characteristic function which is equal to 0 for pore and 1 for solid, E_s denotes the elastic modulus of the solid phase, $A_e^{(n)}$ represents the cross-sectional area (per unit out-of-plane thickness) and $L_e^{(n)}$ stands for the length of the corresponding sub-square. These last geometrical features were the same in all sub-squares. The effective Young's modulus was calculated by

$$E^{(n)} = \left[\sum_{q=I,II,III} \left(\frac{1}{\sum_{r=1,2,3} E_{qr}^{(n)}} \right) \right]^{-1} \qquad \text{Eq. 6-11}$$

where $E_{qr}^{(n)} = \chi_{qr}\, E_s$ [15].

The Young's modulus of the entire fractal structure was given by the harmonic average of Young's modulus of each base unit and filled surface. The three-dimensional structure was reproduced by giving to the IFU an arbitrary unit thickness.

6.3 Results and Discussion

The XRD pattern of the $Al_{20}Zn_{80}$ powder mixture mechanically processed for 48 h is shown in Fig. 6.1a and compared with the reference XRD patterns of pure Al and Zn. The mechanical processing made Al reflections disappear, and Zn ones broaden. The Rietveld analysis indicates that broadening can be ascribed to the reduction of grain size from the initial value of about 100 nm to the final one of about 70 nm. A small downward shift of about 0.1° in the angular position of Zn peaks is detected. Based on

the Al and Zn atomic radii [21], it can be ascribed to a terminal solid solubility of Al in Zn [22], with the two elements remaining substantially segregated.

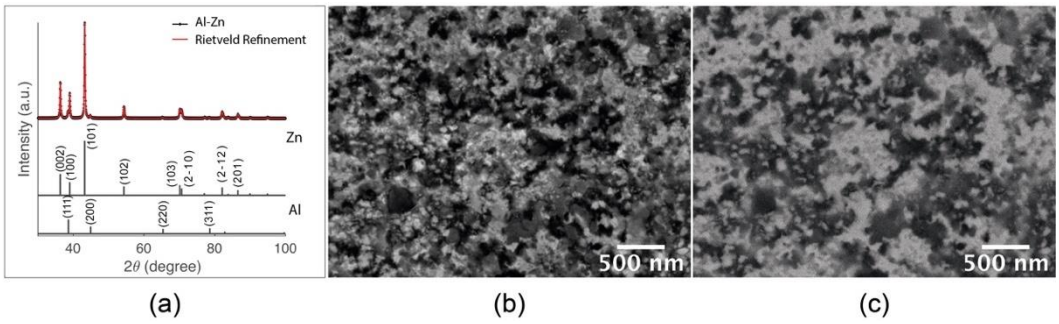

Fig. 6.1 (a) XRD pattern and Rietveld refinement of the $Al_{20}Zn_{80}$ nanocomposite, compared with reference reflection peaks of Al and Zn elements. SEM micrographs of the nanocomposite collected using (b) SE and (c) BSE.

Therefore, it can be concluded that the mechanical processing of the $Al_{20}Zn_{80}$ powder mixtures induces the formation of a nanocomposite. The SEM micrographs, such as the ones shown in Fig. 6.1b and Fig. 6.1c, provide support to this conclusion. In particular, the SEM-BSE imaging indicates that the nanocomposite consists of finely dispersed nanocrystalline phases with diverse atomic number. Specifically, the zones appearing brighter have a higher atomic number, *i.e.*, a higher Zn percentage. As shown by the SEM micrographs reported in Fig. 6.2, the annealing at 550 °C under high-vacuum conditions for 1 h drastically changes the material microstructure. As shown in Fig. 6.2a, the sample surface exhibits the typical appearance of NP metals, with nanosized ligaments and pores (approximately 10 nm). The SEM micrograph in Fig. 6.2b reveals that the NP architecture is maintained inside the sample, although the ligament size appears to be larger.

EDS measurements, shown in Fig. 6.2c and Fig. A.II.1 (supplementary material can be found in **Appendix A.II**) indicate that the Zn atomic percentage, normalized with respect to the sum of Al and Zn ones, mostly averages around 1% near the pellet surface, while it increases up to about 3% near the opposite surface. Therefore, Zn has been almost completely removed from the sample. The O content is related to the oxidation of the Al surface, with consequent formation of a thin passivation layer [23].

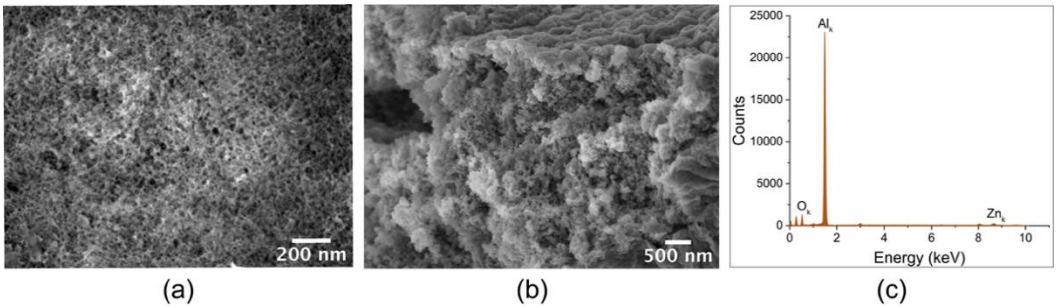

Fig. 6.2 SEM-SE micrographs of (a) the NP Al surface and (b) the NP Al cross-section; (c) EDS spectrum corresponding to the cross-sectional area included between 37 and 74 μm from the pellet surface with ~3% of Zn content. Spectra of the other areas of the sample are reported in Fig. A.II.1.

The experimental evidence heretofore presented definitely suggests that we have been able to fabricate almost pure NP Al. The architecture we observe can be well described in terms of open cells with irregular morphologies that tessellate the entire sample volume. Therefore, the NP Al can be considered a truly NP metal with ligaments characterized by a relatively high aspect ratio, which gives them their stocky appearance. It is possible to note that the sample shows a porous structure over its whole volume. However, relatively large voids, such as the one shown in Fig. 6.3a, have been observed. Our first hypothesis is that they are due to the incomplete compaction of the nanocomposite powders during the preparation of pellets.

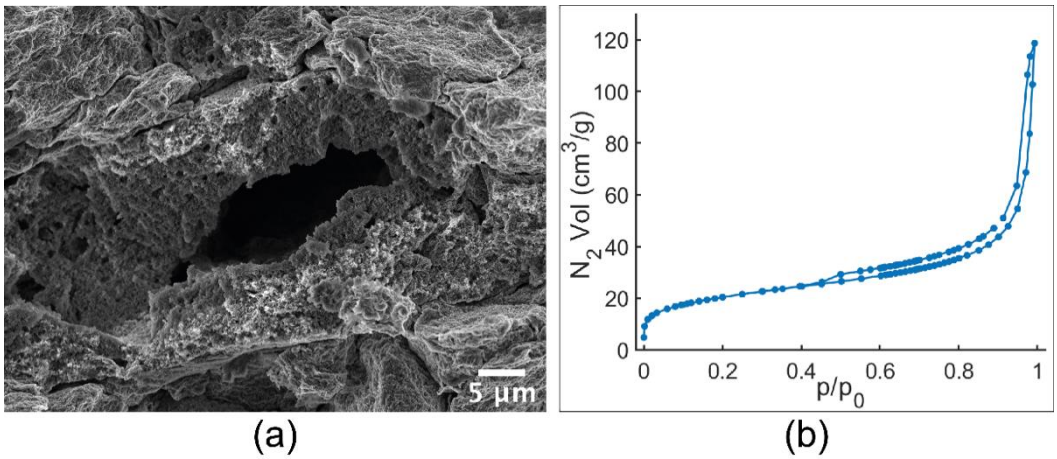

Fig. 6.3 (a) SEM-SE micrograph of the NP Al cross-section showing a quite large, internal pore. (b) N_2 physisorption isotherms obtained from the whole NP Al specimen.

The shape of the N_2 physisorption isotherms shown in Fig. 6.3b is associated to the occurrence of a hysteresis loop and does not strictly match with a specific classification, supporting the NP Al structure's inhomogeneity [24]. The NP Al specific surface area as obtained by BET analysis is nearly 73 $m^2\ g^{-1}$, a remarkably large value that compares well with the highest literature values for NP metals [25,26]. Although limitations associated to surface area determination by physisorption routes have been reported, the

correlation with the structural features has been pointed out [25–27]. For instance, NP Au can have a specific surface area as large as 85 $m^2 g^{-1}$ when its ligaments are about 7 nm in size [25]. From pore volume evaluation, a porosity of 40% can be estimated, relative to those pores smaller than 300 nm.

The presence of nanosized ligaments and pores represents a fundamental aspect of a NP materials. However, it is well known that the performances of this kind of materials also depend on larger-scale cavities by influencing various parameters, such as the mass transport of fluids, mechanical properties, electrical and thermal conductivity [28,29]. Thus, aiming at investigating the overall porous structure of the specimen, a technique capable to reveal its internal 3D structure appeared of pivotal importance. As a consequence, SBF-SEM experiment was carried out on it. By this technique, the sample 3D structure along the entire 270 µm cross-section profile was determined (example images of the cross-section at two different magnifications are shown in supplementary material, Fig. A.II.2) and the obtained micrographs allow to analyze NP Al at different scales with a resolution of 300 nm.

From the SBF-SEM measurements, the 3D reconstruction and a representative video of the porous structure evolution during the subsequent cuts of the entire cross-section profile are shown in Fig. 6.4 and in the supplementary material, respectively. Quantitative analysis of SBF images was focused near the surfaces and in the interior of the sample (see Fig. A.II.3). Indeed, it can be observed that the two surfaces have smaller pores and a higher overall porosity with respect to the inner part of the sample, as can be clearly seen also by the 3D reconstructions at low (Fig. 6.4) and higher (Fig. A.II.4) magnification. Moreover, the dense areas of the sample manifest different brightness levels, associated to a higher concentration of Zn in the brightest areas (and a lower one in the inverted images in Fig. A.II.2 and Fig. A.II.3). The Zn-richest areas are found to be more prevalent in the interior of the specimen due to the slower Zn removal in the inner part of the sample.

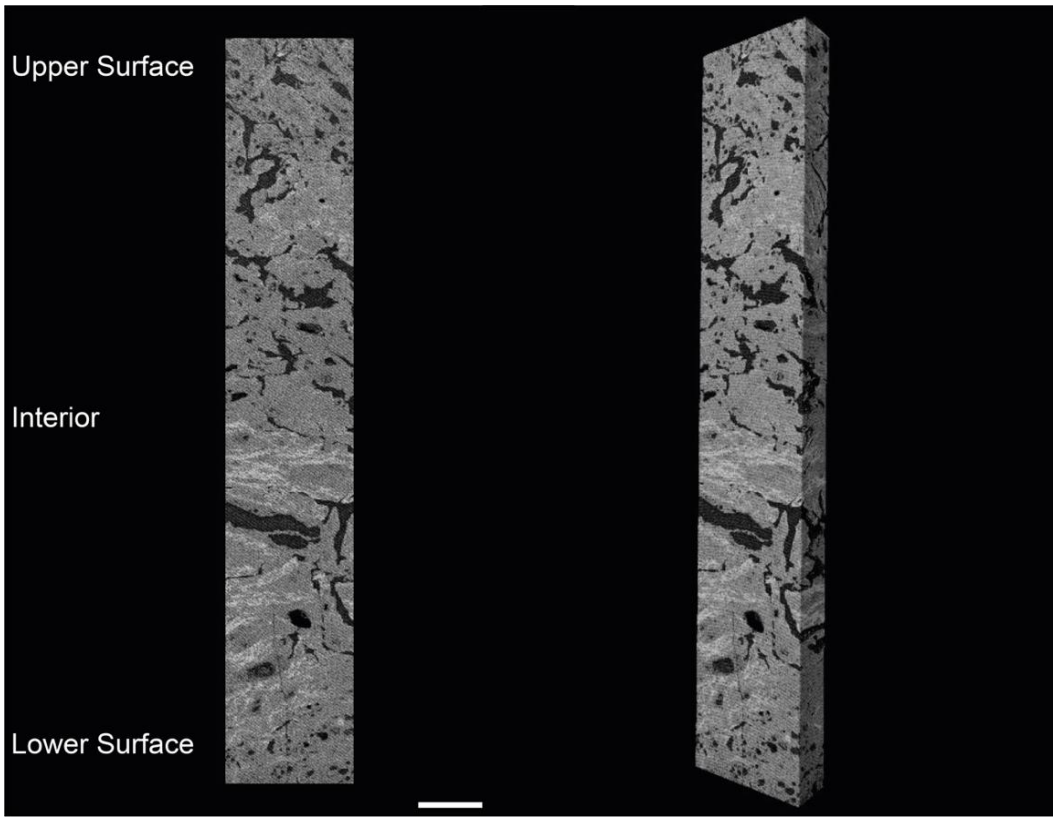

Fig. 6.4 SEM-SBF 3D reconstruction of cross-section profile of NP Al; scale bar: 20 µm.

From SBF-SEM and by using IA techniques, it has been possible to estimate an additional porosity of 10% related to pores larger than 300 nm, which cannot be estimated by N_2 physisorption measurements. Therefore, by adding this value to the porosity relative to pores smaller than 300 nm, a rough estimation of the overall porosity lies around 50%. IA of SBF-SEM images was also carried out to elaborate pore cumulative curves for voids with characteristics length higher than 300 nm. Consequently, in order to reproduce these experimental findings, an IFU model (see Fig. 6.5) has been applied and input data has been reported in Table 6.1. In Fig. 6.6a, cumulative curve obtained by IA elaborations has been compared with fractal pore structure. It is possible to observe that the proposed model can reproduce the experimental data. Moreover, IA allows calculating the fractal dimension (Dt) of pores that is about 1.17 ± 0.02. By using Eq. 6-8, it is possible to estimate the length of the tortuous profile of each pore.

Table 6.1 Input data of Intermingled Fractal Units' model

		E1-1
Unit A	D_f	1.77
	n	1
	R_{max} ***(μm)***	16.5
	Iteration	4
	R_{min} ***(μm)***	0.2
	Solid forever	2
Unit B	D_f	1.89
	n	98
	R_{max} ***(μm)***	5.5
	Iteration	3
	R_{min} ***(μm)***	0.2
	Solid forever	4
	Filled surface (μm^2)	$1.12 \cdot 10^5$

Furthermore, in this case, the measured and calculated data, referred per unit of surface, are very comparable, 0.33 μm^{-1} and 0.30 μm^{-1} respectively. However, the pore fraction relative to IA observation is only ⅕ of total porosity (equal to 50%). In order to have an overall description of porosity, IFU models have been used to design possible pore size distributions. These designed cumulative curves are built considering pore size range from SEM observations and overall porosity from SBF-SEM stacks and N_2 physisorption measurements. In Fig. 6.6b pore size distributions design by using input data reported in Table 6.2, have been shown. It is possible to notice that, as supposed, pore size range and pore fraction are equal for every cumulative curve but yet they have different pore size distributions.

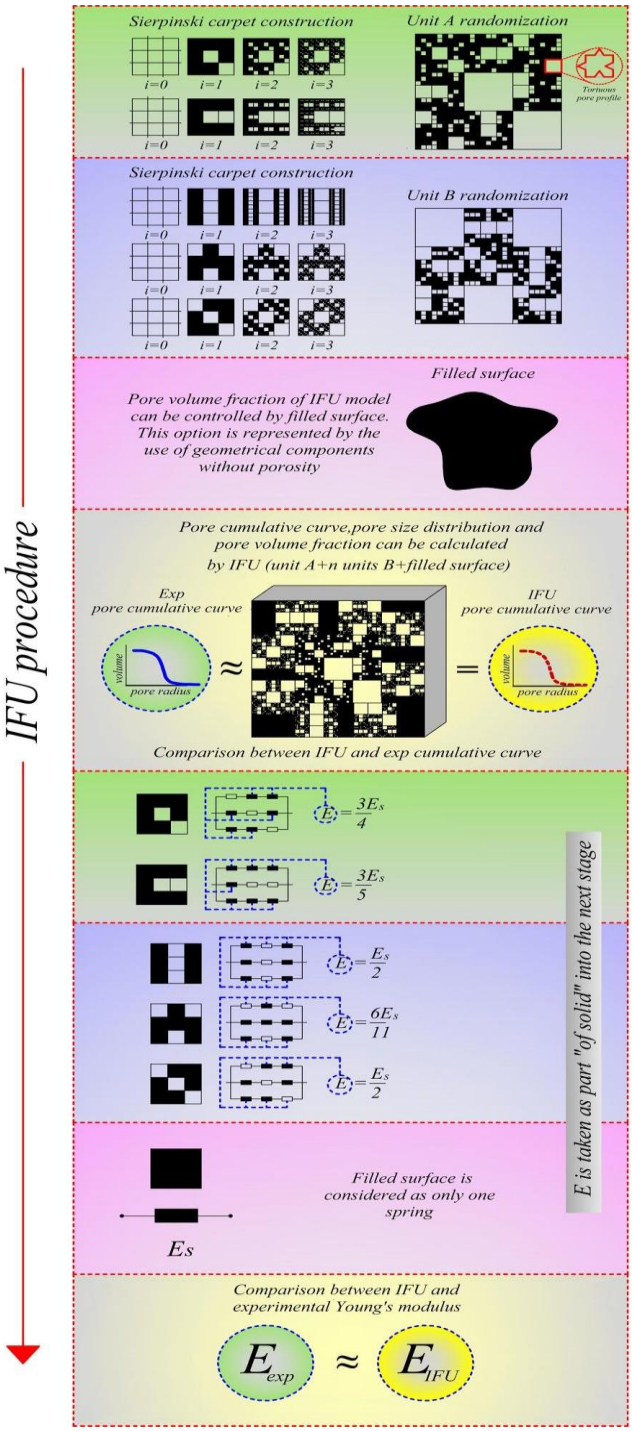

Fig. 6.5 Representative scheme of IFU model working structure.

The remarkable capability of the model to reproduce experimental data is confirmed by the calculated specific surface (Eq. 6-9), which is equal to 73 ± 7 m^2/g *vs* about 73 ± 1 m^2/g, obtained by BET.

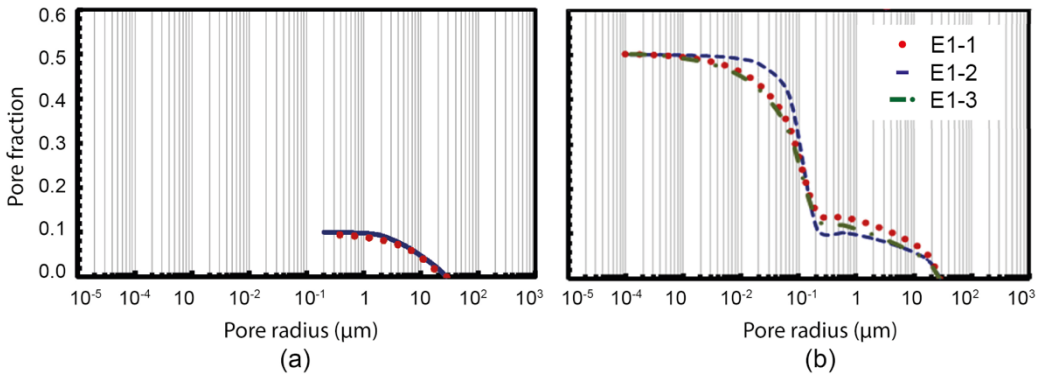

Fig. 6.6 (a) Comparison between porosimetric curves obtained by IA and Fractal modeling; (b) model pore cumulative curves for NP Al, E1-1, E1-2, E1-3, whose input data are reported in Table 6.2.

Table 6.2 Input data of fractal models for complete porous microstructure of NP Al.

		E1-1	E1-2	E1-3
Unit A	D_f	1.89	1.89	1.77
	n	1	1	1
	R_{max} (μm)	16.5	16.5	16.5
	Iteration	10	10	10
	R_{min} (μm)	0.001	0.001	0.001
	Solid forever	0	1	2
Unit B	D_f	1.77	3	1.89
	n	261	375	422
	R_{max} (μm)	1.83	1.83	1.83
	Iteration	9	9	9
	R_{min} (μm)	0.2	0.2	0.2
	Solid forever	5	0	2
	Filled surface (μm^2)	0	0	0

The capability of the fractal model to describe porous structures allows using it for predicting elastic properties [15]. Based on Eq. 6-11, the Young's modulus is estimated to be about 18 ± 2 GPa. As mentioned above, in this paper is reported the first experimental estimation of elastic behavior for NP Al. Mechanical tests allow to estimate the value of nanoindentation Young's modulus which is equal to 18.3 ± 1.4 GPa, which is very close to that predicted by the model.

Moreover, SERS measurements were carried out with NP Al as a substrate using PEDOT:PSS, a commercial conductive polymer, as a probe. Fig. 6.7 shows the Raman spectra of PEDOT:PSS aqueous dispersion drop-casted on glass slide and on NP Al, excited at 532 nm. The intensity of the spectrum with NP Al is around 14 times larger than that of PEDOT:PSS on glass. The measurements were also carried out with 1064 nm laser excitation and no enhancement was detected. Moreover, no enhancement was found by drop casting the polymer on bulk Al pellet. These observations confirm the plasmonic nature of the enhancement.

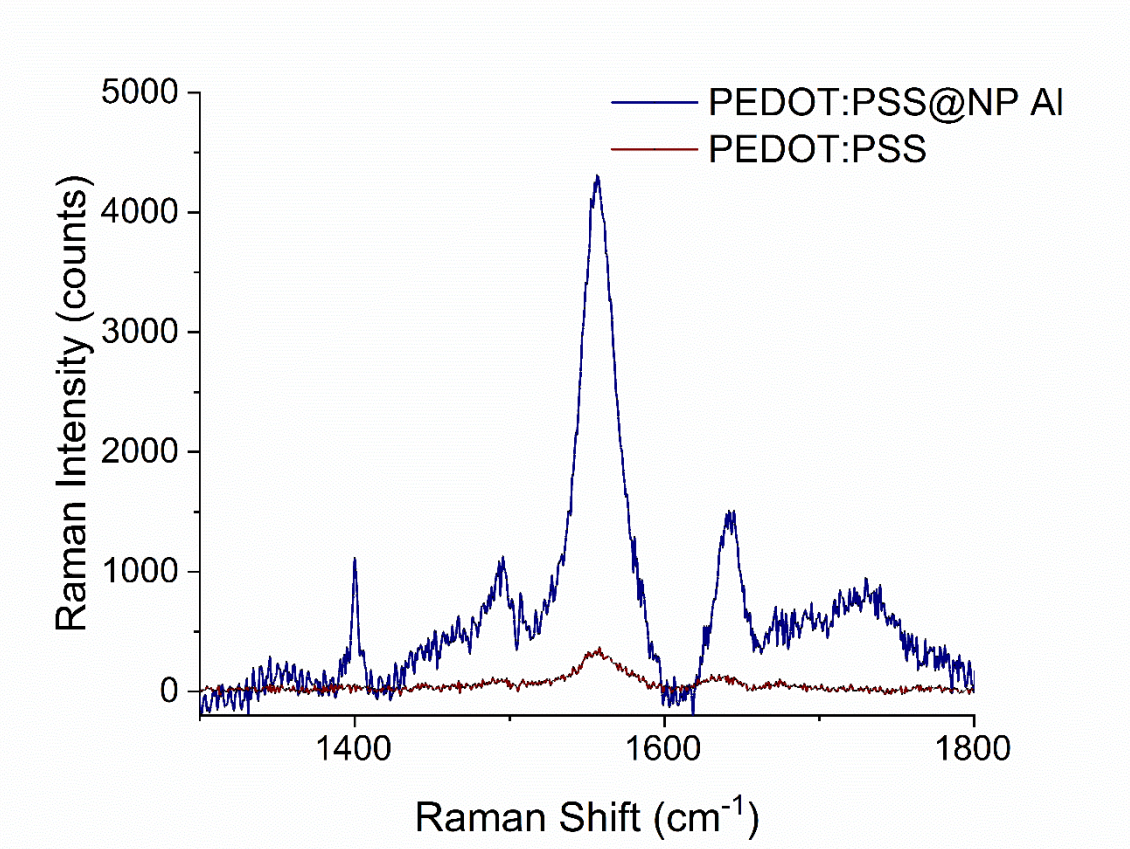

Fig. 6.7 SERS spectrum of PEDOT:PSS on NP Al versus Raman spectrum of PEDOT:PSS on glass slide.

Even if the enhancement factor is low, it is interesting to note that NP Al shows it SERS also in the visible range and not only in UV [9]. This can be

ascribed to the characteristic lengths of the material and Al_2O_3 passivation layer thickness. Indeed, it is known that Al nanostructures plasmonic absorption can be tuned by changing its size and oxide content. In particular, the plasmonic absorption was found to undergo a red-shift at increasing size and oxide content of the nanostructure; moreover the increase in the oxide content was also related to a decrease in the Al plasmonic absorption intensity [30]. Therefore, by controlling the structure of the material, it is possible to tune the plasmonic properties of NP Al for a wide range of low-cost applications.

6.4 Conclusions

We have shown that the VPD method can be successfully used to fabricate NP Al starting from an $Al_{20}Zn_{80}$ nanocomposite prepared by mechanical processing. Annealing the $Al_{20}Zn_{80}$ nanocomposite at 550 °C for 1 h allows removing Zn almost completely, leaving an NP Al structure with a high surface area. Moreover, by SBF-SEM technique a 3D reconstruction of the NP structure was obtained. A fractal model based on Sierpinski carpet as unit was proposed, and it showed to be able to model well the porous microstructure of NP Al. This phenomenological model allowed us to predict some features of this material, such as specific surface area and Young elastic modulus which are very close to experimental ones. The notable capability shown by this model to reproduce the experimental data encourages the development of this methodology which can be in principle applied to any possible NP metals. Moreover, we found that NP Al is SERS-active in the visible range.

The fabrication of NP Al with this method is unprecedented and can mark a progress in the field. Al is a lightweight metal almost ubiquitous in modern technology and the availability of a lighter version of the metal can pave the way to a number of applications in strategic sectors of industry.

References

[1] J. Emsley, Nature’s building blocks : everything you need to know about the elements, Oxford University Press, 2011.

[2] M. Gopalakrishnan, P. Sureshkumar, V. Kanagarajan, J. Thanusu, Aluminium metal powder (atomized) catalyzed Friedel-Crafts acylation in solvent-free conditions: A facile and rapid synthesis of aryl ketones under microwave irradiation, Catal. Commun. 6 (2005) 753–756. https://doi.org/10.1016/j.catcom.2005.07.013.

[3] M.W. Knight, N.S. King, L. Liu, H.O. Everitt, P. Nordlander, N.J. Halas, Aluminum for Plasmonics, ACS Nano. 8 (2014) 834–840. https://doi.org/10.1021/nn405495q.

[4] K.B. Mogensen, M. Gühlke, J. Kneipp, J.B. Wagner, M.E. Palanco, H. Kneipp, K. Kneipp, Surface-enhanced Raman scattering on aluminum using near infrared and visible excitation, Chem. Commun. 50 (2014) 3744–3746. https://doi.org/10.1039/c4cc00010b.

[5] A. Dokhan, E.W. Price, R.K. Sigmant, J.M. Seitzman, The effects of al particle size on the burning rate and residual oxide in aluminized propellents, in: 37th Jt. Propuls. Conf. Exhib., 2001. https://doi.org/10.2514/6.2001-3581.

[6] L. Galfetti, L.T. De Luca, F. Severini, L. Meda, G. Marra, M. Marchetti, M. Regi, S. Bellucci, Nanoparticles for solid rocket propulsion, J. Phys. Condens. Matter. 18 (2006) S1991. https://doi.org/10.1088/0953-8984/18/33/S15.

[7] L.T. De Luca, L. Galfetti, F. Severini, L. Meda, G. Marra, A.B. Vorozhtsov, V.S. Sedoi, V.A. Babuk, Burning of nano-aluminized composite rocket propellants, Combust. Explos. Shock Waves. 41 (2005) 680–692. https://doi.org/10.1007/s10573-005-0080-5.

[8] J.S. Corsi, J. Fu, Z. Wang, T. Lee, A.K. Ng, E. Detsi, Hierarchical Bulk Nanoporous Aluminum for On-Site Generation of Hydrogen by Hydrolysis in Pure Water and Combustion of Solid Fuels, ACS Sustain. Chem. Eng. 7 (2019) 11194–11204. https://doi.org/10.1021/acssuschemeng.9b00481.

[9] D. Garoli, A. Schirato, G. Giovannini, S. Cattarin, P. Ponzellini, E. Calandrini, R.P. Zaccaria, F. D'amico, M. Pachetti, W. Yang, H.J. Jin, R. Krahne, A. Alabastri, Galvanic replacement reaction as a route to prepare nanoporous aluminum for UV plasmonics, Nanomaterials. 10 (2020) 1–12. https://doi.org/10.3390/nano10010102.

[10] W. Yang, Z.P. Luo, W.K. Bao, H. Xie, Z.S. You, H.J. Jin, Light, strong, and stable nanoporous aluminium with native oxide shell, Sci. Adv. 7 (2021). https://doi.org/10.1126/sciadv.abb9471.

[11] C.A. Witham, W. Huang, C.K. Tsung, J.N. Kuhn, G.A. Somorjai, F.D. Toste, Converting homogeneous to heterogeneous in electrophilic catalysis using monodisperse metal nanoparticles, Nat. Chem. 2 (2010) 36–41. https://doi.org/10.1038/nchem.468.

[12] W. Huang, J.H.C. Liu, P. Alayoglu, Y. Li, C.A. Witham, C.K. Tsung, F.D. Toste, G.A. Somorjai, Highly active heterogeneous palladium nanoparticle catalysts for homogeneous electrophilic reactions in solution and the utilization of a continuous flow reactor, J. Am. Chem. Soc. 132 (2010) 16771–16773. https://doi.org/10.1021/ja108898t.

[13] O.M. Suárez, E.G. Estremera, R. Soler, A. Declet, A.J. Hernández-maldonado, Fabrication of Porous and Nanoporous Aluminum via Selective Dissolution of Al-Zn Alloys, 2014 (2014) 1–7. https://doi.org/10.1155/2014/963042.

[14] W. Yang, X.-G. Zheng, S.-G. Wang, H. Jin, Nanoporous Aluminum by Galvanic Replacement : Dealloying and Inward-Growth Plating, J. Electrochem. Soc. 165 (2018) 492–496. https://doi.org/10.1149/2.0881809jes.

[15] L. Casnedi, R. Licheri, M. Brun, G. Pia, From nature geometry to material design: Advanced fractal nature analysis for predicting experimental elastic properties, Ceram. Int. 46 (2020) 23947–23955. https://doi.org/10.1016/j.ceramint.2020.06.171.

[16] G. Pia, High porous yttria-stabilized zirconia with aligned pore channels: Morphology directionality influence on heat transfer, Ceram. Int. 42 (2016) 11674–11681. https://doi.org/10.1016/j.ceramint.2016.04.078.

[17] J. Cai, E. Perfect, C.L. Cheng, X. Hu, Generalized modeling of spontaneous imbibition based on hagen-poiseuille flow in tortuous capillaries with variably shaped apertures, Langmuir. 30 (2014) 5142–5151. https://doi.org/10.1021/la5007204.

[18] J. Schindelin, I. Arganda-Carreras, E. Frise, V. Kaynig, M. Longair, T. Pietzsch, S. Preibisch, C. Rueden, S. Saalfeld, B. Schmid, J.Y. Tinevez, D.J. White, V. Hartenstein, K. Eliceiri, P. Tomancak, A. Cardona, Fiji: An open-source platform for biological-image analysis, Nat. Methods. 9 (2012) 676–682. https://doi.org/10.1038/nmeth.2019.

[19] H.M. Rietveld, A profile refinement method for nuclear and magnetic structures, J. Appl. Crystallogr. 2 (1969) 65–71. https://doi.org/10.1107/s0021889869006558.

[20] S. Brunauer, P.H. Emmett, E. Teller, Adsorption of Gases in Multimolecular Layers, J. Am. Chem. Soc. 60 (1938) 309–319. https://doi.org/10.1021/ja01269a023.

[21] V.A. Lubarda, On the effective lattice parameter of binary alloys, Mech. Mater. 35 (2003) 53–68. https://doi.org/10.1016/S0167-6636(02)00196-5.

[22] Ž. Skoko, G. Štefani, Microstructure of Al-Zn and Zn-Al Alloys, 82 (2009) 405–420.

[23] C. Langhammer, M. Schwind, B. Kasemo, I. Zorić, Localized surface plasmon resonances in aluminum nanodisks, Nano Lett. 8 (2008) 1461–1471. https://doi.org/10.1021/nl080453i.

[24] M. Thommes, K. Kaneko, A. V. Neimark, J.P. Olivier, F. Rodriguez-Reinoso, J. Rouquerol, K.S.W. Sing, Physisorption of gases, with special reference to the evaluation of surface area and pore size distribution (IUPAC Technical Report), Pure Appl. Chem. 87 (2015) 1051–1069. https://doi.org/10.1515/pac-2014-1117.

[25] C. Lakshmanan, R.N. Viswanath, S.R. Polaki, R. Rajaraman, S. Dash, A.K. Tyagi, Electrochimica Acta Surface area of nanoporous gold : Effect on temperature, Electrochim. Acta. 182 (2015) 565–572. https://doi.org/10.1016/j.electacta.2015.09.104.

[26] H. Xu, S. Pang, Y. Jin, T. Zhang, General synthesis of sponge-like ultrafine nanoporous metals by dealloying in citric acid, Nano Res. 9 (2016) 2467–2477. https://doi.org/10.1007/s12274-016-1133-7.

[27] Y. Liu, S. Bliznakov, N. Dimitrov, Comprehensive study of the application of a pb underpotential deposition-assisted method for surface area measurement of metallic nanoporous materials, J. Phys. Chem. C. 113 (2009) 12362–12372. https://doi.org/10.1021/jp901536f.

[28] Y. Ding, J. Erlebacher, Nanoporous metals with controlled multimodal pore size distribution, J. Am. Chem. Soc. 125 (2003) 7772–7773. https://doi.org/10.1021/ja035318g.

[29] T. Fujita, Hierarchical nanoporous metals as a path toward the ultimate three-dimensional functionality, Sci. Technol. Adv. Mater. 18 (2017) 724–740. https://doi.org/10.1080/14686996.2017.1377047.

[30] D. Gerard, S.K. Gray, Aluminium plasmonics, J. Phys. D. Appl. Phys. 48 (2015). https://doi.org/10.1088/0022-3727/48/18/184001.

Chapter 7

Topology-dependent mechanical response of NP Au reconstructions

7.1 Introduction

Introduced in **Chapter 1**, the mechanical properties of NP metals represent a subject of intensive studies, fueled from one side by the fascinating potential combination of low density and high strength, and from the other side by its characteristic brittleness that up to now has prevented almost any real application of NP metals [1–3].

The progress in this field is hampered by the fragmentary and often contradictory published data [4] and by the difficult decoupling of the contribution to the mechanical response by sample defects at different length scales – such as grain boundaries, cracks, dislocations and surface effects – with the pure mechanical behavior that would be associated with the bicontinous interconnected geometry of ligaments and pores typical of NP Au [4–6].

Bearing in mind these issues, we have started a still in progress work in which we focus only the geometry of NP Au, by reproducing its structure, investigated by SEM, into macroscopic specimens by 3D printing. This way, it has been possible to investigate the behavior of samples with the same structure of NP Au – in a 2D approximation – excluding all the other phenomena that arise in a realistic sample. The mechanical behavior of the printed specimen has been experimentally investigated by means of Digital Image Correlation (DIC) and extensometer during tensile tests. The first technique permits to monitor the local displacement of any specimen area during tensile test [7]. It gives therefore local information about the mechanical response of the specimen and at the same time about the global response, such as the Young's modulus of the entire sample. We calculated this parameter also by the standard extensometer measurements. The results have been compared with Finite Element Method [8], and established the accordance between the three methods, FEM was used to perform the same study to other NP Au areas of the same sample. From the preliminary results, we have observed that NP Au local inhomogeneities difficult to detect by image analysis heavily govern the local response of the material, which varies by changing the size of the area analyzed. Above a certain length scale of the test area, the global effect of the local inhomogeneities becomes constant and does not depend anymore by the size of the area analyzed.

7.2 Materials and Methods

7.2.1 NP Au fabrication

AuAg alloy fabrication

2 g of AuAg powder mixture was prepared in an atomic ratio of 30:70. The powders were mechanically milled in a SPEX *8000M Mixer/Mill* ball mill for 16 h in a hardened steel vial with two hardened steel balls of 8 g each. The powders were removed from the sides of the vial every 30 minutes in the first 2 hours and then every 5 h, in order to homogenize the mixture. Pellets of 1.3 cm of diameter and 1 mm of thickness were prepared by cold pressing under 10 tons for 5 min with a hydraulic press.

Dealloying of AuAg alloy

NP Au was prepared by chemical dissolution of Ag in concentrated HNO_3 for 6 h. After the treatment, the pellets were rinsed three times and stored in ultrapure water for 24h. Then, the samples were dried in a desiccator.

7.2.2 SEM imaging, processing and analysis

NP Au morphology was investigated by SEM using a Zeiss Merlin microscope, equipped with a Schottky electron source, working with an acceleration voltage of 5 kV at short working distance (high-resolution mode). Secondary electrons (SE) were collected to provide fine details on the surface morphology. SE were gathered using an in-lens detector. Image processing and analysis were performed with Adobe Photoshop® and Fiji [9]. The ligament thickness s of binarized images of each set is around 19 ± 6 nm. From NP Au images, three different areas of the sample were taken in account and binarized. From each area, a number of concentric squares of different sizes were collected to form a set of images representing the material at different scales. The three sets are shown in Fig. 7.1 (hereinafter called S1), Fig. 7.2 (hereinafter called S2) and Fig. 7.3 (hereinafter called S3). reports the correspondence of specimen name, length of the square L and the ratio between L and the ligament thickness s. Each specimen name recalls the acronym of its set and the percentage length of the square with respect to the smallest square of each set.

Table 7.1 Specimen name, side length L of the corresponding SEM image and L/s ratio.

Specimen ID	$L\ (nm)$	L/s
	SET 1	
S1-800	525	28
S1-400	262.5	14
S1-200	131	7
S1-100	65.5	3.5
	SET 2	
S1-800	527	28
S1-400	263.5	14
S1-200	132	7
S1-100	66	3.5
	SET 3	
S1-1600	1054	55
S1-1200	790	42
S1-800	527	28
S1-400	263.5	14
S1-200	132	7
S1-100	66	3.5

7.2.3 Mechanical tests

Images of set S1 were printed with a Formlabs Form 2 SLA 3D printer, with the Dental Model resin. This kind of resin has a quite wide plastic region, in terms of stress-stain diagram. Furthermore, its elongation to failure is about of 13%. The samples were produced with a width of 40 mm and a thickness of 4 mm. Tensile tests on the printed samples were performed using an MTS Landmark 370 servo hydraulic machine test. The measurements were performed with the aid of DIC. In addition, a more classical extensometer (MTS 632-11F) was used to a results' comparison.

DIC consists in the digital correlation between pixels at different applied loads, resulting in the displacement's field. The DIC technique is based on a sub-partitioning of the image, and then its aim is to track the displacement of every subset between the reference and the current image analyzed. To do this, the surface of the samples was covered with a non-repetitive, isotropic, high-contrast speckle pattern of a size consistent with the resolution of the cameras and lenses used to capture the images. In this work, the surfaces of the samples were painted with a white background and a fine distribution of black dots using a professional airbrush and water-based paint, resulting in a density of approximately 3-6 pixels per speckle. The images were recorded using the monochromatic Allied Vision F421-B Pike high-resolution camera. Intensity was quantized using 8 bits and all test procedures were conducted over an optical bench. The sample was illuminated with a professional lamp capable of covering the sample with an almost uniform light field.

Finite Element Method (FEM) simulations were performed on all the three sets in accordance with the tensile tests, using 8 node 3D brick elements. The mean stress through the cell has been calculated using the mean reaction force on the clamped surface and the cell mean section. The strain was calculated using the mean vertical displacements on the top and the bottom edge of the cell, and then divided by the nominal edge distance.

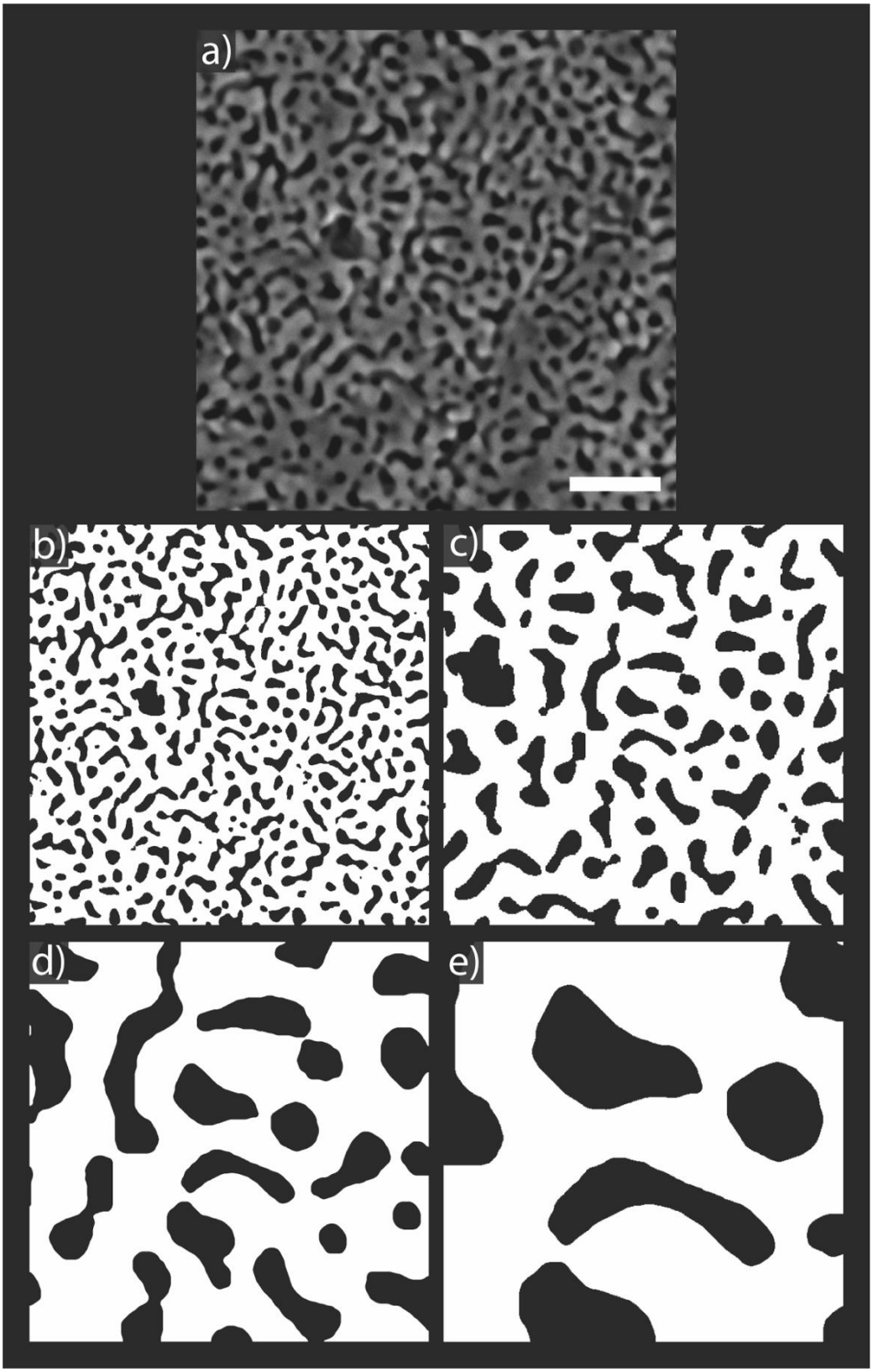

Fig. 7.1 Images of S1: original SEM image (a, scale bar:100nm), corresponding binarized image (S1-800) (b), concentric areas with side length 1/2 (S1-400) (c), 1/4 (S1-200) (d) and 1/8 (S1-100) (e) of the original one.

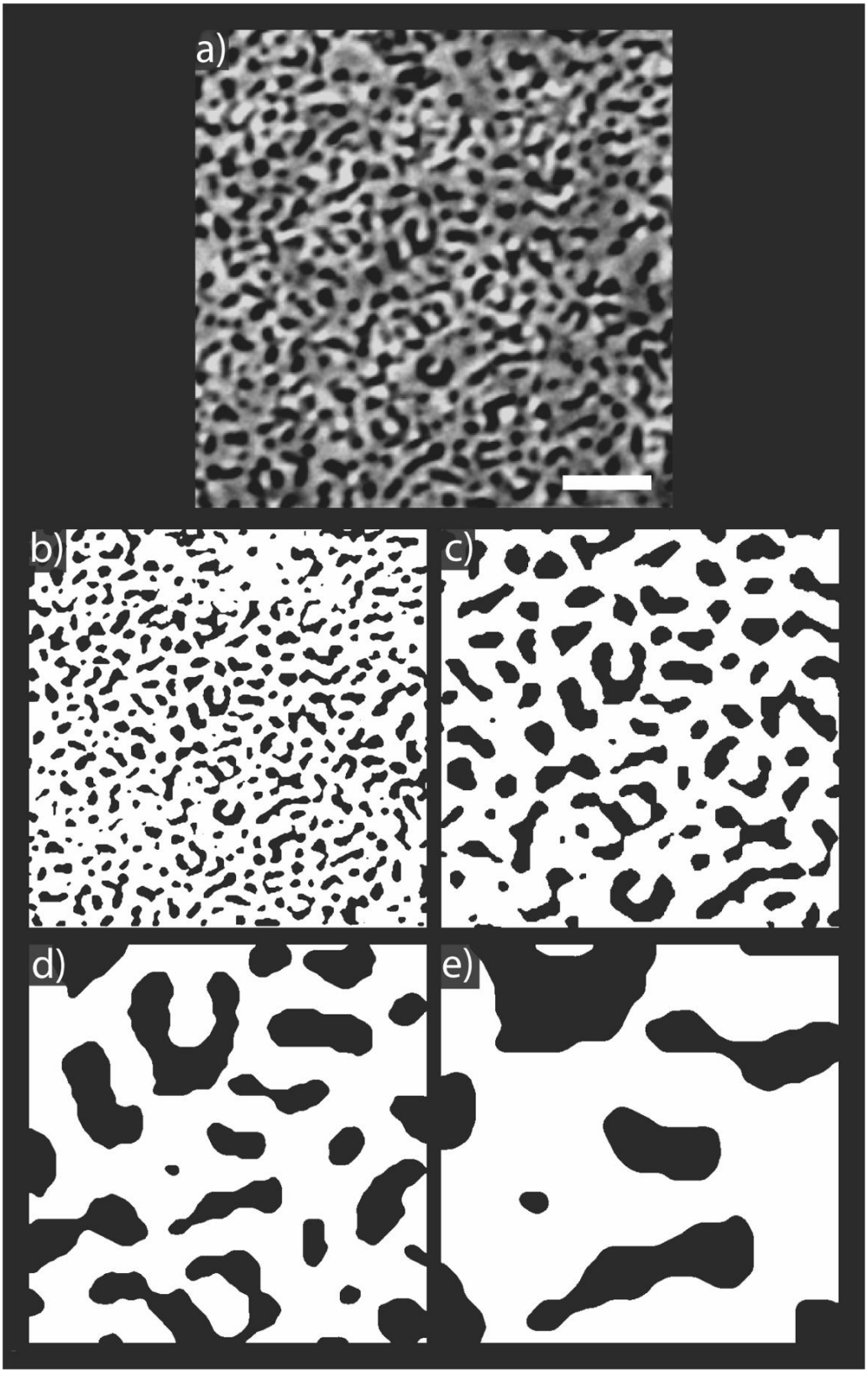

Fig. 7.2 Images of S2: original SEM image (a, scale bar: 100 nm), corresponding binarized image (S2-800) (b), concentric areas with side length 1/2 (S2-400) (c), 1/4 (S2-200) (d) and 1/8 (S2-100) (e) of the original one.

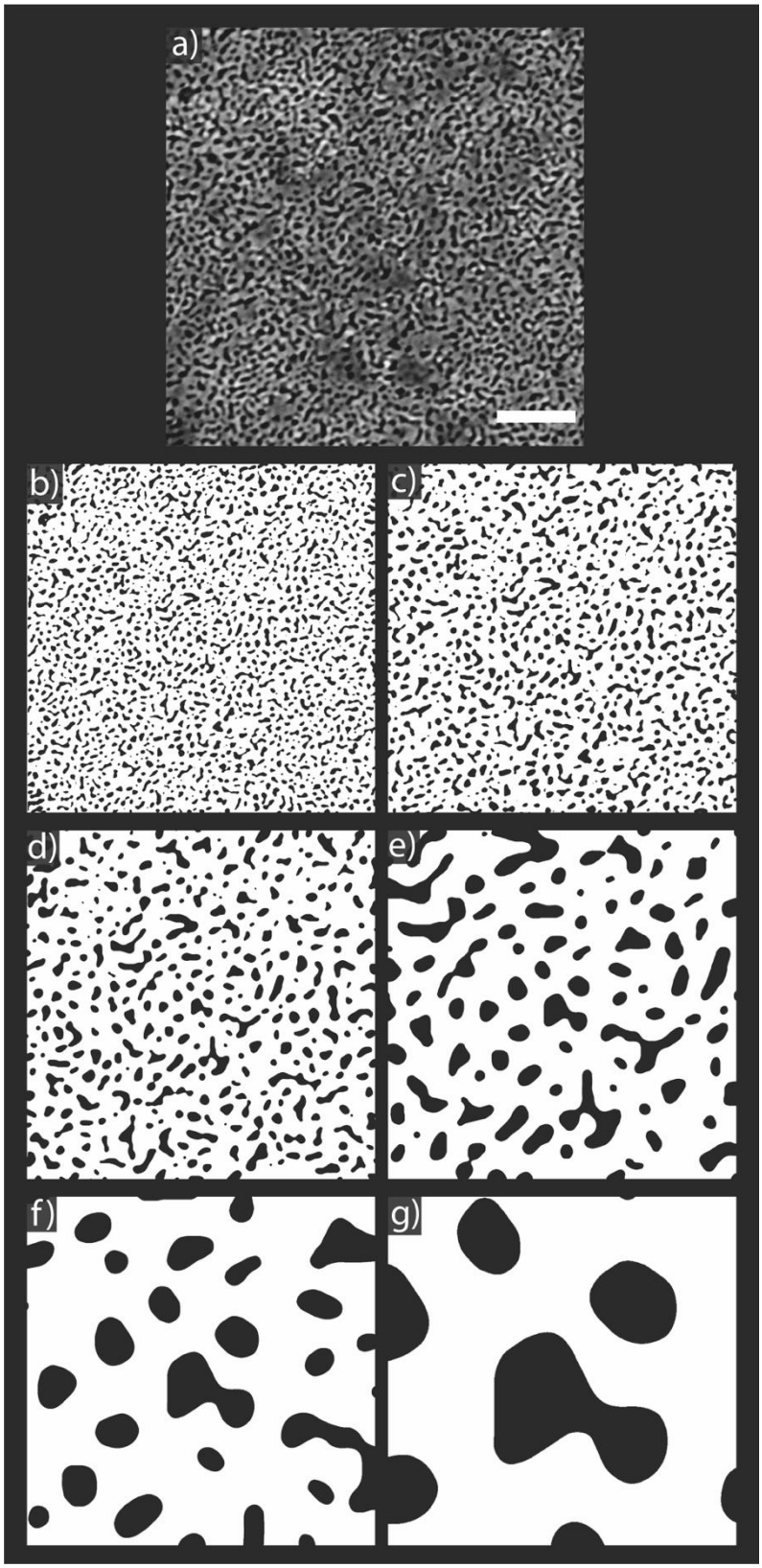

Fig. 7.3 Images of S3: original SEM image (a, scale bar: 200 nm), corresponding binarized image (S3-1600) (b) and concentric areas with side length 3/4 (S3-1200) (c), 1/2 (S3-800) (d), 1/4 (S3-400) (e) 1/8 (S3-200) (f) of the original one.

7.3 Results and Discussion

Fig. 7.4a-c show the photographs of the printed S1-800 specimen for DIC measurements before and during tensile testing. Fig. 7.4b shows the image of the sample strained of 6 mm: in the area evidenced in yellow there is the first fracture that then propagates causing a brittle rupture of the sample, shown in Fig. 7.4c. Since the solid resin used has a ductile behavior, the brittleness encountered in the samples derives from the geometry of the porous structure, probably from stress intensification at voids' sharp edge.

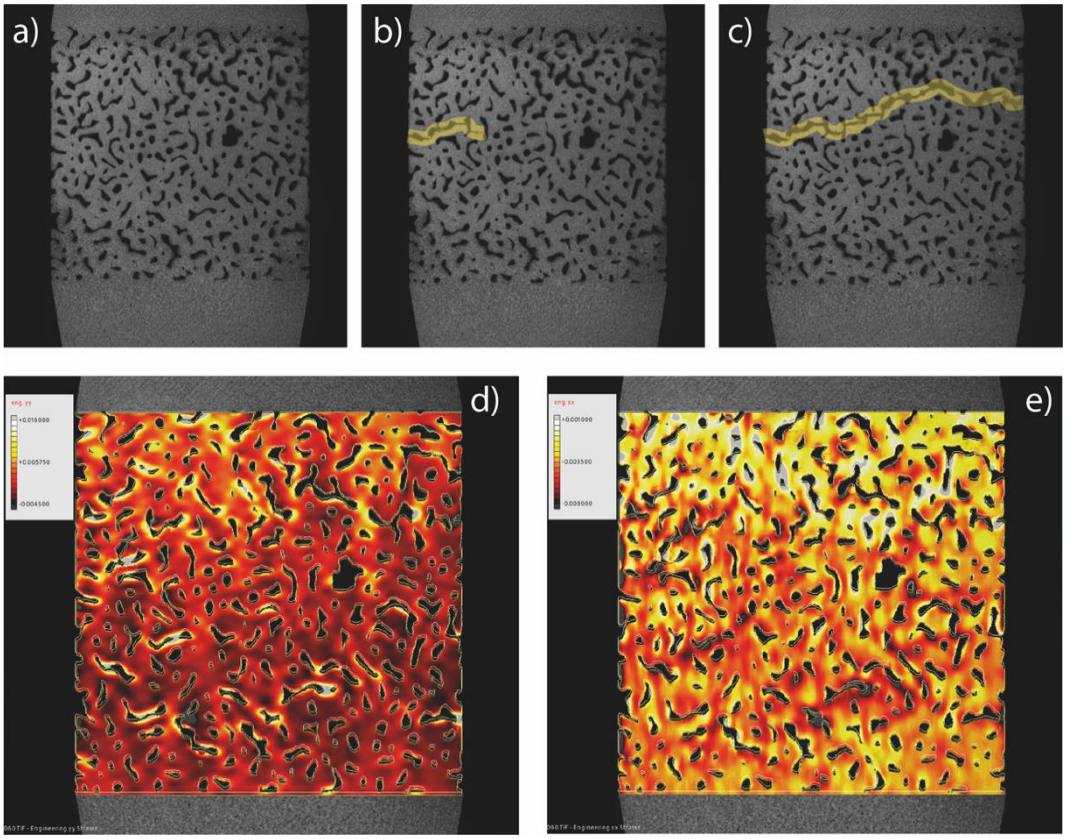

Fig. 7.4 Photographs of S1-800 specimen before tensile testing (a), after 6 mm displacement (b) and after fracture (c); DIC color maps of longitudinal (d) and transversal (e) of strain components.

Fig. 7.4d,e show DIC color strain field maps of the longitudinal and transversal components, respectively, superimposed on the surface of the specimen. Strain varies from positive (tensile) for lighter colors to negative (compressive) darker colors. The images show a heterogeneous behavior of the sample which seems divided into two areas: the top area undergoes a tensile strain, while the other reveals a high density of compressed regions. By comparing DIC images with Fig. 7.4c, it can be noted that the fracture seems to have proceeded along the boundary between the two areas.

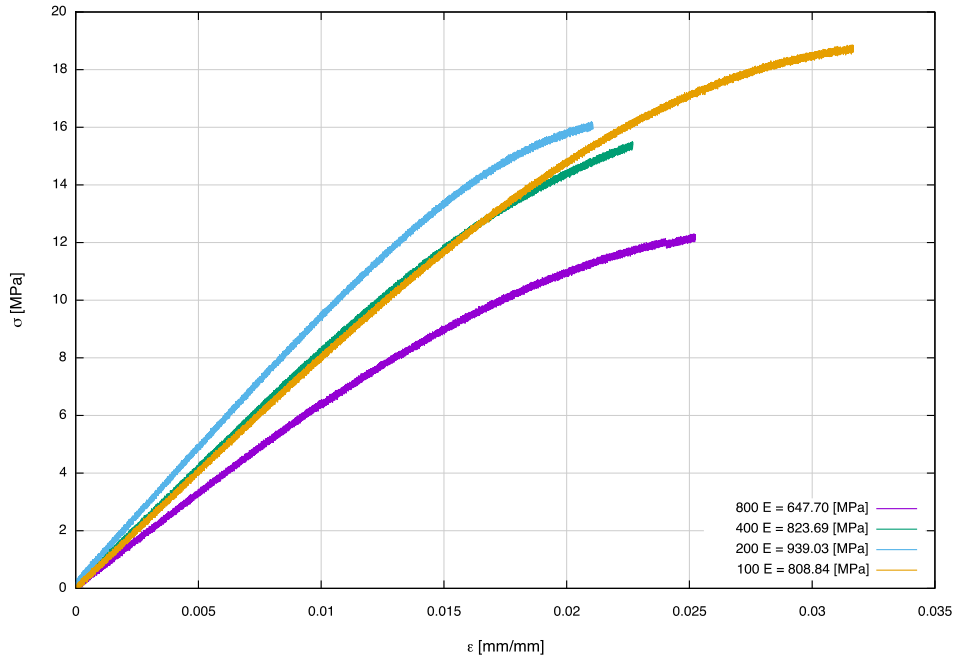

Fig. 7.5 Stress-strain curves of S1 samples.

Fig. 7.5 shows the stress-strain curves of S1 samples, measured from extensometer tensile tests. Young's modulus was calculated from these measurements and also from DIC and FEM. Its trend over the different lengths of the areas taken in account is shown in Fig. 7.6 are in accordance with each other: when the square size decreases from S1-800 to S1-200,

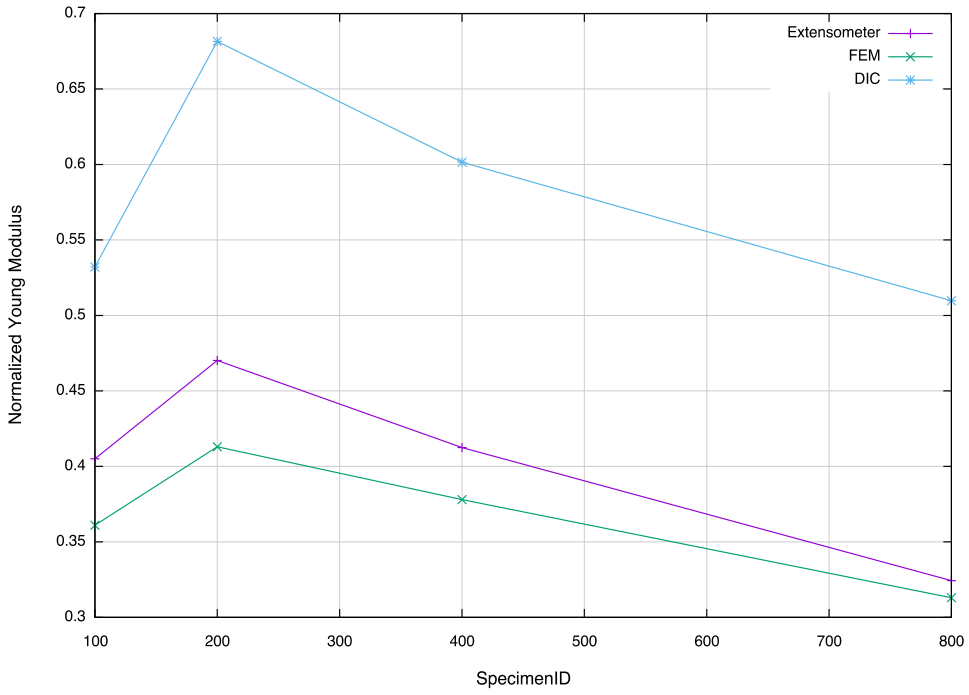

Fig. 7.6 Young's modulus of S1 specimens, calculated by DIC, extensometer tests and FEM.

Young's modulus increases almost linearly and finally decreases again at S1-100.

FEM was used to calculate the Young's modulus of the other two sets, shown in Fig. 7.7. It can be seen that the trends are different and there cannot be found any relationship between Young's modulus and size of the analyzed area for L/s ratio smaller than 28 (see). Nevertheless, for L/s values higher than 28 the Young's modulus becomes nearly constant for different L/s values. Therefore, it seems that under this value the mechanical response is governed by singular features of ligaments and pores, whose distribution becomes homogeneous in material areas larger than around 25-30 times the ligament thickness of the sample, generating a mean response that doesn't depend anymore on the size of the area considered.

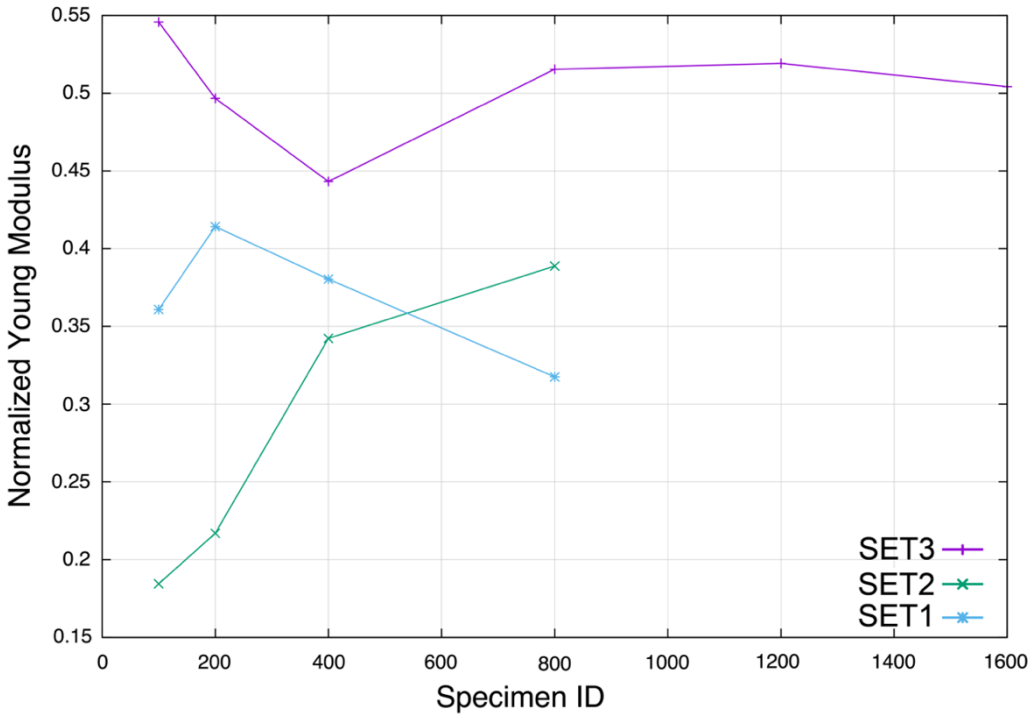

Fig. 7.7 Normalized Young modulus trend over size of area analyzed for the three SET studied by FEM.

The work presented here represents a first basis to be further explored in order to understand the reason for the heterogeneity of very similar structures of the ligament/pore interconnections and their effect on the global mechanical response of the material. It is clear that such changes across the same sample of NP Au will be further higher between samples made by different procedures. Therefore, it is important to find a relationship between geometrical parameters and the local response in order have more

tools for the optimization of the fabrication methods and the interpretation of experimental results.

7.4 Conclusions

In this chapter the effect of local ligament geometry on mechanical response of NP Au has been studied by means of macroscopic reconstructions of the 2D structure of ligaments and pores arising from SEM imaging. It was observed that at scales larger than the ligament size up to a factor of 28, the mechanical response is heterogeneous and areas with tensile and compressive strains can be found during tensile stresses. The relationship of mechanical response to the local topology of each ligament is still to be understood and will be addressed in the course of the work.

References

[1] B.A.M. Hodge, J.R. Hayes, J.A. Caro, J. Biener, A. V. Hamza, Characterization and Mechanical Behavior of Nanoporous Gold **, Adv. Eng. Mater. 8 (2006) 853–857. https://doi.org/10.1002/adem.200600079.

[2] I. McCue, E. Benn, B. Gaskey, J. Erlebacher, Dealloying and Dealloyed Materials, Annu. Rev. Mater. Res. 46 (2016) 263–286. https://doi.org/https://doi.org/10.1146/annurev-matsci-070115-031739.

[3] N. Badwe, X. Chen, K. Sieradzki, Mechanical properties of nanoporous gold in tension, Acta Mater. 129 (2017) 251–258. https://doi.org/10.1016/j.actamat.2017.02.040.

[4] G. Pia, F. Delogu, Mechanical Properties of Nanoporous Au: From Empirical Evidence to Phenomenological Modeling, Metals (Basel). 5 (2015) 1665–1694. https://doi.org/10.3390/met5031665.

[5] G. Pia, F. Delogu, Coarsening of nanoporous Au : Relationship between structure and mechanical properties, Acta Mater. 99 (2015) 29–38. https://doi.org/10.1016/j.actamat.2015.07.074.

[6] H.J. Jin, J. Weissmüller, Bulk nanoporous metal for actuation, Adv. Eng. Mater. 12 (2010) 714–723. https://doi.org/10.1002/adem.200900329.

[7] T.C. Chu, W.F. Ranson, M.A. Sutton, Applications of digital-image-correlation techniques to experimental mechanics, Exp. Mech. 25 (1985) 232–244. https://doi.org/10.1007/BF02325092.

[8] O.C. Zienkiewicz, R.L. Taylor, D. Fox, The Finite Element Method for Solid and Structural Mechanics: Seventh Edition, Elsevier Ltd, 2013. https://doi.org/10.1016/C2009-0-26332-X.

[9] J. Schindelin, I. Arganda-Carreras, E. Frise, V. Kaynig, M. Longair, T. Pietzsch, S. Preibisch, C. Rueden, S. Saalfeld, B. Schmid, J.Y. Tinevez, D.J. White, V. Hartenstein, K. Eliceiri, P. Tomancak, A. Cardona, Fiji: An open-source platform for biological-image analysis, Nat. Methods. 9 (2012) 676–682. https://doi.org/10.1038/nmeth.2019.

Conclusions and future perspectives

In this thesis, we addressed some important issues concerning nanoporous metal development. The search of effective methods to fabricate nanoporous metals and nanoporous metal-composites, and the study of some crucial properties of this kind of material have been the main subject of this work.

In particular, in **Chapter 2** the fabrication and morphological characterization of some nanoporous metals was presented. NP Au fabrication was performed from an AuAg alloy with Au content above the common parting limit, showing that Au surface diffusion can slowly allow Ag dissolution to proceed in these conditions, too. Moreover, a precursor nanocomposite made of a graphene dispersion in an AuAg alloy was fabricated and the resulting morphology and structure after dealloying were studied. The material displayed the typical bicontinuous porous structure of NP Au and no signs of graphene oxidation were detected by Raman Spectroscopy. NP Cu was also fabricated from a mechanically alloyed CuZn precursor. Dealloying was performed both by chemical corrosion and by Zn evaporation during annealing in high vacuum. The material produced by the first method displayed a finer porous structure with smoother ligaments compared to the one produced by the second method and represents one of the CuZn-dealloyed NP Cu examples with the smallest characteristic lengths.

In **Chapter 3**, the behavior of NP Au during thermal treatments was studied by analysis of literature data and by an experimental investigation. We found that the NP Au sample form and microstructure have a significant influence on the material thermal stability, mostly in terms of density. Low-dimensional samples and nanocrystalline ones are more prone to undergo densification and even complete collapse of the porous structure at temperatures higher than 300°C. In particular, from our experimental study, we found that the nanocrystalline AuAg alloy fabricated by mechanical alloy gives rise to an NP Au with fine bicontinuous morphology but low thermal stability, which can be enhanced by inducing grain growth through annealing before dealloying.

Chapter 4 discusses the interaction between NP Au and methyl orange, a common model molecule for degradation studies of some toxic azo dyes, class to which methyl orange belongs. When NP Au is immersed in a solution of the dye, the concentration of methyl orange drops down. This was previously associated with a pure catalytic degradation activated by NP Au. We discussed this hypothesis and found that, even if there are traces

of degradation, the material shows a dominant adsorption behavior which can be well fitted by the classical Langmuir adsorption model. A significant amount of the dye can be desorbed from the NP Au monolith and there are traces of its presence on the material surface even after the desorption stops. After the desorption, the pristine surface features of NP Au are not regenerated, i.e. it doesn't adsorb methyl orange again.

In **Chapter 5** we carried out two different procedures to prepare a heterojunction between NP Au and $CsPbBr_3$ perovskite nanocrystals (NCs). Perovskite NCs show great promises for their properties, among which the high absorption rate is one of the most fascinating, but the efficiency of excited charge carriers transfer is usually limited at perovskite/electrode interfaces. We observed that the deposition of the synthesized NCs by adsorption on NP Au isn't suitable, probably because of an interaction between Au and NCs capping agents that leave the perovskite in an unstable state leading to degradation. Nevertheless, we found that the synthesis of the NCs inside the metal pores gave rise to the formation of a heterojunction with a charge transfer between the NCs and NP Au ligaments. A very high transfer efficiency of around 47 % was found. The prepared nanocomposite can find interest in applications such as photovoltaics, photodetectors, and photocatalysis.

In **Chapter 6** the fabrication of NP Al and a fractal model designed for the prediction of its properties were presented. NP Al was prepared by Vapor Phase Dealloying of an AlZn precursor alloy. The resulting material was made of a multiscale porosity across the entire thickness of the monolith and a very high surface area of around 73 m^2/g. 3D reconstructions made by the SBF-SEM imaging were used to design a fractal model capable of reproducing the surface area of the material. Its efficacy for properties prediction was evaluated by calculating the expected Young's modulus of the material, which was found in optimal accordance with experimental measurements made by nanoindentation.

Finally, the preliminary results of a study on the mechanical properties of NP Au are reported in **Chapter 7**. We investigated the effect of the characteristic geometry of NP Au ligaments and pores on the mechanical properties of the material. For this purpose, SEM images were exploited to print macroscopic reconstructions of the porous morphology, and mechanical tensile tests were performed on the printed specimens. Digital Image Correlation was used to gain local information about the deformation of any specific area of the sample, from which we noted a heterogeneous behavior of apparently similar porous regions. Moreover, we found that Young's modulus considerably changes along with different local areas of

the sample and that it becomes a constant average of the heterogeneous local values when an area with side length around 28 times the mean ligament diameter is stressed.

The work done in this thesis leaves the opportunity for further studies in the next future. In addition to the continuation of the preliminary work described in **Chapter 7**, NP Au/graphene nanocomposite properties for applications in the field of catalysis and sensing will be studied; in particular, the effect of graphene in the electric transport and the functionalization of NP Au is of high interest. Moreover, NP Au/$CsPbBr_3$ heterojunction will be the subject of studies for photocatalysis and photodetection applications. Finally, NP Al is a new material of which only a few studies have been reported with different fabrication methods than ours. Considering the high potential interest for a wide set of low-cost and advanced applications, it is fundamental to gain a deeper knowledge of its structure tunability and its related properties.

Acknowledgments

I’m deeply grateful to my supervisor, Prof. Luca Pilia, for the precious supervision, support, availability in confrontation, and for the patient transmission of his invaluable expertise throughout the years. I extend my sincere gratitude to my co-supervisor, Prof. Giorgio Pia, for his advice, supervision and the precious contribution in the research activity.

I would like to express my warm gratitude to Prof. Andrea Falqui for hosting me for 4 months at King Abdullah University of Science and Technology (KAUST), which is also kindly acknowledged for hospitality and funding. I would like to extend my gratitude to all members of Prof. Falqui's team, who welcomed and helped me with anything. In particular, Prof. Falqui and Dr. Elisa Sogne are also kindly acknowledged for training me in Electron Microscopy techniques and for SEM/EDS and SBF-SEM imaging reported in Chapter 2, Chapter 4, Chapter 6, and Chapter 7.

I’m also grateful to Prof. Francesco Delogu, for his contribution to the idealization and realization of the research activity, his advice and support.

I’m also really grateful to Dr. Nicola Melis, who has been of great help and support for any problem, scientific or not, for all the Ph.D. period with boundless willingness, and who performed electrochemical measurements in Chapter 4.

I would like to thank Prof. Carlo Maria Carbonaro, Prof. Pier Carlo Ricci for the hospitality in their labs for Vapor Phase Dealloying treatments and Raman Spectroscopy measurements, and for the support I received for any necessity. I thank them and Dr. Jessica Satta, Dr. Luigi Stagi, and Prof. Daniele Chiriu also for their contribution in the design and execution of the work on NP Au/perovskite composites reported in Chapter 5.

I’m really grateful to Prof. Maria Francesca Casula for N_2 physisorption measurements on NP Al, her advice, and continuous availability.

Prof. Antonio Baldi and Pietro Santucci are kindly acknowledged for their collaboration in the study presented in Chapter 7, especially for having performed the 3D printing of the macroscopic reconstructions of NP Au structure and the mechanical tests and simulations.

Dr. Giorgia Cutrufello is kindly acknowledged for the HPLC analysis reported in Chapter 4. Dr. Mirko Prato is also kindly acknowledged for XPS analysis reported in Chapter 4.

I’d also like to thank Prof. Roberta Licheri for SEM imaging reported in Chapter 3, and to Ten. Col. Cesare Vecchio Comandante del Reparto Investigazioni Scientifiche di Cagliari, Magg. Marco Palanca Comandante della Sezione di Chimica, Esplosivi ed Infiammabili, Mar. Ord. Claudia Melis Analista di laboratorio in Microscopia Elettronica for SEM imaging reported in Chapter 5. I also acknowledge the CeSAR (Centro Servizi d’Ateneo per la Ricerca) of the University of Cagliari for TEM imaging (Chapter 2) and EDS measurements of Chapter 5.

Finally, I’m grateful to Prof. Paola Rizzi and Dr. Stefano Giordano for the careful reviewing of the thesis and for their precious comments and advices.

Appendix

A.I Supporting material of Chapter 2

Fig. A.I.1, Fig. A.I.2, and Fig. A.I.3 show the morphology of NP Cu in the three different areas of the cross-section: near the upper surface, in the interior, and near the lower surface. We call the two surfaces upper and lower for simplicity, but they are equivalent concerning the experimental procedure.

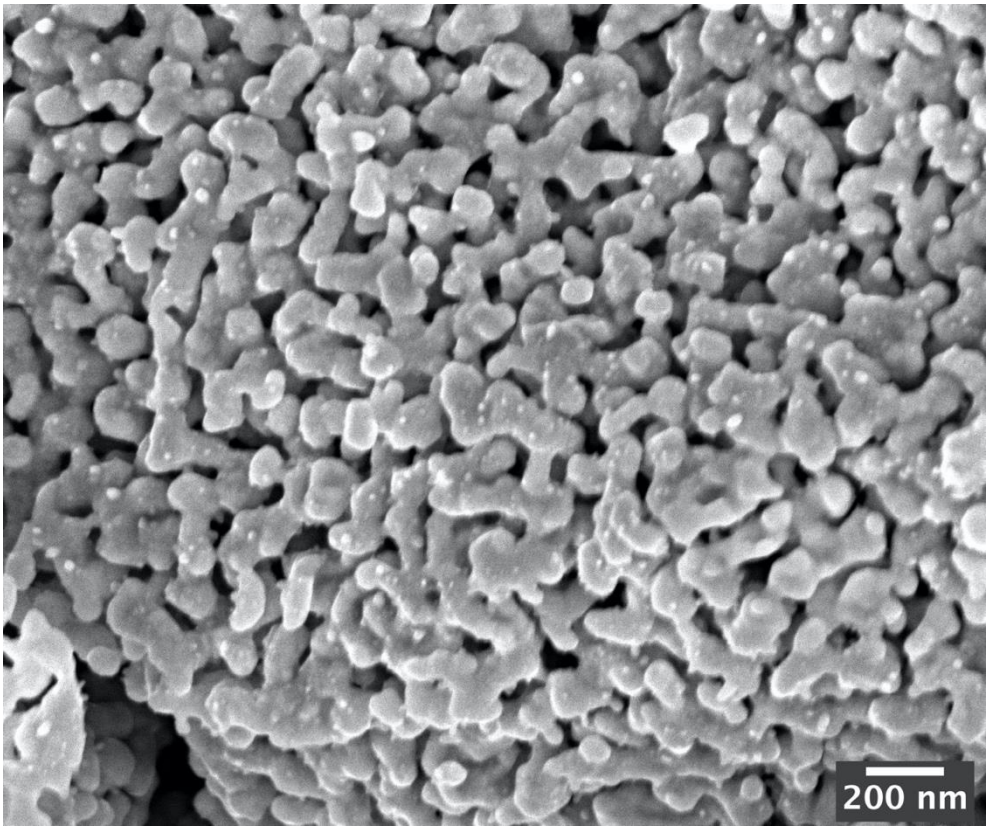

Fig. A.I.1 SEM image of NP Cu morphology of a cross section area in the interior of the sample.

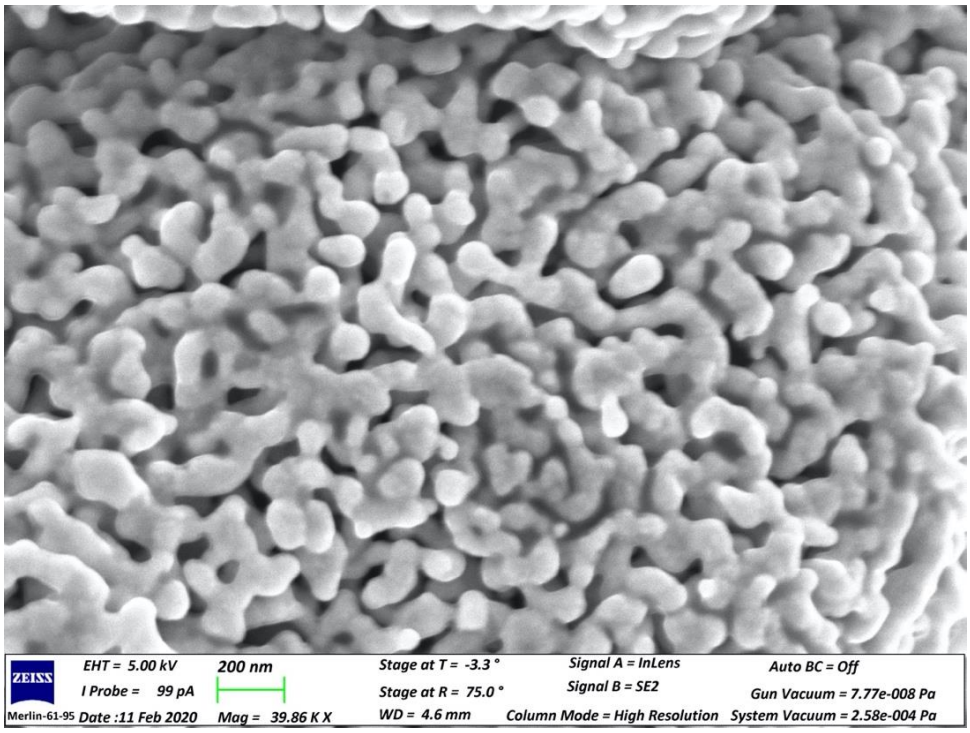

Fig. A.I.2 SEM image of NP Cu morphology of a cross section area in the interior of the sample.

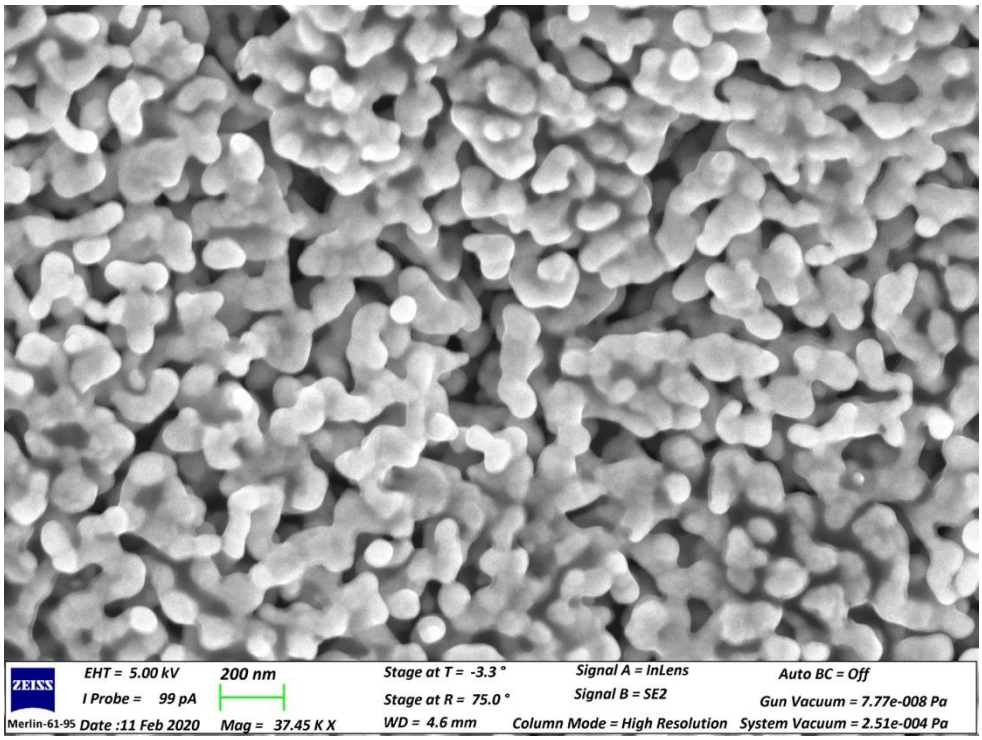

Fig. A.I.3 SEM image of NP Cu morphology of a cross section area near the lower surface.

A.II Supporting material of Chapter 6

The representative video of the porosity evolution of NP Al sample during subsequent cuts can be found at the following link, furnished by the publisher of the article associated with this work:

https://www.mdpi.com/article/10.3390/app11146639/s1

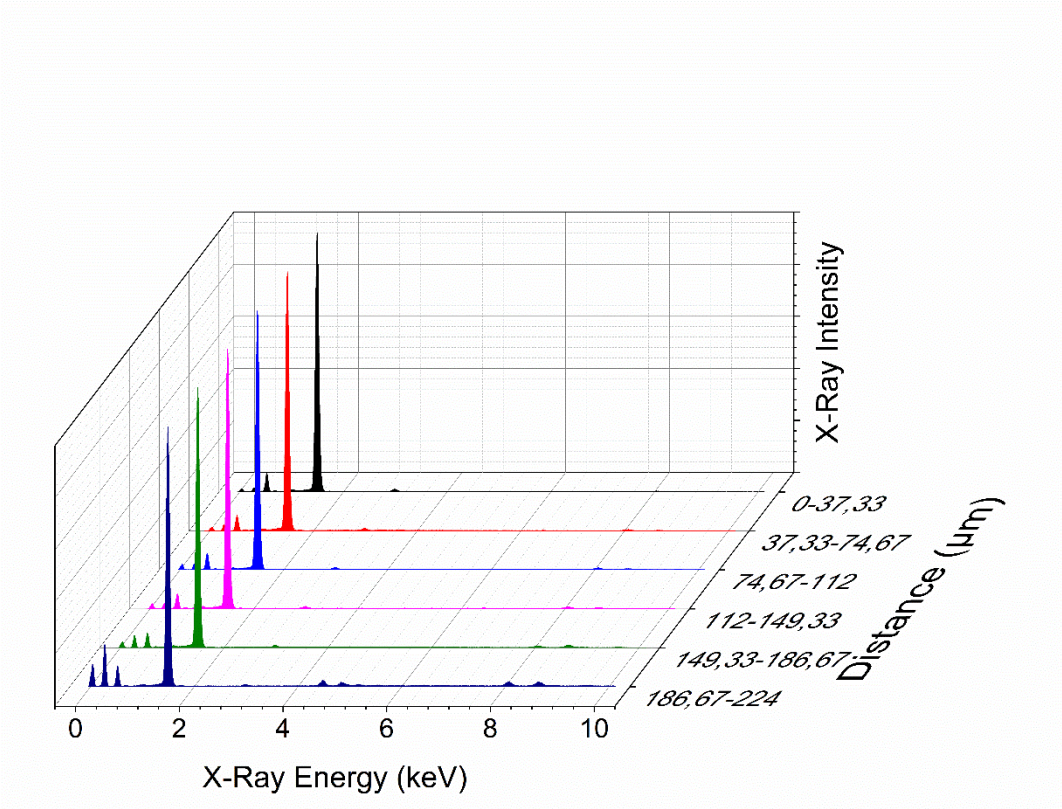

Fig. A.II.1 EDS spectra of cross-section areas of NP Al at different distances from the upper surface of the specimen.

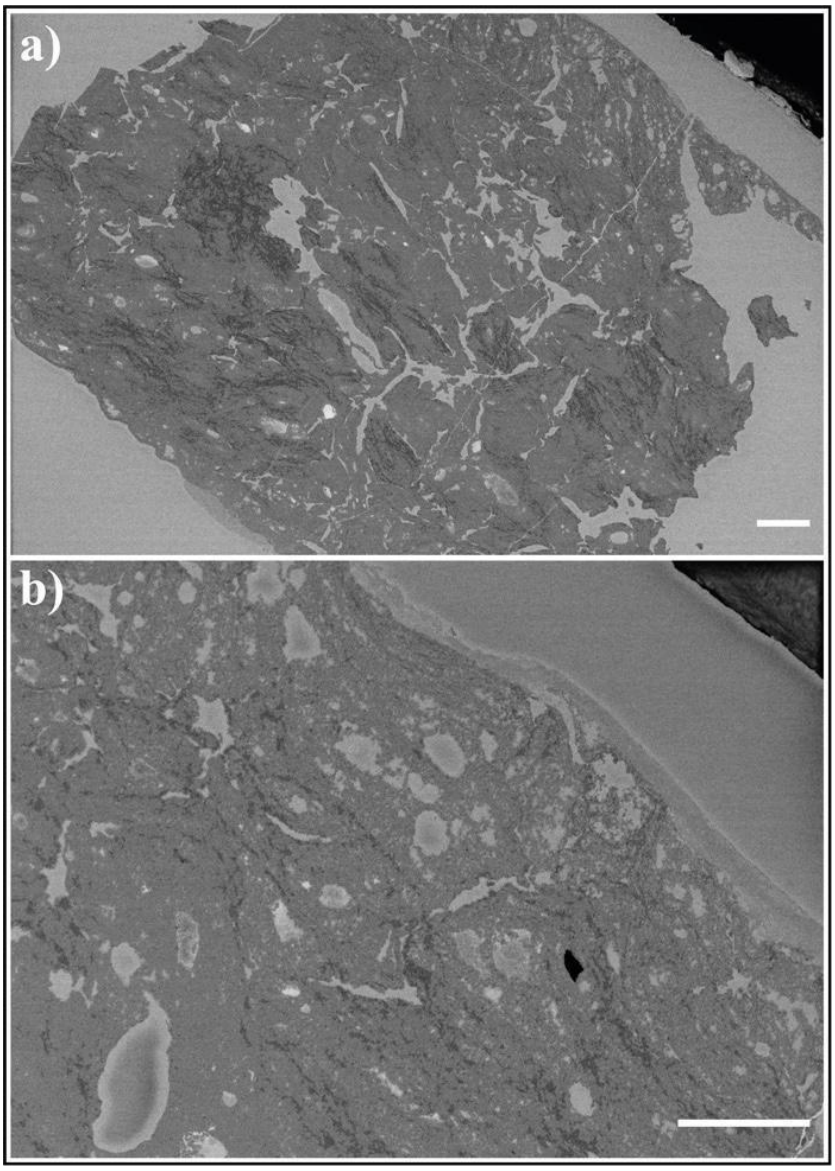

Fig. A.II.2 examples of inverted SEM-SBF images taken at (a) low magnification (scale bar: 20 µm) and (b) higher magnification (scale bar: 10 µm).

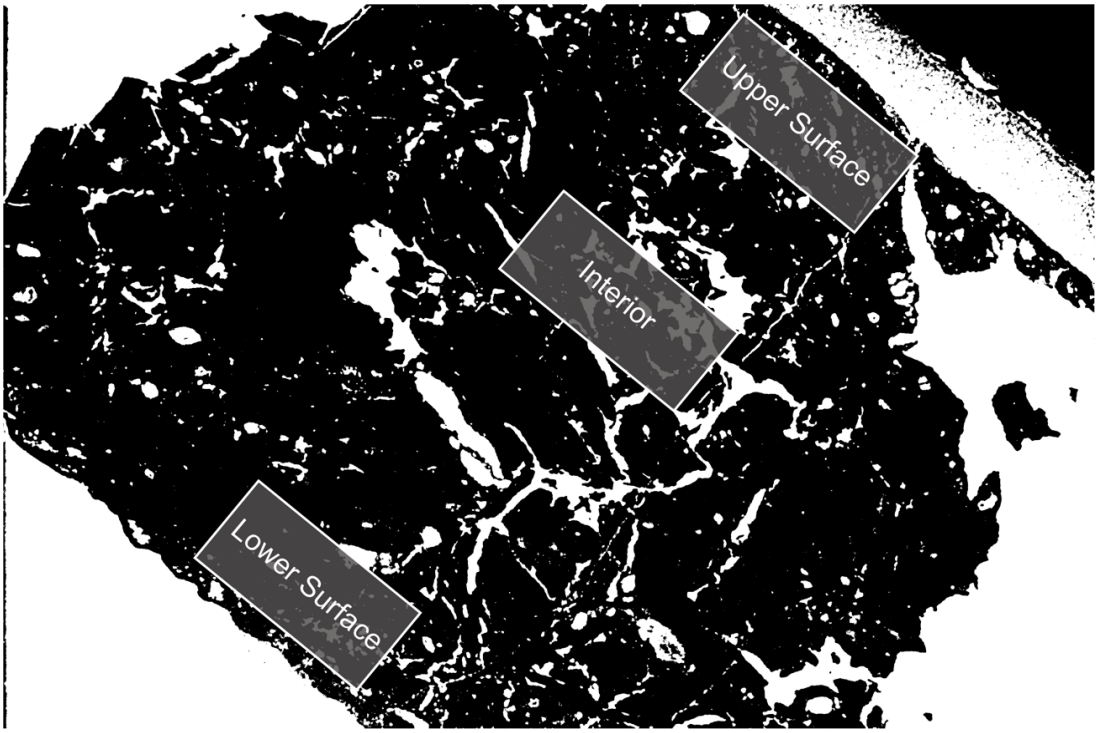

Fig. A.II.3 Inverted and binarized SBF-SEM image of NP Al cross-section in which the three areas of the cross-section subjected to IA are shown.

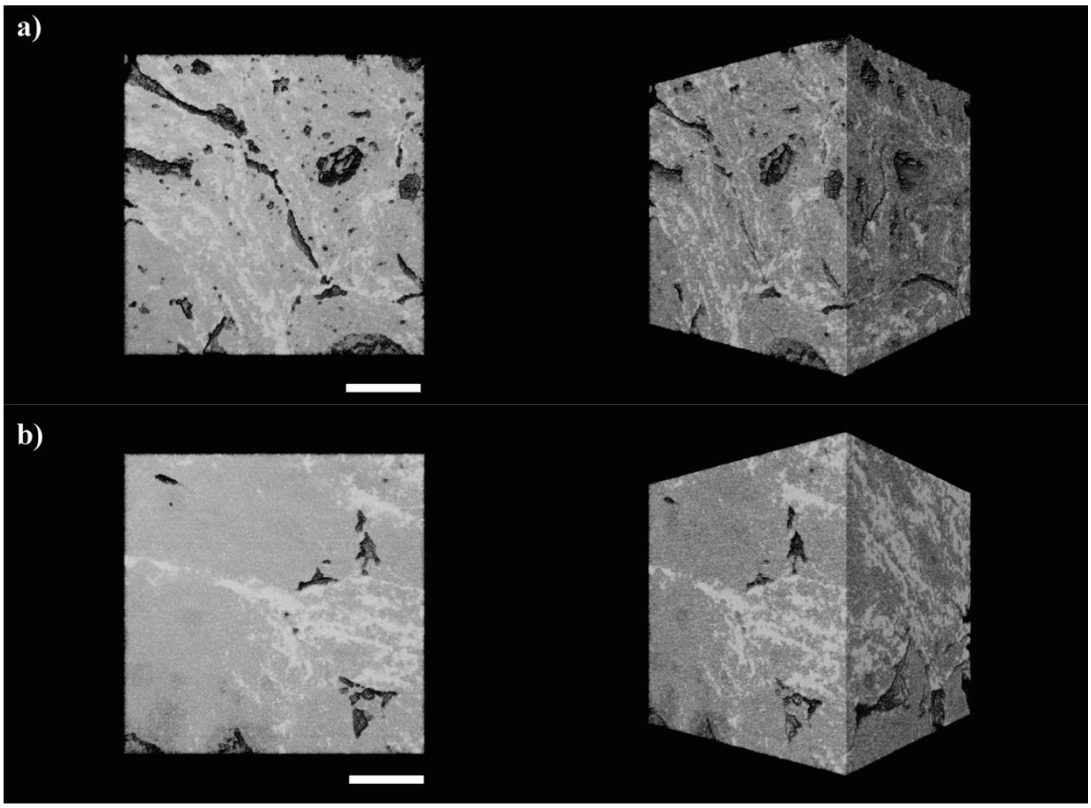

Fig. A.II.4 3D reconstructions of the top surface(a) and interior areas (b) at higher magnification. Scale bar 5 µm.

Figure index

Figure index

Figure index

Figure index

Figure index

Figure index